VIBRATIONAL SUM FREQUENCY AND RAMAN SPECTROSCOPIC STUDIES OF AIR-AQUEOUS INTERFACES AND SOLUTIONS OF NITRATE SALTS, AND AIR-SILICA SURFACE ADSORPTION STUDIES

DISSERTATION

Presented in Partial Fulfillment of the Requirements for
the Degree Doctor of Philosophy in the Graduate
School of The Ohio State University

By
Man Xu
*****
The Ohio State University
2008

Approved by

Dissertation Committee:

Professor Heather C. Allen, Advisor
Professor James V. Coe
Professor John Lenhart

_____
Advisor
Environmental Science Graduate Program

ABSTRACT

Nitrate ions are ubiquitous in aqueous-phase atmospheric aerosols as well as surface and ground waters, and are involved in a variety of reactions in the atmosphere, hydrosphere, and biosphere. A fundamental understanding of nitrate ions at the air-aqueous interface is of prime importance with respect to understanding heterogeneous atmospheric chemistry and geochemistry. Surface activity at the air-aqueous interface may have consequences for diffusion rates and reaction pathways within the interface. Although numerous arguments have been proposed concerning the nature of nitrate ions at aqueous interfaces, there is a lack of detailed molecular-scale experimental evidence. In the studies presented in this dissertation, vibrational sum frequency generation (VSFG) spectroscopy, an interface specific technique that provides direct molecular-level interfacial information, was employed as the primary investigational technique to elucidate the nature of nitrate ions and formation of ion pairs at the air-aqueous interface, and to reveal their influence on the interfacial water structure. Raman and infrared spectroscopies were utilized in addition to VSFG spectroscopy.

Investigations of ion pairing in a series of divalent metal-nitrate solutions were carried out using Raman and infrared spectroscopies. The spectral features of the nitrate vibrational modes indicate that the ion pairing in the metal-nitrate aqueous solutions are concentration and cation dependent. Pb^{2+} has a strong tendency to form ion pairs with

nitrate anions, and the formation of contact ion pairs decreases with decreasing cation size and increasing cation charge density: $Pb^{2+} > Sr^{2+} > Ca^{2+} > Mg^{2+}$.

At the air-aqueous interface, the vibrational symmetric stretch mode of nitrate ions was directly probed by VSFG. Analysis of the VSFG spectra reveals the perturbation from cation-anion interactions on interfacial nitrate ions. $Mg(NO_3)_2$ is particularly interesting at the air-aqueous interface. At low bulk concentration of $Mg(NO_3)_2$, interfacial nitrate anions are relatively free from Coulombic effects of Mg^{2+} cations, which indicates that the number of water molecules available for solvation significantly affects the extent of interfacial ion pairing. This finding and the associated spectral identification shed additional light on the level of interaction between Mg^{2+} and nitrate in the bulk solution. That is, in previous bulk studies, it has been accepted that Mg^{2+} causes negligible perturbation on nitrate and therefore, no significant ion pairing interactions were concluded. With the results from this dissertation, although the frequency of the nitrate symmetric stretch does not change significantly in bulk aqueous $Mg(NO_3)_2$ systems with concentration, the bulk frequency is in fact evidence of Mg^{2+}–nitrate interaction, solvent-shared or solvent-separated ion pairing most likely. This is clear only after the completion of our interfacial studies that reveal a never before observed frequency from aqueous $Mg(NO_3)_2$ systems.

The addition of nitrate salts also has considerable effects on the interfacial water structure, as observed in our VSFG studies of the OH stretching modes. The sum

frequency spectral features reveal that the presence of nitrate anions, metal cations, and the ion pairs perturbs the water hydrogen-bonding network at the air-aqueous interface, and the perturbation varies with cation. We propose an increasing interfacial depth as the cation size increases: Mg^{2+} < Ca^{2+} < Sr^{2+}. Interfacial depth is defined by non-bulk behavior. That is, the cation and anion concentrations are not constant in the first few layers of the air-aqueous interface. Alternatively, concentrations are changing deeper into what is traditionally called the bulk liquid.

In additional studies, distinct from the ion-pairing work at the air-aqueous interface, the surface acidity of silica, which is also atmospherically and geochemically important, was determined by using a surface acidity probe molecule, ethylenediamine ($H_2N(CH_2)_2NH_2$, EDA). The VSFG study of EDA adsorption onto silica surfaces indicate that the adsorption occurs via protonation of an amine group by a silica surface silanol site. The surface acidity of silica is therefore in the range of two pK_a values of EDA: 7.56 to 10.71.

Dedicated to Honglu and my parents

ACKNOWLEDGMENTS

I wish to thank my advisor, Dr. Heather Allen, for her guidance, support, and encouragement, which made it possible for me to accomplish the research necessary to complete this degree. I also wish to thank all of the Allen lab members, past and present. In particular, I am grateful to Dr. Dingfang Liu and Dr. Gang Ma, who were always readily available to assist when obstacles arose. I also want to thank Dr. Laura Voss, Dr. Lisa Van Loon, Cheng Y. Tang, and Xiangke Chen, the discussions with whom were instrumental in the success of this work. I thank my parents for their continual support. I especially thank my husband Honglu Liu. Without his constant encouragement and support, this achievement would not have been possible. Finally, I gratefully acknowledge funding of this work from the Department of Energy (DOE-BES, DE-FG02-04ER15495).

VITA

March 22, 1978 .....……...Born – Jiangsu, China

June 1999 .....……...B. Sc. Chemistry
Nanjing University

June 2002 .....……..M. Sc. Environmental Science
Nanjing University

2002 – 2008 .....……...Graduate Teaching Associate
The Ohio State University

2002 – 2008 .....……Graduate Research Associate
The Ohio State University

PUBLICATIONS

Xu, M.; Liu, D.; Allen, H. C. Ethylenediamine at air-aqueous and air-silica interfaces: protonation versus hydrogen bonding investigated by sum frequency generation spectroscopy. *Environmental Science and Technology*, 2006, **40**(5), 1566.

Liu, D.; Ma, G.; Xu, M.; Allen, H. C. Adsorption of ethylene glycol vapor on α-Al_2O_3 (0001) and amorphous SiO_2 surfaces: observation of molecular orientation and surface hydroxyl groups as sorption sites. *Environmental Science and Technology*, 2005, **39**(1), 206.

FIELDS OF STUDY

Major Field: Environmental Science

TABLE OF CONTENTS

LIST OF TABLES

Page

LIST OF FIGURES

Page

LIST OF ABBREVIATIONS

Å	Angstrom
AS	asymmetric stretch
ATR	attenuated total reflection
A.U.	arbitrary units
CIP	contact ion pair
CCD	charge-coupled device
ºC	degrees Celsius
CW	continuous wave
EDA	ethylenediamine
FTIR	Fourier transform infrared
FL	focal length
fwhm	full width at half maximum
hwhm	half width at half maximum
IPD	in-plane deformation
IR	infrared
K-K	Kramers-Kronig
M	moles per liter
m	moles of solute per kilogram of water
MD	molecular dynamics

m.f.	mole fraction
$m.f._s$	surface mole fraction
μm	micrometer
nm	nanometer
OPD	out-of-plane deformation
ps	picosecond
RH	relative humidity
SDS	sodium dodecyl sulfate
SS	symmetric stretch
SSHIP	solvent-shared ion pair
SSIP	solvent-separated ion pair
$SDR_{IP/free}$	surface number density ratio of ion-paired to relative free nitrate
VSFG	vibrational sum frequency generation
VIS	visible
cm^{-1}	wavenumber

CHAPTER 1

INTRODUCTION

The work presented in this dissertation was motivated by a desire to contribute to a better understanding of ion pairing (cation-anion association) and surface complex formation of divalent metals at the air-aqueous interface and the aqueous-mineral oxide interface. In-depth understanding of these processes is of significant importance in heterogeneous atmospheric chemistry and aqueous geochemistry. This research focuses on the ion pairing of nitrate-containing aqueous systems.

Nitrate, an important nitrogen species in the nitrogen cycle, is of great environmental interest. In the atmosphere, nitrate is pervasive in the form of nitrate radicals and nitrate ions. Nitrate radicals have been studied extensively with respect to their role in night-time gas-phase atmospheric chemistry.[1,2] Like the gas-phase nitrate radical in the atmosphere, the aqueous-phase nitrate ion is a common constituent of atmospheric aerosols. Gaseous ammonia reacts with nitric acid in the atmosphere and forms aerosol ammonium nitrate. The generated nitrate aerosols are in the aqueous state at the relative humidity conditions above the deliquescence.[3] In marine regions, the formation of nitrate aerosols is associated with significant chloride ion depletion in sea salt aerosols as a result of NaCl reaction with HNO_3, NO_3 radicals, N_2O_5, and $ClONO_2$.[1,2,4,5] Water induced

recrystallization of nitrate on NaCl surfaces into $NaNO_3$ crystallites avoids passivation of the surface, which, in turn, further depletes chloride ions.[5,6] The gaseous halogen products generated are photochemically active and are involved in ozone destruction and/or formation, and in reactions with organics in the troposphere.[4,5] Such chemistry is of significant importance in marine urban regions.[5,6] In polar regions, recent studies[7-10] have indicated that photolysis, as well as other processes, re-evaporation, sorption, and desorption, may contribute to the nitrate loss in polar snowpacks, complicating the atmospheric interpretation of the ice core nitrate records. The emissions from nitrate photolysis in polar firn are thought to account for the elevated levels of nitrogen oxides and hydroxyl radicals above snowpacks, which may ultimately affect the global chemical composition.[7,9-11]

In the hydrosphere and on land, nitrate is an essential nutrient to plants.[12-14] Yet, excessive concentrations of nitrate ions may contribute to eutrophication and exhibit toxicities to humans and other animals.[12,13,15] Ammonia and other nitrogen compounds in natural waters tend to be oxidized by aerobic bacteria to nitrite and then to nitrate. Compounds containing nitrogen, including organic nitrogen compounds from wild animals, feedlots, human sewage, and inorganic nitrogen compounds from manufactured fertilizers, can be considered as potential nitrate sources.[12,13,15] Nitrate leaching from soils is also important for nitrate ions in surface and ground waters.[14,16] In some agriculture areas, nitrogen fertilizers and livestock manure have caused serious problems to surface

waters and ground waters.[12,15] Being an essential nutrient for aquatic microorganisms and plants, excess nitrate ions could result in eutrophication in water bodies, though most often phosphorus is the limiting nutrient.[17] Another consequence of high nitrate concentrations in water systems is the toxicity to humans and aquatic life.[12,13,15] Nitrate itself is not toxic; however, nitrite produced through the reduction of nitrate is highly toxic to humans, especially to infants.

The nature of nitrate ions at the aqueous interface has received considerable attention. Recent computational studies of nitrate ions have produced conflicting results concerning the propensity of nitrate ions for the air-aqueous interface.[18-21] Salvador et al. proposed that the nitrate ion might prefer interfacial over bulk solvation,[18] whereas Dang et al. predicted that the nitrate ion was preferentially localized below the Gibbs dividing surface.[19] The Gibbs dividing surface is where the interfacial water density is half its bulk value. More recent molecular dynamics (MD) simulations suggested that nitrate ions exhibit a very weak surface propensity and a small amount of nitrate ions reside at the water surface.[20,21]

The studies presented in this dissertation aim at elucidating the nature of nitrate ions and metal-nitrate ion pairing at the air-aqueous interface, as well as their effects on the interfacial water structure. Vibrational sum frequency generation (VSFG) spectroscopy, an interface specific technique that provides direct molecular-level interfacial information, was employed as the primary investigational technique for the interfacial studies. Raman

and infrared spectroscopies that provide the bulk information were utilized to complement the VSFG studies. The related theories are presented in Chapter 2. Experimental details can be found in Chapter 3 and in subsequent chapters.

In order to understand the metal-nitrate ion pairing in the interfacial region, first of all, it is critical to study the ion pairing in aqueous solutions. This is the focus of Chapter 4. Results reveal that Pb^{2+} has a strong tendency to form ion pairs with the nitrate anions relative to Sr^{2+}, Ca^{2+}, and Mg^{2+} in their aqueous solutions, and contact ion pair formation decreases with increasing cation charge density: $Pb^{2+} > Sr^{2+} > Ca^{2+} > Mg^{2+}$. Chapters 5 and 6 investigate the divalent metal-nitrate ion pairing at the air-aqueous interface and the influence on the interfacial water structure. For the first time, a vibrational mode of the nitrate ion at the air-aqueous interface is directly probed by VSFG. The VSFG results of the nitrate vibrational modes reveal that the interfacial nitrate anion follows bulk ion pairing trends. $Mg(NO_3)_2$ is particularly interesting at the air-aqueous interface. Nitrate is relatively free from the Coulombic effects of cations for lower concentration $Mg(NO_3)_2$ aqueous solutions. The sum frequency spectral features in the water OH stretching region indicate the effects of divalent metal cations and nitrate anions on the interfacial structure of water, revealing that water solvation and metal-nitrate ion pairing perturb the water structure at the air-aqueous interface. A thickening of the air-aqueous interface is suggested as the cation size increases: $Mg^{2+} < Ca^{2+} < Sr^{2+}$. Additionally, a quantitative study of surface acidity of silica, one important mineral oxide, is presented in Chapter 7.

Ethylenediamine (EDA) that has the amine moieties of many widely used environmental contaminants was employed as the surface acidity probe. The study of EDA adsorption onto silica surfaces indicates that the adsorption occurs through protonation of an amine group by a silica surface silanol site, and the surface acidity of silica is quantified to be in the range of two pK_a values of EDA: 7.56 to 10.71. Such quantitative surface acidity information of mineral oxides helps to better understand chemical processes on mineral oxide surfaces, such as adsorption, desorption, and heterogeneous reactions in controlled or natural environments, and is useful in future studies of metal adsorption and metal-anion pairing at aqueous-mineral oxide interfaces.

CHAPTER 2

THEORIES

2.1 Vibrational Sum Frequency Generation Theory

2.1.1 Vibrational Sum Frequency Generation

Detailed theoretical descriptions of the VSFG process are available in the literature.[22-25] A brief introduction of this spectroscopic technique is given here. VSFG is a second-order nonlinear process that occurs in noncentrosymmetric environments such as interfaces under the electric-dipole approximation. In the VSFG process, coherent sum frequency photons are generated by spatially and temporally overlapping of a visible beam and an infrared beam at a sample surface. The resulting sum frequency light pulses have a frequency, ω_{VSFG}, which is the sum of the frequencies of the two incident pulses, ω_{VIS} and ω_{IR}. Both reflected and transmitted sum frequency signals are generated. When visible and IR light pulses are in co-propagating geometry, the reflected sum frequency occurs at an angle θ_{VSFG} given by:

$$k_{VSFG} \sin\theta_{VSFG} = k_{VIS} \sin\theta_{VIS} + k_{IR} \sin\theta_{IR} \tag{2.1}$$

θ is the angle of the indicated beam to the surface normal, and k refers to the phase that equals $n\omega/c$, where n is the real refractive index (details see section 2.3) of the medium through which the indicated beam travels, ω is the frequency of the indicated beam, and c

is the speed of light in vacuum.

The VSFG intensity, I_{VSFG}, is proportional to the absolute square of the effective sum frequency susceptibility, $\chi_{eff}^{(2)}$, and to the intensities of the visible and infrared incident pulses:

$$I_{VSFG} = \frac{8\pi^3 \omega_{VSFG}{}^2 \sec^2 \theta_{VSFG}}{c^3 n_1(\omega_{VSFG}) n_1(\omega_{vis}) n_1(\omega_{IR})} |\chi_{eff}^{(2)}|^2 I(\omega_{vis}) I(\omega_{IR}) \tag{2.2}$$

with

$$\chi_{eff}^{(2)} = [\hat{e}(\omega_{VSFG}) \cdot L(\omega_{VSFG})] \cdot \chi^{(2)} : [L(\omega_{vis}) \cdot \hat{e}(\omega_{vis})] \cdot [L(\omega_{IR}) \cdot \hat{e}(\omega_{IR})] \tag{2.3}$$

Here, $n_1(\omega)$ is the refractive index of the bulk medium 1 at frequency ω, $\hat{e}(\omega)$ is the unit electric field vector, and $L(\omega)$ is the Fresnel factor at frequency ω. (Detailed information on Fresnel factors is presented in section 2.1.2.) The macroscopic second-order nonlinear susceptibility, $\chi^{(2)}$, is comprised of a nonresonant term, $\chi_{NR}^{(2)}$, and a sum of resonant terms, $\chi_{\nu}^{(2)}$, as shown in equation 2.4.

$$\chi^{(2)} = \chi_{NR}^{(2)} + \sum_{\nu} \chi_{\nu}^{(2)} \tag{2.4}$$

A single resonant susceptibility term $\chi_{\nu}^{(2)}$ is described by

$$\chi_{\nu}^{(2)} \propto \frac{A_{\nu}}{\omega_{IR} - \omega_{\nu} - i\Gamma_{\nu}} \tag{2.5}$$

in which A_{ν} is the amplitude of the VSFG transition moment of vibrational mode ν, ω_{ν}

is the center frequency of the transition, and Γ_ν describes the line-width of the transition. When the frequency of the incident infrared photons, ω_{IR}, is resonant with a vibrational mode ν of an interfacial molecule, $\omega_{IR} - \omega_\nu$ approaches zero and thus the value of $\chi_\nu^{(2)}$ increases. Consequently, the resonant susceptibility term $\chi_\nu^{(2)}$ dominates the nonlinear susceptibility $\chi^{(2)}$ for dielectrics and a VSFG intensity enhancement is observed (equation 2.2-2.5).

The macroscopic resonant susceptibility $\chi_\nu^{(2)}$ is a third-rank tensor with 27 individual elements. Thus, $\chi_\nu^{(2)}$ can be denoted as $\chi_{IJK,\nu}^{(2)}$, where I, J and K represent Cartesian coordinates in the laboratory reference frame. $\chi_{IJK,\nu}^{(2)}$ is related to the number density of the interfacial molecules and to the molecular hyperpolarizability:

$$\chi_{IJK,\nu}^{(2)} = N_s \langle \beta_{IJK,\nu}^{(2)} \rangle \tag{2.6}$$

where N_s represents the number density of the interfacial molecules, $\beta_{IJK,\nu}$ represents the molecular hyperpolarizability for vibrational mode ν in the laboratory coordinate system, and $\langle\rangle$ represents an average over the orientational distribution of the molecules. An Euler angle transformation relates the molecular coordinate system (l, m, n) to the laboratory coordinate system (I, J, K)

$$\beta_{IJK,\nu}^{(2)} = \sum_{lmn} \mu_{IJK:lmn} \beta_{lmn,\nu}^{(2)} \tag{2.7}$$

where $\mu_{IJK:lmn}$ is the Euler angle transformation between the laboratory

coordinates and the molecular coordinates. In VSFG, the second-order molecular polarizability is

$$\beta^{(2)} = \beta_{NR}^{(2)} + \sum_{v} \frac{\beta_v}{\omega_{IR} - \omega_v + i\Gamma_v} \tag{2.8}$$

The tensor elements of sum frequency strength factor β_v are related to the Raman and IR properties of the vibrational mode:

$$\beta_{lmn,v} \propto \langle g|\alpha_{lm}|v\rangle\langle v|\mu_n|g\rangle \tag{2.9}$$

Here, *g* refers to the ground vibrational state and *v* refers to the excited vibrational state. α_{lm} represents the Raman polarizability tensor, and μ_n represents the infrared transition dipole moment. $\beta_{lmn,v}$ is nonzero only when both the Raman and the IR transition moments are nonzero. Therefore, a VSFG active vibrational mode must be both Raman and IR active, which is a selection rule for the VSFG process.

2.1.2 Fresnel Factors

The effective sum frequency susceptibility $\chi_{eff}^{(2)}$ (equation 2.3) depends on the experimental polarization and geometry. Under polarization combinations ssp, sps, pss and ppp, $\chi_{eff}^{(2)}$ can be expressed as equation 2.10-2.13.[22,26] Polarization combination, for instance ssp, refers to the polarization of the sum frequency, visible, and infrared photons, respectively. The s-polarized light has its electric field vector perpendicular to the plane

of incidence, while the p-polarized light has its electric field vector parallel to the plane of incidence.

$$\chi^{(2)}_{eff,ssp} = L_{yy}(\omega_{VSFG})L_{yy}(\omega_{vis})L_{zz}(\omega_{IR})\sin\theta_{IR}\chi_{yyz} \tag{2.10}$$

$$\chi^{(2)}_{eff,sps} = L_{yy}(\omega_{VSFG})L_{zz}(\omega_{vis})L_{yy}(\omega_{IR})\sin\theta_{vis}\chi_{yzy} \tag{2.11}$$

$$\chi^{(2)}_{eff,pss} = L_{zz}(\omega_{VSFG})L_{yy}(\omega_{vis})L_{yy}(\omega_{IR})\sin\theta_{VSFG}\chi_{zyy} \tag{2.12}$$

$$\begin{aligned}\chi^{(2)}_{eff,ppp} = &-L_{xx}(\omega_{VSFG})L_{xx}(\omega_{vis})L_{zz}(\omega_{IR})\cos\theta_{VSFG}\cos\theta_{vis}\sin\theta_{IR}\chi_{xxz}\\ &-L_{xx}(\omega_{VSFG})L_{zz}(\omega_{vis})L_{xx}(\omega_{IR})\cos\theta_{VSFG}\sin\theta_{vis}\cos\theta_{IR}\chi_{xzx}\\ &+L_{zz}(\omega_{VSFG})L_{xx}(\omega_{vis})L_{xx}(\omega_{IR})\sin\theta_{VSFG}\cos\theta_{vis}\cos\theta_{IR}\chi_{zxx}\\ &+L_{zz}(\omega_{VSFG})L_{zz}(\omega_{vis})L_{zz}(\omega_{IR})\sin\theta_{VSFG}\sin\theta_{vis}\sin\theta_{IR}\chi_{zzz}\end{aligned} \tag{2.13}$$

The Fresnel factors are functions of the refractive indices of the beam in different media, and the experimental geometry[22,26]

$$L_{xx}(\omega_i) = \frac{2n_1(\omega_i)\cos\gamma_i}{n_1(\omega_i)\cos\gamma_i + n_2(\omega_i)\cos\theta_i} \tag{2.14}$$

$$L_{yy}(\omega_i) = \frac{2n_1(\omega_i)\cos\theta_i}{n_1(\omega_i)\cos\theta_i + n_2(\omega_i)\cos\gamma_i} \tag{2.15}$$

$$L_{zz}(\omega_i) = \frac{2n_2(\omega_i)\cos\theta_i}{n_1(\omega_i)\cos\gamma_i + n_2(\omega_i)\cos\theta_i}\left(\frac{n_1(\omega_i)}{n'(\omega_i)}\right)^2 \tag{2.16}$$

where $n_m(\omega_i)$ is the refractive index of the bulk medium m (m = 1, 2, ′) at frequency ω_i (i = VSFG, vis, IR). One method to determine $n_m(\omega_i)$ at different frequencies is the Kramer-Kronig method, as presented in section 2.3. γ_i is refractive angle into medium 2 defined by Snell's law $n_1(\omega_i)\sin\theta_i = n_2(\omega_i)\sin\gamma_i$. θ_I is the incident or reflection angle from the

interface normal for the beam in consideration. $n'(\omega_i)$ is the effective refractive index of the interface that can be estimated by equation 2.17.[22]

$$\left(\frac{1}{n'(\omega_i)}\right)^2 = \frac{4n_2^{\ 2}(\omega_i)+2}{n_2^{\ 2}(\omega_i)(n_2^{\ 2}(\omega_i)+5)} \tag{2.17}$$

According to equation 2.2, 2.3 and 2.10-2.13, the VSFG intensity is associated with the Fresnel factors. Therefore, when performing the normalization of VSFG spectra, the Fresnel factors should be considered in addition to IR and visible intensities. Appendix A gives an example of normalizing the VSFG spectrum of neat water by using Fresnel factors and the real-time IR profile. The normalized spectrum is compared with the spectrum normalized to IR.

2.2 Raman Spectroscopy: Raman Depolarization Ratio and VSFG Hyperpolarizability Ratio

The Raman depolarization ratio ρ is given by[26-28]

$$\rho = \frac{I_\perp}{I_{II}} = \frac{3\gamma^2}{45\alpha^2+4\gamma^2} \tag{2.18}$$

$I_\perp$ is the intensity of scattered light polarized perpendicular to the incident light, and I_{II} is the intensity of Raman scattering polarized in the same plane as the incident light. α is the mean polarizability, γ is the anisotropy, with

$$\alpha = \frac{1}{3}(\alpha_{aa} + \alpha_{bb} + \alpha_{cc}) \tag{2.19}$$

$$\gamma^2 = \frac{1}{2}[(\alpha_{aa} - \alpha_{bb})^2 + (\alpha_{aa} - \alpha_{cc})^2 + (\alpha_{bb} - \alpha_{cc})^2] \tag{2.20}$$

when considering the symmetric stretching vibration of a C_{3v} group. α_{lm} ($l = m = a, b, c$) is the Raman tensor in the molecular coordinate system.

Combining equation 2.18-2.20,

$$\rho = \frac{3}{4 + 5\left(\frac{2R+1}{R-1}\right)} \quad \text{with} \quad R = \frac{\alpha_{aa}}{\alpha_{cc}} \tag{2.21}$$

According to equation 2.9, the VSFG process is considered to be anti-Stokes Raman scattering of a vibrationally excited state with $\beta_{lmn} \propto \alpha_{lm} \cdot \mu_n$. Therefore, the VSFG hyperpolarizability ratio $\frac{\beta_{aac}}{\beta_{ccc}} = \frac{\alpha_{aa} \cdot \mu_c}{\alpha_{cc} \cdot \mu_c} = \frac{\alpha_{aa}}{\alpha_{cc}} = R$. Equation 2.21 gives the expression for the hyperpolarizability ratio R in terms of the Raman polarization ratio ρ

$$R = \frac{Q-1}{Q+2} \text{ or } R = \frac{Q+1}{Q-2} \tag{2.22}$$

with $Q = \sqrt{\frac{3}{5}\left(\frac{1}{\rho} - \frac{4}{3}\right)}$.

Only one of these two R values from equation 2.22 is physically correct and can be applied to the orientation analysis. Eisenthal et al.[29] developed a method using polarized VSFG measurements to determine the correct R value. Briefly, the macroscopic

susceptibility, χ, is related to the molecular hyperpolarizability, β. In the symmetric stretching vibrational mode of a C_{3v} group, for example, the relationship is given by[26,29]

$$\chi_{xxz}^{SS} = \chi_{yyz}^{SS} = \frac{1}{2} N_s \beta_{ccc} [2R\langle \cos^3 \theta \rangle + (1+R)\langle \sin^2 \theta \cos\theta \rangle] \tag{2.23}$$

$$\chi_{xzx}^{SS} = \chi_{yzy}^{SS} = \frac{1}{2} N_s \beta_{ccc} [(1-R)\langle \sin^2 \theta \cos\theta \rangle] \tag{2.24}$$

where θ is the orientation angle. The relative sign of χ_{xxz} and χ_{xzx} of the symmetric stretch can therefore differentiate whether R is less than or greater than 1. One way to determine the relative sign of the susceptibility elements is through phase studies.[30,31] The polarization method,[29] however, provides an alternative and experimentally easier way to determine the relative sign of χ_{xxz} and χ_{xzx}.

The s-polarized VSFG polarization, P_x^{VSFG}, where

$$P_x^{VSFG} = \chi_{xxz} E_x^{vis} E_z^{IR} + \chi_{xzx} E_z^{vis} E_x^{IR} \tag{2.25}$$

describes the incoming electric field, E, along the indicated axis. The intensities of the s-polarized VSFG were measured with the input visible and IR pulses polarized 45° and parallel to each other, and with the input visible and IR both polarized 45° but perpendicular to each other.[29] In the first case, $E_x^{vis} E_z^{IR}$ and $E_z^{vis} E_x^{IR}$ have the same sign, whereas in the latter case $E_x^{vis} E_z^{IR}$ and $E_z^{vis} E_x^{IR}$ have the opposite sign. Therefore, comparison between the two s-polarized VSFG intensities gives the relative sign of χ_{xxz} and χ_{xzx} (equation 2.25), which in turn can determine the correct R value of equation 2.22.

2.3 Refractive Indices and Kramers-Kronig Relations

The VSFG intensity as well as the Fresnel factors depend on the value of the real refractive indices. One method to extract the refractive indices at different frequencies is the Kramer-Kronig (K-K) method. Infrared spectra are usually plots of the absorbance *A* or the transmittance *T* versus wavenumber. In transmission infrared spectroscopy, absorbance *A* is expressed as equation 2.26 for a given sample thickness *l*, in accord with the Beer-Lambert Law.

$$A = -\log_{10}\frac{I_s}{I_0} = \alpha l \tag{2.26}$$

where I_s is the intensity after passing through the sample, I_0 is the intensity of the incident light, and α is the absorption coefficient which is related to the extinction coefficient *k* by

$$\alpha = \frac{4\pi k}{\lambda} \tag{2.27}$$

k is also the imaginary part of the complex refractive index $\tilde{n}$:

$$\tilde{n} = n + ik \tag{2.28}$$

n is often called the refractive index, which follows Snell's law $n_1 \sin\theta_1 = n_2 \sin\theta_2$; *k* represents the damping of an electromagnetic wave inside the material. Both *n* and *k* are functions of wavelength λ.

Based on equation 2.26 and 2.27, at a certain wavelength λ, the dominant factor that affects the absorbance is the imaginary refractive index *k*. However, the real part

n of the refractive index also plays a role in the absorption process. Physically, the refractive index of a material is a function describing the response of the material to the applied electromagnetic radiation. The real part n and the imaginary part k are therefore not wholly independent but are connected by the Principle of Causality which is formulated mathematically by the K-K relations:[32-35]

$$n(\nu') - n_{\infty} = \frac{2}{\pi} P \int_0^{\infty} \frac{\nu k(\nu)}{\nu^2 - \nu'^2} d\nu \tag{2.29}$$

$$k(\nu') = -\frac{2\nu'}{\pi} P \int_0^{\infty} \frac{n(\nu)}{\nu^2 - \nu'^2} d\nu \tag{2.30}$$

Here ν is the wavenumber. P refers to the Cauchy principle value. The integral in equation 2.29 and 2.30 is considered as a Cauchy principle value because of the possible singularity at $\nu = \nu'$ (improper integral).

K-K relations can be employed to determine the real and imaginary parts of the complex refractive index.[33,34] The Beer-Lambert Law (equation 2.26 and 2.27) allows us to estimate a value of $k(\nu)$ for each wavenumber from the absorbance spectrum in the zeroth approximation. The approximate $k(\nu)$ values are K-K transformed to obtain the values of the real refractive index $n(\nu)$. Then, the approximate $k(\nu)$ and $n(\nu)$ values are used to calculate an absorbance spectrum. The new absorbance spectrum is compared with the original experimental spectrum and $k(\nu)$ values are adjusted. The updated $k(\nu)$ values are then employed to calculate better approximations to $n(\nu)$. These steps are iterated until $k(\nu)$ and $n(\nu)$ become constant.

In the case of reflection infrared spectroscopy, the procedure of determining the real and imaginary refractive indices is somewhat different.[36] Generally speaking, for transmission spectroscopy, the imaginary part k is estimated from experiments and the real part n is obtained by the K-K relation, as discussed above, whereas for reflection spectroscopy, the intensity is measured and the phase is calculated by the K-K relation.

In a reflection spectrum, the measured reflectance R is the power ratio of reflected light to incident light.[37] R corresponds to the absolute square of the reflection coefficient[36,37]

$$R = |r|^2 \tag{2.31}$$

At normal or near-normal incidence and when one medium is air (or vacuum),[36,37]

$$r = \frac{\tilde{n} - 1}{\tilde{n} + 1} \tag{2.32}$$

$\tilde{n}$ is the complex refractive index as shown in equation 2.28. Thus, r is also complex with modulus $|r|$ and phase θ, $r = |r|e^{i\theta}$. By incorporating equation 2.31, we obtain

$$r = |r|e^{i\theta} = \sqrt{R}e^{i\theta} = \sqrt{R}\cos\theta + i\sqrt{R}\sin\theta \tag{2.33}$$

$$\ln r = \frac{1}{2}\ln R + i\theta \tag{2.34}$$

The imaginary part θ correlates with the experimentally measured reflectance R by a K-K relation[32,36]

$$\theta(\nu') = -\frac{\nu'}{\pi} P\int_0^\infty \frac{\ln R(\nu)}{\nu^2 - \nu'^2} d\nu \tag{2.35}$$

From equation 2.28 and 2.32, r can be expressed as a function of real (n) and imaginary (k) refractive indices:

$$r = \frac{n^2 + k^2 - 1}{(n+1)^2 + k^2} + i\frac{2k}{(n+1)^2 + k^2} \tag{2.36}$$

By comparing 2.33 and 2.36, n and k are associated with R and θ:

$$\frac{n^2 + k^2 - 1}{(n+1)^2 + k^2} = \sqrt{R}\cos\theta \tag{2.37}$$

$$\frac{2k}{(n+1)^2 + k^2} = \sqrt{R}\sin\theta \tag{2.38}$$

Therefore, in the near-normal reflection spectroscopy, the real and imaginary refractive indices are estimated using the measured reflectance and the calculated phase from K-K.

CHAPTER 3

EXPERIMENTAL

3.1 Scanning Vibrational Sum Frequency Generation Instrumentation

Two scanning VSFG systems, both available in the Allen lab, were used in the studies presented in this dissertation. The VSFG scanning systems, described as the 20 Hz and the 10 Hz systems, are described below. Additional details of these two systems can be found in previous publications.[38-40] In both scanning VSFG systems, the VSFG spectra were acquired using a visible beam at 532 nm and a tunable infrared beam.

The 20 Hz scanning VSFG system was utilized for the study of vibrational modes of interfacial nitrate ions. In the 20 Hz VSFG system, the 532 nm visible pulse is generated by doubling the frequency (second harmonic) of the 1064 nm pump source from an Nd:YAG laser (27 ps pulse duration and 20 Hz repetition rate, EKSPLA, PL 2143A/20/SS). The infrared pulse tunable from 1000 cm^{-1} to 4000 cm^{-1} with spectral width < 6 cm^{-1} is generated from an optical parametric generator (EKSPLA, PG401/DFG2-16P). The 532 nm visible beam is focused 40 mm after the sample surface by a plano convex lens (700 mm focal length). At the sample surface the 532 nm beam has a diameter of 1 mm and an intensity of ~400 μJ/pulse. The infrared beam is focused at the sample surface by using a ZnSe lens (50 mm focal length) to yield a < 0.5 mm

beam diameter of the infrared light at the sample surface with an intensity of ~40 μJ/pulse at 1050 cm^{-1}. The input angles of the 532 nm and infrared beams are 60° and 55° from the surface normal, respectively. The 532 nm and infrared pulses are overlapped at the interface spatially and temporally. After the sample stage, a series of mirrors and irises are used to separate the VSFG signal and the 532 nm beam, followed by a Glan Thompson, a halfwave plate, and a notch filter to further filter out scattered 532 nm light and to change the VSFG polarization. The VSFG signal is focused to the monochromator by using a 200 mm focusing lens. After filtration in the monochromator, sum frequency light is collected using a cooled charge-coupled device (CCD) camera (Andor Technology, DV412).

The 10 Hz scanning VSFG system was employed to study vibrational modes in the OH stretching region of water and the CH and NH stretching regions of ethylenediamine. The 10 Hz system uses a pulsed Nd:YAG laser (29 ps pulse duration and 10 Hz repetition rate, ESKPLA, PL 2143A/SS) that pumps a KTP-KTA based optical parametric generator/amplifier (LaserVision). The mid-infrared beam generated is tunable from 2500 cm^{-1} to 4000 cm^{-1} with a bandwidth of 4-8 cm^{-1} and energy of 200-500 μJ/pulse at the sample surface, depending on the spectral region. The 532 nm visible beam is ~550 μJ/pulse at the sample surface. The input angles are set to 45° and 53° from the surface normal for the 532 nm and infrared beams, respectively. A cooled CCD camera (Andor Technology, DV887ECS-BV) is utilized to collect the VSFG signal. An

iris, a Schott glass filter (BG 25, CVI Laser), a short pass filter (SPF500, CVI laser), and two holographic notch plus filters (Kaiser Optical System, Inc.) are used before the CCD camera to block the 532 nm scattered light.

Both scanning VSFG systems were calibrated using a polystyrene thin film and the non-resonant VSFG spectra of a gold surface. The calibration spectrum was collected by placing a thin film of polystyrene, whose infrared absorbances are well known, in the path of the infrared beam prior to beam overlap on the gold surface. The resultant infrared beam is structured due to absorbance by the polystyrene film, which leads to a structured non-resonant VSFG spectrum of gold. The peak positions (dips) in the calibration VSFG spectrum are used to calibrate the VSFG spectra. To ensure the stability of the VSFG system and to confirm the reproducibility of the spectra, VSFG spectra of neat water or an 8.0 mM sodium dodecyl sulfate (SDS) solution were also obtained at the beginning and the end of daily experiments.

All VSFG spectra presented in this dissertation are plots of the sum frequency intensity versus the incident infrared frequency, and are the average of three to six replicate spectra. The VSFG spectra were normalized to IR profiles detected in real time with VSFG.

3.2 Raman Instrumentation

Raman spectra were obtained by passing an unpolarized 532 nm light (Spectra-Physics, Millennia II) or 785 nm light (Raman System Inc) from a continuous wave laser onto the sample using a 5 mm or 7.5 mm focusing Raman probe (InPhotonics), depending on the experiment. The Raman scatter was focused onto the entrance slit of a 500 mm monochromator (Acton Research, SpectroPro SP-500) through a fiber optic imaging coupler (Acton Research, FC-446-030), dispersed by a 600 groove/mm grating blazed at 1 μm, and collected on a liquid nitrogen cooled CCD camera (Roper Scientific, LN400EB, 1340 × 400 pixel array, back-illuminated and deep depletion CCD). The power of the 532 nm beam for sample illumination was ~100 mW, and the power of the 785 nm beam was ~240 mW. The slit width of the monochromator entrance slit was set to 50 μm, and the resolution was 3.2 cm^{-1}. Raman spectra were collected with an exposure time of 50 s. Before data collection, the monochromator was calibrated using the 435.833 nm Hg line of a fluorescent light, and was verified by comparison to the Raman spectrum of crystalline naphthalene.

In the Raman setup, a Raman probe (Inphotonics) was employed to illuminate the sample and to filter and collect the scattered radiation. In order to study the metal-nitrate interaction which has intermolecular vibrational bands at ~250 cm^{-1} or lower, a Raman setup that can detect lower frequencies was designed and utilized. Details of the low frequency Raman instrumentation are presented in Appendix B. In the obtained low-

frequency Raman spectra, the interference of water-water hydrogen bonding hinders direct interpretation of low-frequency Raman spectra of the nitrate aqueous solutions. Therefore, in this dissertation, discussions are focused on the nitrate vibrational modes in the region 300 cm^{-1} to 4000 cm^{-1} acquired using the Raman probe.

3.3 FTIR Instrumentation

A Thermo Nicolet Fourier transform infrared (FTIR) spectrometer (Thermo Electron Corporation, Avatar 370) was employed to acquire attenuated total reflection Fourier transform infrared (ATR-FTIR) spectra. ATR-FTIR instead of transmission FTIR was used as a bulk probe for ease of comparison. IR penetration depth for ATR-FTIR is on the order of the wavelength of the incident light, and the IR absorption is therefore dominated by the bulk. We have assumed that the refractive indices of aqueous solutions are relatively constant. A 45º single-bounce ZnSe crystal trough mounted on an accessory (Thermo Electron Corporation, Smart SpeculATR) was employed to collect spectra at a spectral resolution of 4 cm^{-1}. The obtained ATR-FTIR spectra will be referred as IR spectra in future chapters. All IR spectra shown in this dissertation were averaged over 128 scans.

3.4 Curve-Fitting Analysis

When several overlapping peaks contribute to a spectral intensity, it is difficult to assign the accurate peak positions. Curve-fitting techniques were used to determine the positions, amplitudes, and areas of the component peaks of a spectrum. The VSFG spectra were fit with the peak-fitting function in IgorPro 4.05A software (WaveMetrics, Inc.) using a home-written program to incorporate phase.[41] The mathematical model describing the profile of bands was the Lorentzian model. The VSFG intensity I_{VSFG} is proportional to the absolute square of the summation of resonant $\chi_{v}^{(2)}$ and nonresonant $\chi_{NR}^{(2)}$ susceptibility terms, as shown in equation 2.2 to 2.4. Unlike Raman and IR, VSFG is coherent. The relative phase of the VSFG response for each overlapping vibrational mode can have a profound effect on the shape of the resultant VSFG spectra, and therefore was included in the curve-fitting process of the VSFG spectra. When performing the curve-fitting analysis, input of the following parameters was required: two non-resonant terms (real and imaginary), peak amplitudes and phases, peak positions, and peak widths for each component peak. Since a VSFG active vibrational mode must be both Raman and IR active, Raman and IR spectra of the chemicals of interest were acquired before the VSFG curve-fitting analysis. By performing curve-fits on the Raman and IR spectra, the number of peaks, peak positions and peak widths of Raman and IR active modes were obtained. These peak parameters were used as references for the initial

guess in the VSFG curve-fitting process.

The curve-fitting analysis of the Raman and IR spectra was conducted using the multipeak fitting function in IgorPro 4.05A, with the Voigt line shape and the background subtraction option enabled. In order to properly compare the fitting results, the best-fit Voigt line shapes were held to be relatively constant.

CHAPTER 4

NITRATE IONS AND ION PAIRING IN AQUEOUS SOLUTIONS

Ion pairing, the association of oppositely charged ions in electrolyte solutions to form distinct chemical species, ion pairs, is of prime importance in many areas including solution chemistry, environmental chemistry, geochemistry, and biology.[20,42-45] Ion pairs are classified as three types: solvent-separated ion pairs (SSIPs) where the primary solvation shells of the cation and the anion remain intact, solvent-shared ion pairs (SSHIPs) when a single solvent layer exists between the cation and the anion, and contact ion pairs (CIPs) when no solvent exists between the ion partners of the pair and ions are in direct contact.[42,46] Ion pairing in systems containing nitrate anion, an environmentally and biologically important ion, has attracted considerable interest.[6,10,19,21,47-49] The formation of ion pairs with a counter cation changes the environment of the nitrate anion. This has implications for surface reactivity and reaction mechanism in atmospheric and geochemical systems.

This chapter presents a Raman spectroscopic study of ion pairing in aqueous solutions between nitrate anions and divalent metal cations, Mg^{2+}, Ca^{2+}, Sr^{2+}, and Pb^{2+}, from 0.1 m to saturated concentrations at room temperature. Ammonium nitrate solutions that give little indication of disturbance of the nitrate anion by the cation are studied for

comparison.[50] Raman spectra of nitrate vibrational modes are interpreted carefully to elucidate effects of different divalent cations. IR experiments were also conducted, complementing the Raman study. The work presented in this chapter is different from previous research in that other research[51-55] has mainly focused on individual metal-nitrate salts and few studies[45,51,56,57] have been conducted to understand relative differences between different cations with nitrate. In the present work we elucidate effects of different metal dications, Mg^{2+}, Ca^{2+}, Sr^{2+}, and Pb^{2+}, on metal-nitrate ion pairing by a comprehensive spectroscopic study.

4.1 Material

All nitrate salts, $Mg(NO_3)_2 \cdot 6H_2O$ (Certified ACS, 98.0-102.0%), $Ca(NO_3)_2 \cdot 4H_2O$ (Certified ACS, 99.0-103.0%), $Sr(NO_3)_2$ (Certified ACS, 99.0%), and $Pb(NO_3)_2$ (Certified ACS, 99.0%) were purchased from Fisher Scientific and were used as received. The aqueous solutions were made using Nanopure water with resistivity 18.0-18.3 MΩ cm.

Molality (m), which is defined as the moles of solute per kg of water, is used as the concentration unit for the nitrate salt solutions in this chapter. Table 4.1 shows the concentrations of the aqueous solutions in molality (m), mole fraction (m.f.), and moles per liter (M).

4.2 Experimental Method

The Raman spectrometer with a 785 nm continuous wave laser (Raman System Inc) was employed as the primary instrument for the work presented in this chapter. The power of the 785 nm illumination light was ~240 mW. The slit width of the monochromator entrance slit was set to 50 μm, the grating used was 600 groove/mm, and the resolution was 3.2 cm^{-1}. Raman spectra were collected with an exposure time of 50 s. Detailed information of Raman and IR instrumentation can be found in section 3.2 and 3.3.

4.3 Results and Discussion

Raman spectra were obtained from metal-nitrate aqueous solutions that ranged in concentration from 0.1 m to saturation at room temperature. The Raman spectra of saturated $Mg(NO_3)_2$, $Ca(NO_3)_2$, $Sr(NO_3)_2$, and $Pb(NO_3)_2$ solutions are shown in Figure 4.1. There are three nitrate vibrational bands in the spectra shown in the right panel of Figure 4.1: in-plane deformation (IPD) modes at ~719 cm^{-1}, symmetric stretching (SS) modes at ~1049 cm^{-1} (also shown in the inset of Figure 4.1), and asymmetric stretching (AS) modes at ~1370 cm^{-1}. In the saturated solution of $Mg(NO_3)_2$, the nitrate IPD occurs as a well defined single peak, whereas peak splitting or an asymmetric peak shape of the IPD is observed for $Ca(NO_3)_2$, $Sr(NO_3)_2$, and $Pb(NO_3)_2$. For the nitrate SS modes shown in Figure 4.1 and the inset, the frequency differences between $Pb(NO_3)_2$ and other nitrate

solutions are observed. In the case of the AS modes, small variations are observed for different divalent cation-nitrate saturated solutions. The left panel of Figure 4.1 shows the Raman spectra of the intermolecular metal-water vibrational modes, which will be discussed later.

The spectral features of the nitrate vibrational bands arise from the symmetry changes of nitrate. Unperturbed nitrate ion has a D_{3h} symmetry and is expected to exhibit a four-band spectrum: SS band $\nu_1(A_1')$ at ~1049 cm^{-1}, out-of-plane deformation (OPD) band $\nu_2(A_2'')$ at ~830 cm^{-1}, AS $\nu_3(E')$ at ~1370 cm^{-1}, and IPD $\nu_4(E')$ at ~719 cm^{-1}.[51,58,59] The AS and IPD modes are both Raman and IR active, while the SS is Raman active only and the OPD is IR active only. In aqueous solutions, the perturbation from metal cations and water molecules causes a lowering of nitrate symmetry from D_{3h} to C_{2v} or C_s, resulting in more vibrational bands.[51,52,58] Vibrational bands in the SS and OPD regions become both Raman and IR active, with frequencies similar to those of unperturbed nitrate. As shown in Figure 4.2, the nitrate SS peak occurs in the IR spectra of the metal-nitrate aqueous solutions and this peak amplifies as concentration increases. In the AS region two bands are expected to arise from the lifting of degeneracy of the AS band as the nitrate symmetry lowers, and two bands in the IPD region arise from the lifting of degeneracy of the IPD. These are in accord with the results of our Raman spectra (Figure 4.1, for instance). Two AS bands at ~1345 cm^{-1} and ~1420 cm^{-1} are observed in Raman spectra of the nitrate aqueous solutions. Two IPD bands instead of one IPD band are present in the

Raman spectra of $Ca(NO_3)_2$, $Sr(NO_3)_2$, and $Pb(NO_3)_2$ solutions. The OPD band cannot be observed in the Raman spectra of our concentration range. In the following paragraphs, the spectral changes of the IPD, the SS, and the AS bands will be discussed in detail.

In-plane deformation. The splitting of the nitrate IPD band has been used as a criterion for the CIP formation.[45,56,59-61] The Raman spectra of the nitrate IPD modes of NH_4NO_3, $Mg(NO_3)_2$, $Ca(NO_3)_2$, $Sr(NO_3)_2$, and $Pb(NO_3)_2$ are shown in Figure 4.3. The Raman spectra of NH_4NO_3 solutions, in which the Coulombic perturbation of ammonium cation on nitrate is relatively small, are shown for comparison. In the spectra of NH_4NO_3 solutions (Figure 4.3a), neither peak splitting nor frequency shift is observed, consistent with the fact that nitrate is relatively "free" from NH_4^+ in aqueous solutions. As for $Mg(NO_3)_2$ solutions, spectra in Figure 4.3b show no obvious peak splitting of the IPD in our concentration range, but an increase in the band width, suggesting a low degree of CIPs in the $Mg(NO_3)_2$ solutions.[57,61] The slight frequency shift of the IPD band to higher frequency (~1 cm^{-1}) with increasing concentration of $Mg(NO_3)_2$ indicates the presence of SSHIPs and/or SSIPs.[59] The IPD band is not sensitive enough to differentiate between SSHIPs and SSIPs. Detailed information of peak frequencies and areas is shown in Table 4.2. In the aqueous solutions of $Ca(NO_3)_2$, $Sr(NO_3)_2$, and $Pb(NO_3)_2$ (Figure 4.3c-e), nitrate exhibits a single peak at 720 ± 1 cm^{-1} at concentration lower than 0.5 m. The single IPD peak implies no or low degree of CIP formation between metal cations and nitrate anions. As the concentration increases to 1.0 m, a shoulder appears at 738 cm^{-1},

732 cm^{-1}, and 728 cm^{-1} for $Ca(NO_3)_2$, $Sr(NO_3)_2$, and $Pb(NO_3)_2$, respectively (Figure 4.3c-f). With further increase in the concentration, this high frequency shoulder gradually increases in intensity, and shifts to higher frequency. Notice here the high frequency side of the IPD band for $Pb(NO_3)_2$ is at a lower frequency compared to $Ca(NO_3)_2$ and $Sr(NO_3)_2$ (729 cm^{-1} versus 740 cm^{-1} and 735 cm^{-1} in saturated solutions, for example). This may reflect differences in the polarizing power of the cations.[45] The value 729 cm^{-1} is still within the range assigned to CIPs in aqueous solutions. Therefore, we assign the low frequency component peak at ~718 cm^{-1} to the hydrated nitrate ions, containing SSIPs and/or SSHIPs, and the high frequency component peak at 728-740 cm^{-1} to the contact ion paired (CIPd) nitrate ions.

Figure 4.4a shows the relative peak intensity of the CIPd nitrate (the ratio of the intensity of the ~740 cm^{-1} peak to the sum intensity of the ~720 cm^{-1} peak and the ~740 cm^{-1} peak) as a function of concentration for different metal-nitrate solutions. The relative peak intensity has been used to estimate the percentage of the CIPd species in previous studies, assuming that the molar Raman intensity remains the same for free and ion paired forms of nitrate.[45,56] Figure 4.4b reveals a linear correlation between the sum intensity of the nitrate IPD bands and the molarity, which implies that the IPD intensity is not sensitive to the relative amount of free or ion paired species. Therefore the assumption used by Fleissner et al. is reasonable and the relative amount of the CIPd nitrate species is then extracted from Figure 4.4a. For example, at concentration 3.3 m

there are 24% CIPd nitrate and 76% hydrated nitrate (may include SSIP and SSHIP) in the $Ca(NO_3)_2$ solution. This is consistent with Irish and Walrafen.[51] When comparing different divalent metal-nitrate solutions with the same concentration, the degree of CIP follows: $Pb(NO_3)_2 > Sr(NO_3)_2 > Ca(NO_3)_2 > Mg(NO_3)_2$. For instance, at concentration 1.7 m, 45% of nitrate in the $Pb(NO_3)_2$ solution is CIPd, and this number decreases to 31% for $Sr(NO_3)_2$, 20% for $Ca(NO_3)_2$, and almost no CIP for $Mg(NO_3)_2$. The trend for $Sr(NO_3)_2$, $Ca(NO_3)_2$, and $Mg(NO_3)_2$ in aqueous solutions agrees with Chang and Irish's studies,[51,57] though in the glassy state the trend has been found to be $Sr(NO_3)_2 > Ca(NO_3)_2 \approx Mg(NO_3)_2$.[45]

Hydration by water molecules competes with cation-anion ion pairing.[44,62,63] Having a large ionic radius and a small surface charge density, Pb^{2+} binds to water molecules relatively loosely compared to other dications. Therefore, it is relatively easy for nitrate to enter the first hydration shell of Pb^{2+} to form CIPs. Mg^{2+}, on the other hand, has a small ionic radius and a large surface charge density. The hydrated ions of $Mg(H_2O)_6^{2+}$ are thus very stable.[64] As shown in the left panel of Figure 4.1, the intermolecular metal-water band at ~350 cm^{-1} predominates in the Raman spectrum of the $Mg(NO_3)_2$ aqueous solution, indicating strong hydration of Mg^{2+} cations. Water molecules of the Mg^{2+} hydration shell compete against the nitrate anion successfully. Hence, a relatively low degree of CIP is present in the $Mg(NO_3)_2$ aqueous solutions at room temperature. This is consistent with results from the Raman IPD modes; the CIP formation between divalent

metal cations and nitrate anions decreases with increasing ionic surface charge density: $Pb^{2+} > Sr^{2+} > Ca^{2+} > Mg^{2+}$.

Symmetric stretch. The variation of the full width at half maximum (fwhm) and the frequency of the nitrate SS band indicate the perturbation of metal cations on nitrate anions via hydration water molecules. Figure 4.5 shows the Raman spectra of the nitrate SS modes. Detailed fwhm and frequency values are listed in Table 4.3. As the concentration increases from 0.5 m to saturate, the fwhm of the nitrate SS band increases 10-20% for divalent metal-nitrate solutions (Figure 4.5b-e, Table 4.3). For comparison, in the case of NH_4NO_3 aqueous solutions, the SS fwhm variation is below 5% (Figure 4.5a, Table 4.3). Vollmar[65] has suggested that the increase in the fwhm is caused by the breaking down of the solution structure, creating a more disordered environment for the nitrate ions. In the studies of $Zn(NO_3)_2$ at high temperatures and pressures, it has been proposed that the bound (ion-paired) nitrate species relaxes faster than the free species, resulting in a larger bandwidth of the bound species.[56,66] The increase in bandwidth (Figure 4.5b-e) therefore can be explained by the interaction of the cation with the nitrate anion, which causes faster relaxation. Nitrate and its counter cation have a stronger tendency to form ion pairs at higher concentrations and, consequently, the long-range Coulombic perturbation of metal cations on nitrate anions broadens the SS band. When comparing different nitrate solutions with the same nitrate concentration (Figure 4.5f-g), the fwhm follows a trend $Pb(NO_3)_2 > Sr(NO_3)_2 \approx Ca(NO_3)_2 > Mg(NO_3)_2 > NH_4NO_3$. For

instance, the fwhms are 13.0 cm^{-1}, 11.1 cm^{-1}, 11.0 cm^{-1}, 10.5 cm^{-1}, and 8.0 cm^{-1} for $Pb(NO_3)_2$, $Sr(NO_3)_2$, $Ca(NO_3)_2$, $Mg(NO_3)_2$, and NH_4NO_3, at molaility 1.7 m (NH_4NO_3 has concentration 3.4 m). This trend implies strong Coulombic effects of Pb^{2+} on nitrate relative to Sr^{2+}, Ca^{2+}, and Mg^{2+}. Nitrate is almost free from NH_4^+ Coulombic effects.

Peak position of the nitrate SS band is also concentration dependent and cation dependent. For $Mg(NO_3)_2$, $Ca(NO_3)_2$, and $Sr(NO_3)_2$ aqueous solutions, the frequency slightly blue shifts from 1049 cm^{-1} at 0.1 m to 1050 cm^{-1} at saturated concentrations (Figure 4.5b-d). Interestingly, the SS frequency red shifts as concentration increases in $Pb(NO_3)_2$ solutions (Figure 4.5e). For different salt solutions with the same concentration, the peak position of $Pb(NO_3)_2$ is always at lower frequency compared to other metal cations (Figure 4.5f-g). Similar shifts of the SS band are observed in the infrared spectra (Figure 4.2; peak positions of the SS in the IR spectra are listed in Table 4.4).

The blue shift of the SS band for $Mg(NO_3)_2$, $Ca(NO_3)_2$, and $Sr(NO_3)_2$ and the red shift for $Pb(NO_3)_2$ can be interpreted by two competitive forces: the weakening of the nitrate-water hydrogen-bonding that causes a SS blue shift, and the ion pairing between metal cation and nitrate that results in a red shift of the SS. On one hand, metal cations in aqueous solutions interact with or even replace water molecules around nitrate, resulting in a weakening of the nitrate-water hydrogen-bonding. Nitrate-water hydrogen-bonding (water solvation) usually decreases the frequency of the nitrate SS vibration.[65] Therefore, the weakening of the nitrate-water hydrogen-bonding leads to a blue shift of the nitrate

SS band. On the other hand, the strong cation-nitrate interaction weakens the covalent N-O bond, and causes a red shift of the nitrate SS band[66]. In the case of $Mg(NO_3)_2$, $Ca(NO_3)_2$, and $Sr(NO_3)_2$ solutions, the effects of weakening nitrate-water hydrogen-bonding dominate. Consequently, the nitrate SS band blue shifts as concentration increases in their aqueous solutions. Similar frequency shifts have been observed in previous studies of nitrate and sulfate.[45,59,63,65,67,68] For $Pb(NO_3)_2$ aqueous solutions, however, the effects of metal-nitrate interaction dominate. Having a large ionic radius and a relatively small surface charge density, Pb^{2+} binds water molecules relatively loosely compared to other dications used in this study. The Coulombic perturbation of Pb^{2+} on nitrate exceeds the effect of nitrate-water hydrogen-bond weakening. Similar red shifts have been observed for $Pb(NO_3)_2$-N-methylacetamide solutions and $Zn(NO_3)_2$ aqueous solutions.[56,66,69] In the case of $NaNO_3$, though the surface charge density of Na^+ is smaller than that of Pb^{2+} (0.76 vs. 1.12), a blue shift rather than a red shift is observed, as shown in Figure 4.6. This phenomenon reflects the differences between monovalent and divalent metal ions. Low surface charge density of Na^+ leads to weak Na^+-water binding. Meanwhile, the Na^+-nitrate interaction is even weaker as a result of the single charge of Na^+ cations. It is the relative strengths of these two competitive effects that dictate the direction of the frequency shift of the nitrate SS band.

Asymmetric stretch. Unperturbed nitrate gives rise to a single asymmetric stretching ν_3(E') band at ~1370 cm^{-1}.[49,53,61] In the aqueous nitrate solutions, two AS component

peaks are observed, as shown in Figure 4.1 and 4.7. Unlike the IPD modes, the degeneracy of the AS modes is caused by perturbation from water molecules as well as long-range Coulombic perturbation from cations.[53,59-61,69] *Ab initio* calculations on isolated complexes of nitrate ion with a single water molecule have identified two structures with C_{2v} and C_s symmetries. In both symmetries the two component peaks of the AS are separated by ~50 cm^{-1}, which is consistent with the minimal splitting in dilute aqueous solutions detected by previous experimental studies.[49,70,71] In the present study, the separation of the two component peaks varies from 63 cm^{-1} for 0.5 m $Mg(NO_3)_2$ to 90 cm^{-1} for saturated $Pb(NO_3)_2$ (Figure 4.7a-g), suggesting the cation Coulombic effects on nitrate. Detailed peak separation values are listed in Table 4.5. (In the aqueous solutions of NH_4NO_3, the separation is in the range 63 to 69 cm^{-1}, which may suggest that nitrate is not totally but relatively free from the Coulombic effects of NH_4^+.) It is important to note that effects from cations and water molecules coexist in aqueous solutions, and the perturbation from water varies as concentration changes. The peak separation of the nitrate AS modes is therefore not an accurate measurement for the strength of ion pairing. However, considering the magnitude of the difference, $Pb(NO_3)_2$ has the largest peak separation among these metal-nitrate solutions (Figure 4.7f-g). We therefore conclude that Pb^{2+} has the strongest tendency to form ion pairs with nitrate compared to the other cations in this work. This is consistent with the results from the IPD and the SS modes discussed above.

4.4 Conclusions

Studies of the divalent metal-nitrate aqueous solutions, $Mg(NO_3)_2$, $Ca(NO_3)_2$, $Sr(NO_3)_2$, and $Pb(NO_3)_2$, were conducted using Raman and infrared spectroscopies. The perturbation of metal-nitrate ion pairing and water hydration lowers the symmetry of nitrate. Therefore peak shifting, splitting, and broadening are observed in the Raman and IR spectra of the nitrate aqueous solutions. Analysis of the spectral features reveal that Pb^{2+} has a strong tendency to form ion pairs with nitrate relative to Sr^{2+}, Ca^{2+}, and Mg^{2+}, and contact ion pair formation decreases with decreasing cation size and increasing cation charge density: $Pb^{2+} > Sr^{2+} > Ca^{2+} > Mg^{2+}$. The effects of Mg^{2+} and Ca^{2+} on ion paring are significantly different. Recent molecular dynamics simulations[72] showed that the contact ion pairing in $Mg(NO_3)_2$ is thermodynamically unfavorable because there is a large activation barrier to remove water from the first hydration shell of Mg^{2+} and to form a contact ion pair; whereas in $Ca(NO_3)_2$ the contact ion pairing is preferred over the solvent-shared and solvent-separated ion pairing due to the low free energy of the contact ion pair formation. This provides thermodynamic support to our spectroscopic results.

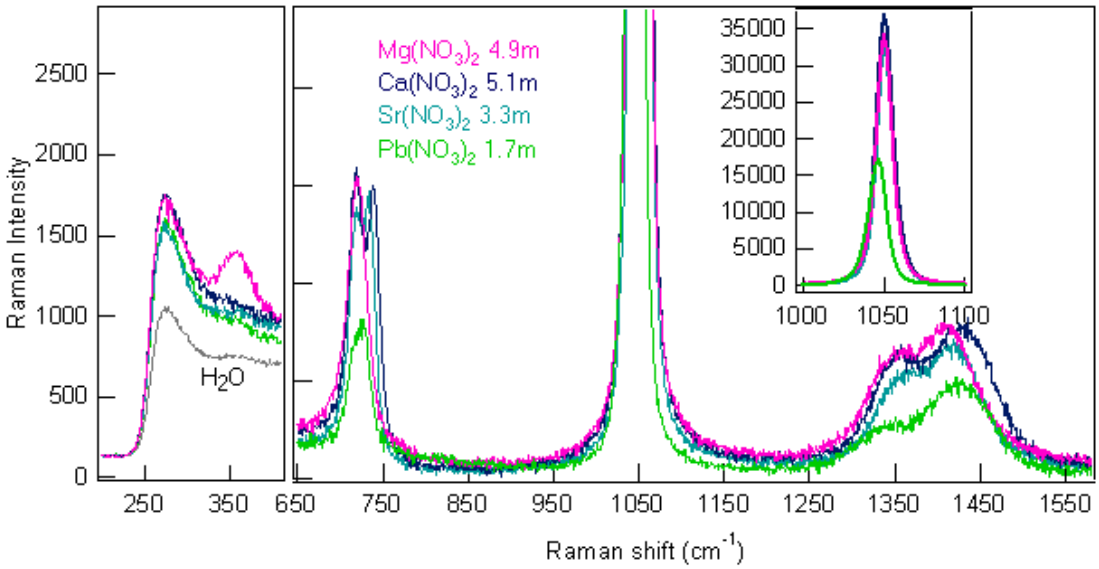

Figure 4.1 Raman spectra of saturated aqueous solutions of $Mg(NO_3)_2$, $Ca(NO_3)_2$, $Sr(NO_3)_2$, and $Pb(NO_3)_2$. The inset: Raman spectra of the nitrate symmetric stretch modes. Water spectrum is shown in gray in the left panel for comparison.

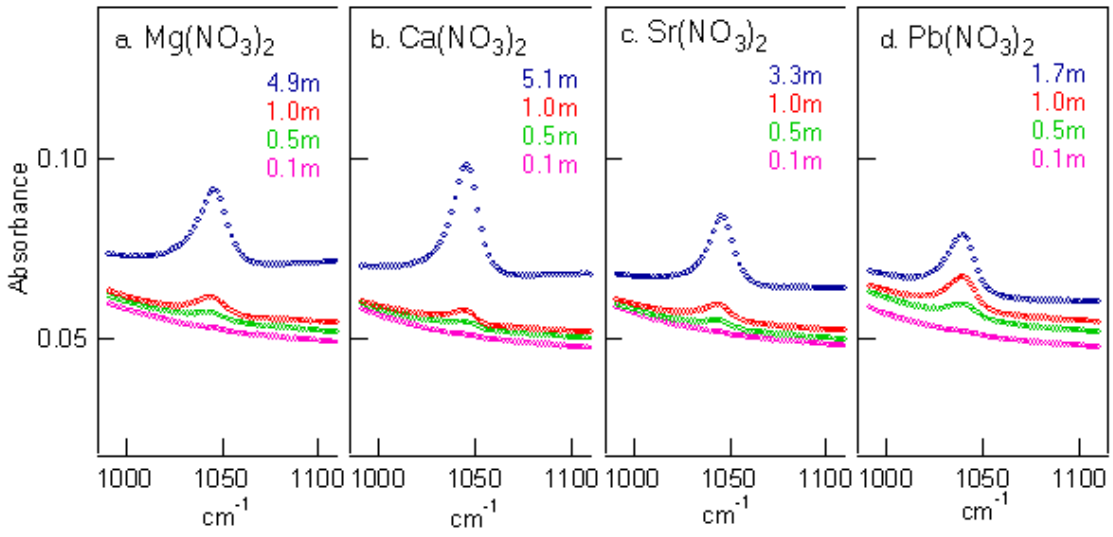

Figure 4.2 IR spectra of nitrate symmetric stretching modes: a) $Mg(NO_3)_2$ solutions; b) $Ca(NO_3)_2$ solutions; c) $Sr(NO_3)_2$ solutions; d) $Pb(NO_3)_2$ solutions.

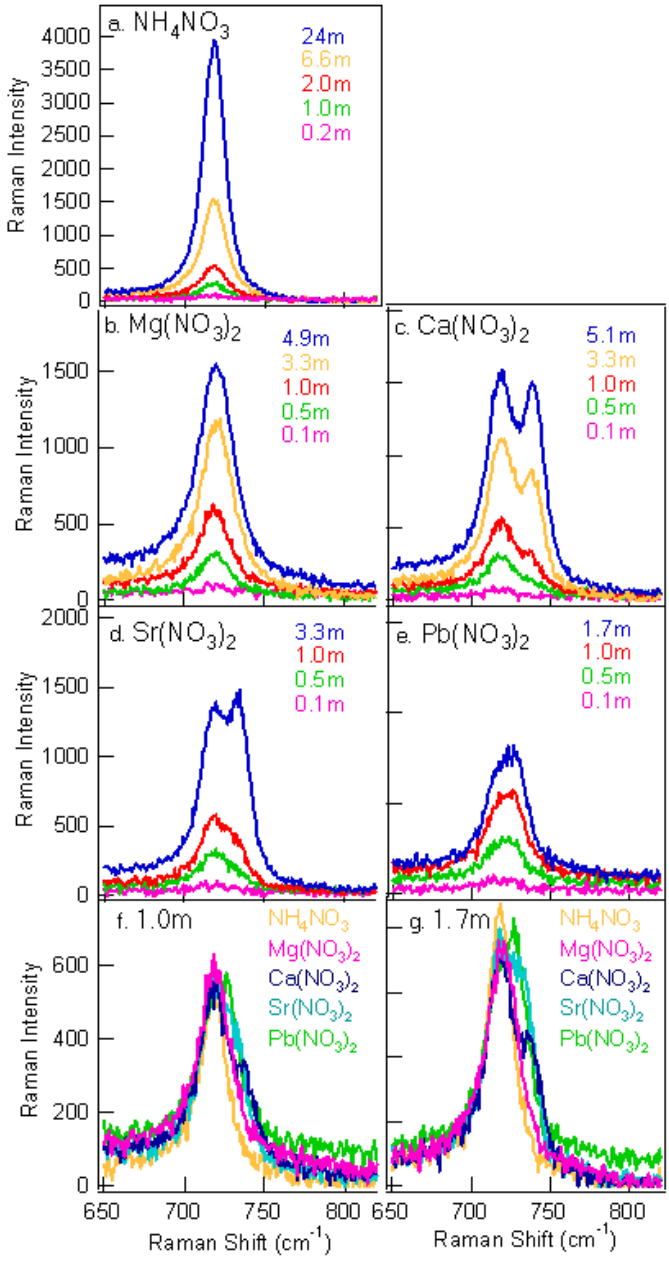

Figure 4.3 Raman spectra of nitrate in-plane deformation modes: a) NH_4NO_3 solutions; b) $Mg(NO_3)_2$ solutions; c) $Ca(NO_3)_2$ solutions; d) $Sr(NO_3)_2$ solutions; e) $Pb(NO_3)_2$ solutions; f) 1.0 m solutions; g) 1.7 m solutions. In panel f) and g), NH_4NO_3 has the same nitrate concentrations with divalent metal-nitrate solutions, i.e. 2.0 m and 3.4 m respectively.

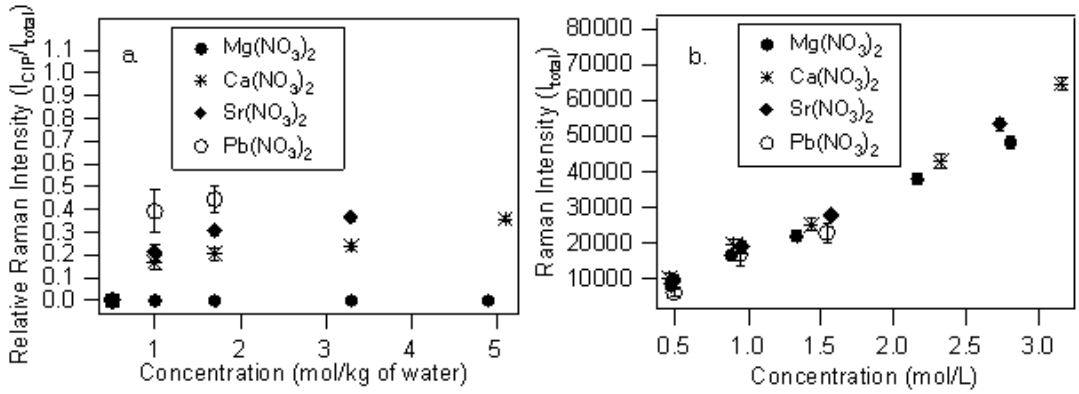

Figure 4.4 Raman intensities of nitrate in-plane deformation modes as a function of concentration: a) relative intensity of the contact ion paired nitrate as a function of molality; b) sum intensity of the free and ion paired nitrate as a function of molarity.

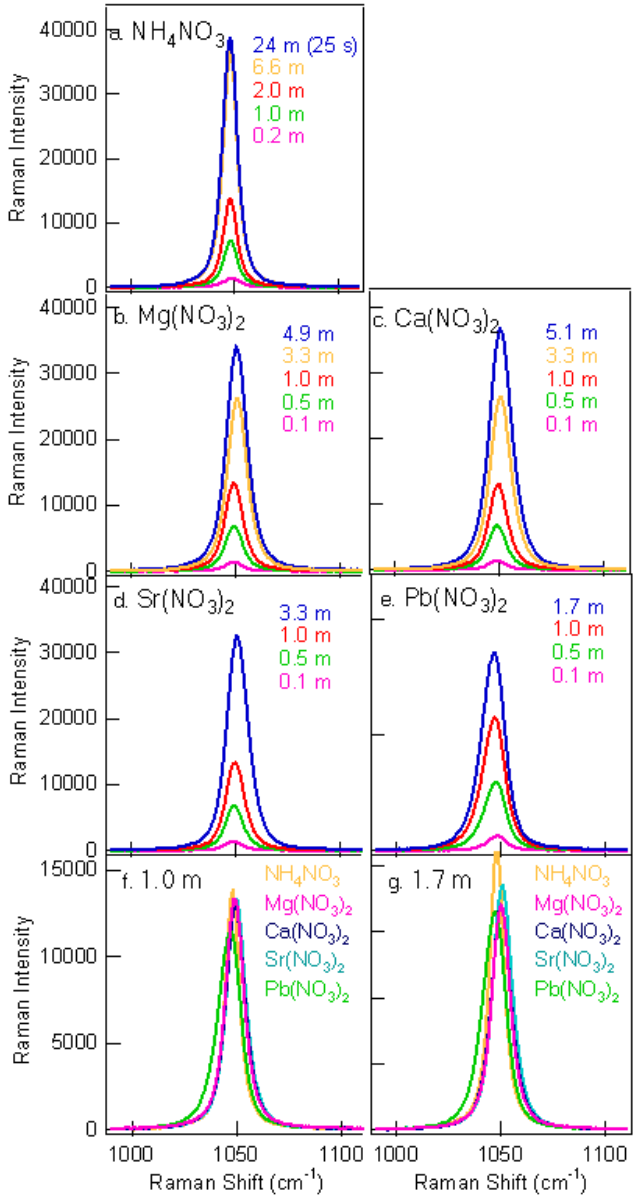

Figure 4.5 Raman spectra of nitrate symmetric stretching modes: a) NH_4NO_3 solutions; b) $Mg(NO_3)_2$ solutions; c) $Ca(NO_3)_2$ solutions; d) $Sr(NO_3)_2$ solutions; e) $Pb(NO_3)_2$ solutions; f) 1.0 m solutions; g) 1.7 m solutions. In panel a), exposure time 25 s instead of 50 s was used for 24 m NH_4NO_3 because of the saturation issue. In panel f) and g), NH_4NO_3 has the same nitrate concentrations with dication nitrate solutions, i.e. 2.0 m and 3.4 m respectively.

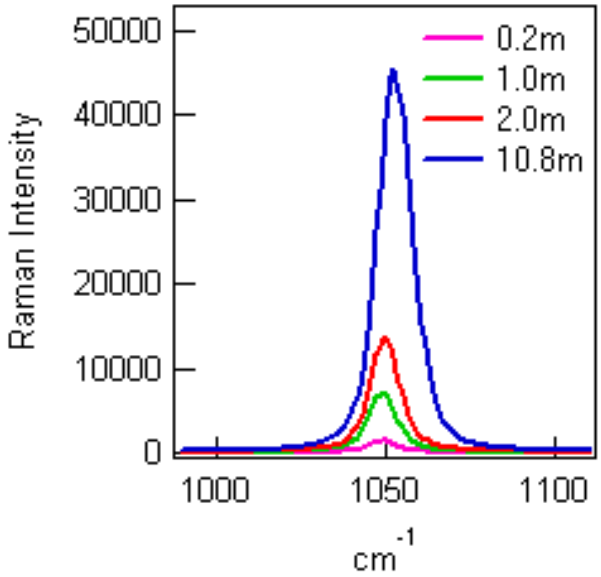

Figure 4.6 Nitrate symmetric stretching peaks in Raman spectra of $NaNO_3$ solutions.

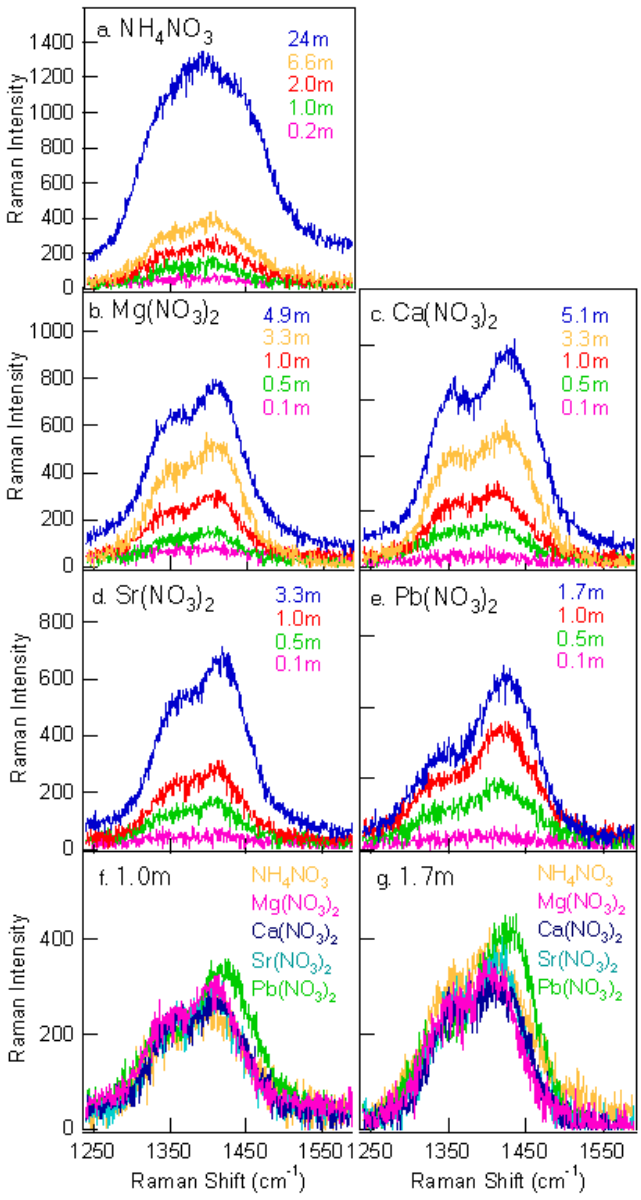

Figure 4.7 Raman spectra of nitrate asymmetric stretching modes: a) NH_4NO_3 solutions; b) $Mg(NO_3)_2$ solutions; c) $Ca(NO_3)_2$ solutions; d) $Sr(NO_3)_2$ solutions; e) $Pb(NO_3)_2$ solutions; f) 1.0m solutions; g) 1.7m solutions. In panel f) and g), NH_4NO_3 has the same nitrate concentrations with dication nitrate solutions, i.e. 2.0 m and 3.4 m respectively.

Molality (moles per kg of water)	Salt Mole Fraction (m.f.)	Molarity (moles per liter)			
		$Mg(NO_3)_2$	$Ca(NO_3)_2$	$Sr(NO_3)_2$	$Pb(NO_3)_2$
0.10	0.0018	0.089	0.092	0.10	0.10
0.50	0.0089	0.47	0.46	0.49	0.49
1.0	0.018	0.88	0.90	0.96	0.94
1.7	0.030	1.3	1.4	1.6	1.6
2.6	0.045	1.9	2.0	2.3	-
3.3	0.056	2.2	2.3	2.7	-
4.9	0.081	2.8	-	-	-
5.1	0.084	-	3.2	-	-

Table 4.1 Concentrations of the nitrate aqueous solutions.

	0.5 m		1 m				1.7 m			
	Position	Area	Position (cm^{-1})		Area		Position (cm^{-1})		Area	
			#1	#2	#1	#2	#1	#2	#1	#2
NH_4NO_3[1]	718.0	6662	718.1	-	12623	-	718.2	-	21496	-
$Mg(NO_3)_2$	719.0	8007	718.8	-	16535	-	719.9	-	21943	-
$Ca(NO_3)_2$	719.0	10188	718.6	738.2	16241	3276	718.6	738.4	19972	5139
$Sr(NO_3)_2$	720.4	9429	717.8	732.3	14850	3926	717.9	733.5	19132	8478
$Pb(NO_3)_2$	721.1	6168	716.6	727.8	10327	6634	716.7	729.3	12673	10169

	3.3 m				Saturated			
	Position (cm^{-1})		Area		Position (cm^{-1})		Area	
	#1	#2	#1	#2	#1	#2	#1	#2
NH_4NO_3[1]	718.3	-	39324	-	718.2	-	88443	-
$Mg(NO_3)_2$	720.4	-	37953	-	720.1	-	48296	-
$Ca(NO_3)_2$	719.1	739.5	32589	10262	718.5	739.7	41380	23187
$Sr(NO_3)_2$	718.4	734.9	33914	19443	718.4	734.9	33914	19443
$Pb(NO_3)_2$	-	-	-	-	716.7	729.3	12673	10169

Table 4.2 Curve-fitting results of nitrate in-plane deformation bands in Raman spectra.

[1] NH_4NO_3 has the same nitrate concentration as the divalent cation-nitrate solutions. The concentrations for NH_4NO_3 solutions are 1 m, 2 m, 3.4 m, 6.6 m and saturated.

	0.5 m		1.0 m		1.7 m	
	Position (cm^{-1})	FWHM (cm^{-1})	Position (cm^{-1})	FWHM (cm^{-1})	Position (cm^{-1})	FWHM (cm^{-1})
NH_4NO_3[2]	1047.9	7.9	1047.8	7.9	1047.8	8.0
$Mg(NO_3)_2$	1048.9	9.9	1048.9	10.3	1049.9	10.5
$Ca(NO_3)_2$	1048.7	10.2	1049.1	10.6	1049.9	11.0
$Sr(NO_3)_2$	1049.0	10.1	1049.5	10.7	1050.5	11.1
$Pb(NO_3)_2$	1046.9	12.2	1046.3	12.8	1046.1	13.0
	3.3 m		Saturated			
	Position (cm^{-1})	FWHM (cm^{-1})	Position (cm^{-1})	FWHM (cm^{-1})		
NH_4NO_3[2]	1047.8	8.1	1047.6	8.5		
$Mg(NO_3)_2$	1050.5	11.1	1050.2	11.8		
$Ca(NO_3)_2$	1050.4	11.8	1050.3	12.8		
$Sr(NO_3)_2$	1050.6	12.1	1050.6	12.1		
$Pb(NO_3)_2$	-	-	1046.1	13.0		

Table 4.3 Curve-fitting results of nitrate symmetric stretching bands in Raman spectra.

[2] NH_4NO_3 has the same nitrate concentration as the divalent cation-nitrate solutions. The concentrations for NH_4NO_3 solutions are 1 m, 2 m, 3.4 m, 6.6 m and saturated.

	0.5 m Position (cm^{-1})	1.0 m Position (cm^{-1})	Saturated Position (cm^{-1})
$Mg(NO_3)_2$	1043.6	1043.9	1045.2
$Ca(NO_3)_2$	1042.8	1043.3	1044.7
$Sr(NO_3)_2$	1043.8	1043.5	1045.5
$Pb(NO_3)_2$	1039.2	1038.6	1038.4

Table 4.4 Curve-fitting results of nitrate symmetric stretching bands in IR spectra.

	0.5 m			1.0 m			1.7 m		
	Position (cm^{-1})		Separation	Position (cm^{-1})		Separation	Position (cm^{-1})		Separation
	#1	#2		#1	#2		#1	#2	
NH_4NO_3[3]	1343.4	1406.7	63.3	1336.5	1405.6	69.1	1337.3	1406.3	69.0
$Mg(NO_3)_2$	1344.7	1407.9	63.2	1344.5	1410.7	66.2	1342.3	1409.1	66.8
$Ca(NO_3)_2$	1350.8	1415.2	64.4	1347.4	1415.1	67.7	1348.0	1418.9	70.9
$Sr(NO_3)_2$	1347.3	1412.2	64.9	1350.8	1415.3	64.5	1353.0	1418.1	65.1
$Pb(NO_3)_2$	1335.4	1418.3	82.9	1335.8	1423.3	87.5	1336.3	1426.7	90.4
	3.3 m			Saturated					
	Position (cm^{-1})		Separation	Position (cm^{-1})		Separation			
	#1	#2		#1	#2				
NH_4NO_3[3]	1333.8	1403.5	69.7	1335.9	1406.2	70.3			
$Mg(NO_3)_2$	1344.3	1412.0	67.7	1344.1	1412.6	68.5			
$Ca(NO_3)_2$	1349.2	1426.0	76.8	1349.6	1430.9	81.3			
$Sr(NO_3)_2$	1354.4	1421.5	67.1	1354.4	1421.5	67.1			
$Pb(NO_3)_2$	-	-	-	1336.3	1426.7	90.4			

Table 4.5 Curve-fitting analysis of nitrate asymmetric stretching bands in Raman spectra.

[3] NH_4NO_3 has the same nitrate concentration as the divalent cation-nitrate solutions. The concentrations for NH_4NO_3 solutions are 1 m, 2 m, 3.4 m, 6.6 m and saturated.

CHAPTER 5

NITRATE IONS AND ION PAIRING AT THE AIR-AQUEOUS INTERFACE

The nature of nitrate ions at the air-aqueous interface has received special attention recently because of the growing awareness of their key role in the surface chemistry of atmospheric aerosols and aqueous systems.[6,10,19,21] Nitrate ions are ubiquitous in aqueous-phase atmospheric aerosols from the polluted to the remote troposphere, and are involved in a variety of atmospheric heterogeneous reactions.[1,4-6,9,10] Meanwhile, nitrate plays an important role in aqueous geochemistry, and has potential toxicities to humans and other animals. Thus, a fundamental understanding of nitrate at air-aqueous interfaces may provide insight into the role of nitrate ions at the surface of water systems and aqueous-phase atmospheric aerosols.

In the work reported here, for the first time, a vibrational mode of the nitrate ion at the air-aqueous interface is directly probed by an interface specific technique, vibrational sum frequency generation spectroscopy. Kido Soule et al.[73] have studied nitric acid in a different spectral region. Other previous VSFG studies of nitrate aqueous solutions mainly focused on the influence of ions on the interfacial water structure.[74] Our VSFG study directly probes nitrate at the interface and reveals that the interfacial nitrate anion follows bulk ion pairing trends with Mg^{2+}–nitrate ion pairing weaker than Ca^{2+}–nitrate

and Sr^{2+}–nitrate ion pairing.[72] Ion pairing refers to the interaction and association of oppositely charged ions,[42,75] where the long-range electrostatic Coulombic forces play a major role.[42] $Mg(NO_3)_2$ is particularly interesting at the air-aqueous interface. We observed two distinct nitrate populations for aqueous $Mg(NO_3)_2$ solution interfaces, where the population defines the extent of ion-ion interaction. The amount of relatively free nitrate ions (negligible ion-ion interaction) at the air-aqueous interface becomes significant at lower bulk concentration of $Mg(NO_3)_2$. This phenomenon is not observed in the bulk. It appears that the number of water molecules available to solvate the nitrate ion plays a pivotal role for ion pairing, or lack of it, at the air-aqueous interface.

5.1 Materials

Nitrate salts, $Mg(NO_3)_2$, $Ca(NO_3)_2$, and $Sr(NO_3)_2$, were purchased from Fisher Scientific. Nanopure water with resistivity 18.0-18.3 MΩ cm was used to make the aqueous solutions. To remove organic impurities, aqueous solutions were filtered three to six times by using a carbon filter (Whatman Carbon-Cap 150). VSFG spectra in the 2800 cm^{-1} to 3000 cm^{-1} region were obtained to check for organic impurities in these nitrate aqueous solutions.

Solutions of concentrations 2.6 m and 3.3 m were studied in this work. According to densities of nitrate solutions at room temperature (297 K), 2.6 m corresponds to 0.045 m.f. (salt mole fraction) for all salts, and 1.9 M (mol/L) for $Mg(NO_3)_2$, 2.0 M for $Ca(NO_3)_2$,

and 2.3 M for $Sr(NO_3)_2$; 3.3 m corresponds to 0.056 m.f. for all salts, and 2.2 M for $Mg(NO_3)_2$, 2.3 M for $Ca(NO_3)_2$, and 2.7 M for $Sr(NO_3)_2$ (see Table 4.1).

5.2 Experimental Method

The VSFG spectra presented in this chapter were acquired using the 20 Hz scanning VSFG system (EKSPLA). The polarizations were ssp for the sum frequency, visible and infrared pulses, respectively. The VSFG spectra were acquired using a 30 s exposure time for each data point and were normalized to the real-time IR profile. All VSFG spectra shown in this chapter are an average of four to six replicate spectra.

Complementary to the VSFG study that provides interfacial information, the Raman and IR spectra of the nitrate bulk solutions were obtained. In the Raman instrumentation, a 785 nm light from a continuous wave laser (Raman System Inc.) was used for sample illumination. The power of the 785 nm light was ~240 mW. The slit width of the monochromator entrance slit was 50 μm, the grating used was 600 grooves/mm, and the resolution was 3.2 cm^{-1}. Raman spectra were collected with an exposure time of 50 s. In the IR experiments, a 45° single-bounce ZnSe crystal trough was employed to collect the IR spectra. Additional details of VSFG, Raman and IR instrumentation are in Chapter 3.

In the curve-fitting analysis, the VSFG spectra were fit with the peak-fitting function in IgorPro 4.05A software (WaveMetrics, Inc.) using a home-written program to incorporate phase.[41] The mathematical model describing the profile of bands was the

Lorentzian model. Detailed information of VSFG curve-fitting analysis is shown in Chapter 3. In the fit of nitrate VSFG spectra, standard deviations of the experimental data were considered and included as the weighting factor.

5.3 Results and Discussion

Figure 5.1 shows the ssp-polarized VSFG spectra of $Mg(NO_3)_2$ aqueous solutions at the air-aqueous interface. In the spectrum of the 2.6 m $Mg(NO_3)_2$ aqueous solution (Figure 5.1a), a peak at 1063 cm^{-1} and a shoulder at 1047 cm^{-1} are observed, whereas in the spectrum of the 3.3 m $Mg(NO_3)_2$ solution (Figure 5.1b) the dominant peak position is at 1047 cm^{-1}. To assign the observed VSFG peaks, Raman and IR spectra were obtained from the $Mg(NO_3)_2$ aqueous solutions, as shown in Figure 5.2. The peaks at 1050 cm^{-1} in the Raman spectra (Figure 5.2a) and 1044 cm^{-1} in the IR spectra (Figure 5.2b) are assigned to the symmetric stretch modes of nitrate. For free nitrate with a D_{3h} symmetry, the symmetric stretch band is IR inactive.[51,58] The symmetric stretch however occurs in the IR spectra (Figure 5.2b) as a result of the perturbation of cations and/or water molecules that lowers the symmetry of nitrate.[51,58,59] The noncoincidence between Raman and IR frequencies may arise from the strong intermolecular resonant vibrational coupling that leads to rapid transfer of vibrational excitations in the time domain and delocalization of vibrational modes in the frequency domain.[76,77] Therefore, the peaks around 1047 cm^{-1} and 1063 cm^{-1} in the VSFG spectra of $Mg(NO_3)_2$ (Figure 5.1) are

assigned to the symmetric stretch modes of nitrate anions at the air-aqueous interface.

In Figure 5.1a and b the dominant VSFG peak position of the nitrate symmetric stretch has changed from 1063 cm^{-1} to 1047 cm^{-1} as the bulk concentration of $Mg(NO_3)_2$ increases from 2.6 m to 3.3 m. Unlike VSFG spectra that provide vibrational information at the interface, Raman and IR spectra shown in Figure 5.2 provide bulk information. Raman spectra (Figure 5.2a) show only a slight frequency shift of the nitrate symmetric stretch band from 1049 cm^{-1} to 1050 cm^{-1} when $Mg(NO_3)_2$ concentration increases from 2.6 m to 3.3 m. In the IR spectra (Figure 5.2b), a similar frequency shift (from 1044 cm^{-1} to 1045 cm^{-1}) is observed. When the concentration of $Mg(NO_3)_2$ varies in a much broader range (0.5 m to saturated), the frequency shift is less than 2 cm^{-1} (see Figure 4.5b and Table 4.3 in the previous chapter). Note in both Raman and IR spectra the symmetric stretch peak shifts 1-2 cm^{-1} to higher frequency with increasing concentration. This blue shift has been interpreted by the weakening of the nitrate-water hydrogen-bonding.[65,72] In the VSFG spectra, there are two resolvable component peaks that are 16 cm^{-1} apart, where the 1063 cm^{-1} peak and the 1047 cm^{-1} peak are dominant for the 2.6 m and 3.3 m $Mg(NO_3)_2$ solutions, respectively. The VSFG shift in frequency for the dominant peak is opposite to what is observed in the bulk studies. Therefore, the 16 cm^{-1} frequency change of the nitrate symmetric stretch band in the VSFG spectra cannot be simply explained by a bulk-like ion pairing trend. Only the 3.3 m symmetric stretch frequency is similar to the observed bulk symmetric stretch frequencies, whereas the 2.6 m symmetric stretch

frequency has never before been observed for either interfacial or bulk aqueous $Mg(NO_3)_2$. Clearly, at the lower 2.6 m solution air-aqueous interface, unique behavior is observed. Deconvolution of the symmetric stretch peak further confirms a two-component band, consisting of two populations.

At the air-aqueous interface, the two populations associated with the component bands at 1047 cm^{-1} and 1063 cm^{-1} are ion-paired and relatively free nitrate, respectively. Nitrate anions located in the air-aqueous interfacial region attract Mg^{2+} cations toward the interface. This interface-driving electroneutrality force competes with the bulk-driving electrostatic force.[20,78] According to previous theoretical and experimental studies, $Mg(NO_3)_2$ aqueous solutions are well-behaved, close-to-ideal solutions with extensive ion-water mixing and virtually no formation of contact ion pairs between Mg^{2+} and nitrate.[20,59,72] At the air-aqueous interface, nitrate anions exhibit only a very weak propensity for the interface, as suggested by previous MD simulations.[20,21,78] The VSFG data presented here reveal that the electroneutrality effect of nitrate within the interface on Mg^{2+} is relatively weak, and the electrostatic repulsion of Mg^{2+} from the interface dominates. It is well accepted that small "hard" Mg^{2+} ions are strongly repelled from the air-aqueous interface, in accord with classical theory of electrolyte surfaces.[20,79] In the 2.6 m $Mg(NO_3)_2$ aqueous solution, Mg^{2+} cations reside preferentially deep in the bulk. The Coulombic interaction and the ion pairing between Mg^{2+} and interfacial nitrate is relatively weak, as just discussed. A lack (or significant weakening) of interaction would

reasonably shift the nitrate symmetric stretch to higher frequency compared with the nitrate ions where the interaction is stronger at the air-aqueous interface of the 3.3 m $Mg(NO_3)_2$ solution. Recently, Thomas et al.[21] found that for nitrate anions that approach the air-aqueous interface there is a decrease in the number of water molecules coordinating to the interfacial nitrate relative to the bulk nitrate. The low coordination number could shift the nitrate symmetric stretch peak to higher frequency compared to the bulk. However, this would also be expected to occur for the 3.3 m $Mg(NO_3)_2$ solution, but is not observed in the VSFG spectrum (Figure 5.1b). In fact, the 1047 cm^{-1} peak position that dominates the 3.3 m solution is close to which is observed in bulk studies. Therefore, we conclude that the electrostatic repulsion of Mg^{2+} from the interface is the dominant effect that results in a weak Columbic interaction between Mg^{2+} and interfacial nitrate for 2.6 m $Mg(NO_3)_2$ solution. Hence, at the air-aqueous interface, the VSFG frequency at 1063 cm^{-1} is assigned to the symmetric stretch of relatively free interfacial nitrate species, and the component peak at 1047 cm^{-1} is assigned to the symmetric stretch of ion-paired interfacial nitrate, likely a SSIP or SSHIP.

The 1063 cm^{-1} peak has not been observed from Raman or IR $Mg(NO_3)_2$ ion pairing studies. The assignment of this peak frequency to a relatively free nitrate anion allows us to further shed light on bulk studies. Although Mg^{2+} has been considered to be ineffective at ion pairing with nitrate from previous bulk studies,[57,59] it is not. This is clearly demonstrated by the present work, which reveals that ion pairing dominates at the air-

aqueous interface of the 3.3 m $Mg(NO_3)_2$ solution, and provides additional reference frequencies for perturbed nitrate. Therefore, ion-ion interactions are stronger than previously thought in the bulk $Mg(NO_3)_2$ aqueous solutions.

To better understand the VSFG spectra of 2.6 m and 3.3 m $Mg(NO_3)_2$ solutions, curve-fitting analysis was completed for nitrate symmetric stretch modes. Component peaks at 1047 cm^{-1} and 1063 cm^{-1} were employed in the curve-fitting analysis. Curve-fitting results are presented in Table 5.1 and component peaks are shown in red dashed lines in figures. In the VSFG spectrum of 2.6 m $Mg(NO_3)_2$, the component peak at 1063 cm^{-1} is the dominant peak, and the area ratio of the peak at 1047 cm^{-1} to the peak at 1063 cm^{-1} is 0.12. Recall that VSFG intensity is related to orientation and is proportional to the square of the interfacial number density. Assuming that the interfacial nitrate orientation relative to the surface normal remains constant for relatively free and ion-paired nitrate,[21] the surface number density ratio of ion-paired to relatively free nitrate ($SDR_{IP/free}$) is therefore 0.34. In other words, the majority of interfacial nitrate ions are relatively free at the air-aqueous interface of a 2.6 m $Mg(NO_3)_2$ aqueous solution.

As the concentration of the $Mg(NO_3)_2$ solution increases, the Coulombic interaction as well as the ion pairing between Mg^{2+} cations and interfacial nitrate anions becomes stronger and the number of water molecules available for ion solvation decreases. Note that the 2.6 m (0.045 m.f.) solution has approximately one more water molecule per ion relative to the 3.3 m (0.056 m.f.) solution, that is, at 2.6 m there are seven water

molecules per ion (cation or anion), and at 3.3 m there are six water molecules per ion. At concentration 3.3 m, more Mg^{2+} cations are forced to approach the air-aqueous interface relative to the 2.6 m solution. The interfacial nitrate is therefore more ion-paired for the 3.3 m $Mg(NO_3)_2$ solution. According to our curve-fitting results and obvious from the spectrum (Figure 5.1b, Table 5.1), the $SDR_{IP/free}$ is 1.7 at the air-aqueous interface of 3.3 m $Mg(NO_3)_2$. The ion-paired nitrate, SSIP or SSHIP, becomes the dominant interfacial species at the air-aqueous interface of the 3.3 m $Mg(NO_3)_2$ solution.

Interestingly, the total peak intensity of the 3.3 m $Mg(NO_3)_2$ aqueous solution is not higher than that of the 2.6 m $Mg(NO_3)_2$ solution as one might expect. Recall that the VSFG intensity depends on the square of the number density of interfacial molecules, their orientation, and the Raman and IR transition strengths of the vibrational mode.[22-25] As indicated in the Raman and IR intensities shown in Figure 5.3, there is no significant change in transition moment strengths for the low frequency peak with concentration. However, the 1063 cm^{-1} component peak has not been observed in bulk systems. An argument can be made for a change in interfacial number densities of nitrate ions if one assumes negligible orientation changes. Based on previous computational studies,[21] the interfacial nitrate ions are preferentially oriented with the plane of nitrate parallel to the interface. The assumption of negligible orientation changes of interfacial nitrate is thus reasonable. Therefore, the VSFG data suggests a larger number density of interfacial nitrate ions for the lower concentration $Mg(NO_3)_2$ solution, 2.6 m.

The VSFG spectra of $Ca(NO_3)_2$ and $Sr(NO_3)_2$ solutions at the air-aqueous interface are somewhat different relative to the $Mg(NO_3)_2$ solutions. The VSFG spectra of $Ca(NO_3)_2$ and $Sr(NO_3)_2$ with concentrations 2.6 m and 3.3 m are shown in Figure 5.4. According to these spectra and curve-fitting results (Table 5.1), the dominant symmetric stretch peak of nitrate is at 1047 cm^{-1} rather than 1063 cm^{-1}, and the $SDR_{IP/free}$ varies from 2.4 to 4.5, indicating that the dominant interfacial nitrate species are ion-paired rather than free for $Ca(NO_3)_2$ and $Sr(NO_3)_2$ solutions. If we compare $Mg(NO_3)_2$, $Ca(NO_3)_2$, and $Sr(NO_3)_2$ with the same concentration, 3.3 m, the VSFG results show that the $SDR_{IP/free}$ is 1.7 for $Mg(NO_3)_2$, 2.8 for $Ca(NO_3)_2$, and 4.5 for $Sr(NO_3)_2$. At the air-aqueous interface, the strong Coulombic cation-nitrate interaction results in more ion-paired nitrate for $Sr(NO_3)_2$ and $Ca(NO_3)_2$ solutions compared to $Mg(NO_3)_2$ solution of the same concentration. The trend of the Coulombic interaction with nitrate, $Sr^{2+} > Ca^{2+} > Mg^{2+}$, is similar to previous bulk ion pairing studies,[51,57,72] where Ca^{2+} and Sr^{2+} have been found to have a stronger tendency to form ion pairs with NO_3^- in aqueous solutions, with Sr^{2+}–nitrate ion pairing slightly stronger than Ca^{2+}–nitrate ion pairing.

5.4 Conclusions

The air-aqueous interface of divalent metal-nitrate solutions was investigated using vibrational sum frequency generation spectroscopy. Sum frequency results reveal a lack of ion-ion interaction, and thus, lack of ion-pairing at the air-aqueous interface for a 2.6

m (0.045 m.f.) aqueous solution of $Mg(NO_3)_2$. Results also suggest that full solvation, or lack of it, at the air-aqueous interface of $Mg(NO_3)_2$ solutions has significant implications for ion pairing between interfacial nitrate and the small, densely charged Mg^{2+} cation. The interface appears to be highly sensitive, particularly when full solvation of the interfacial anion is compromised. The fact that relatively free nitrate anions exist at the air-aqueous interface is surprising.

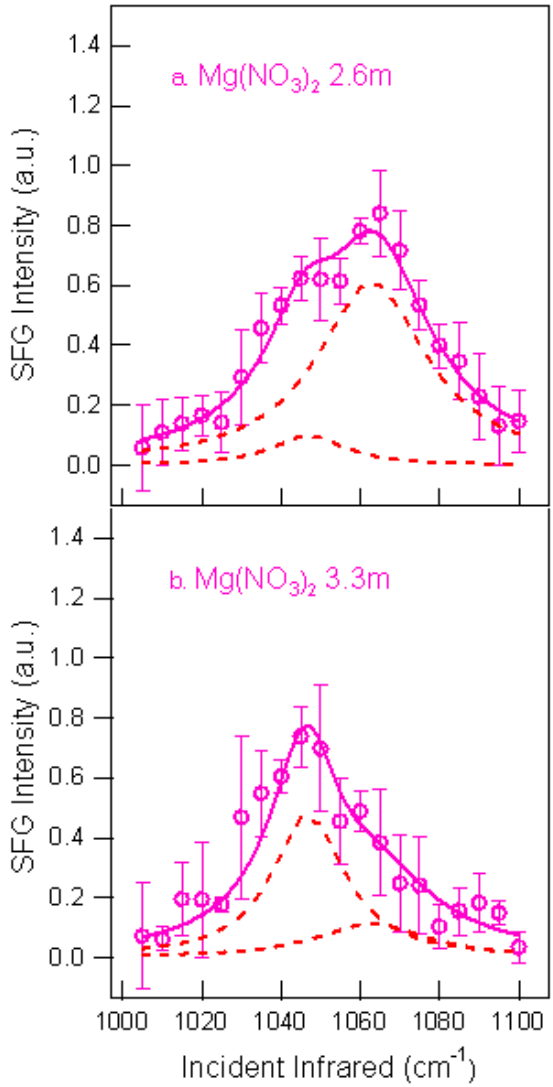

Figure 5.1 VSFG spectra of aqueous $Mg(NO_3)_2$ solutions with ssp polarization: a) 2.6 m $Mg(NO_3)_2$; b) 3.3 m $Mg(NO_3)_2$. Pink circles: experimental data with error bars; pink solid lines: overall fits; red dashed lines: Lorentzian component peaks.

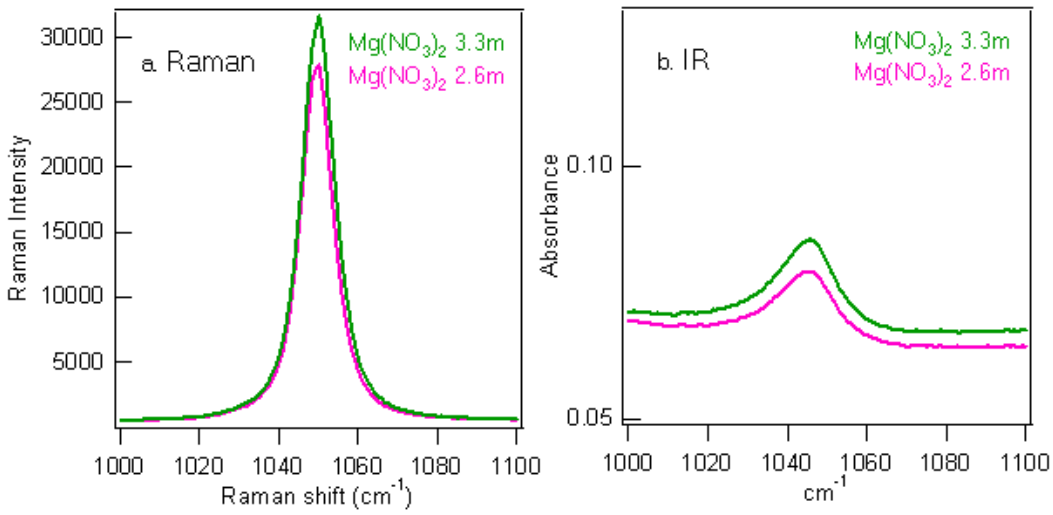

Figure 5.2 Raman and IR spectra of aqueous $Mg(NO_3)_2$ solutions with concentration 2.6 m and 3.3 m: a) Raman spectra; b) IR spectra. Coloring scheme: 2.6 m $Mg(NO_3)_2$, pink; 3.3 m $Mg(NO_3)_2$, green.

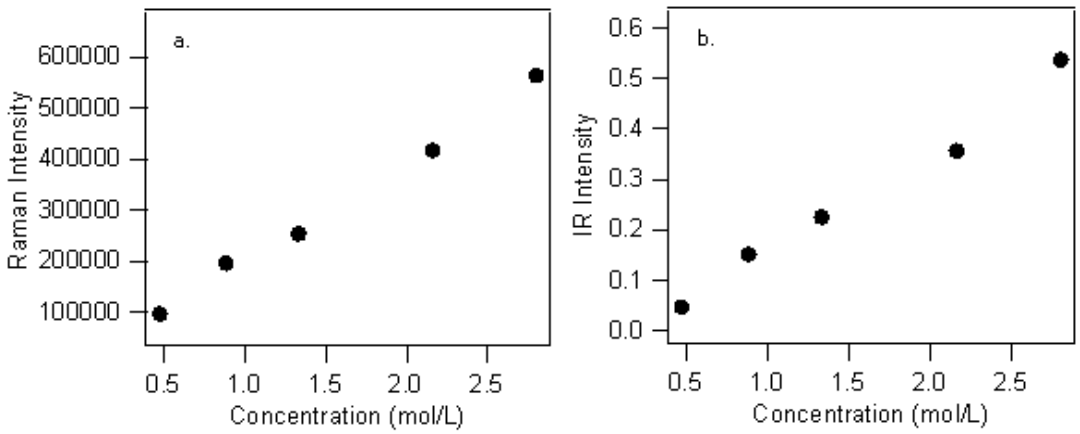

Figure 5.3 Raman (a) and IR (b) intensities of nitrate symmetric stretch peak as a function of concentration.

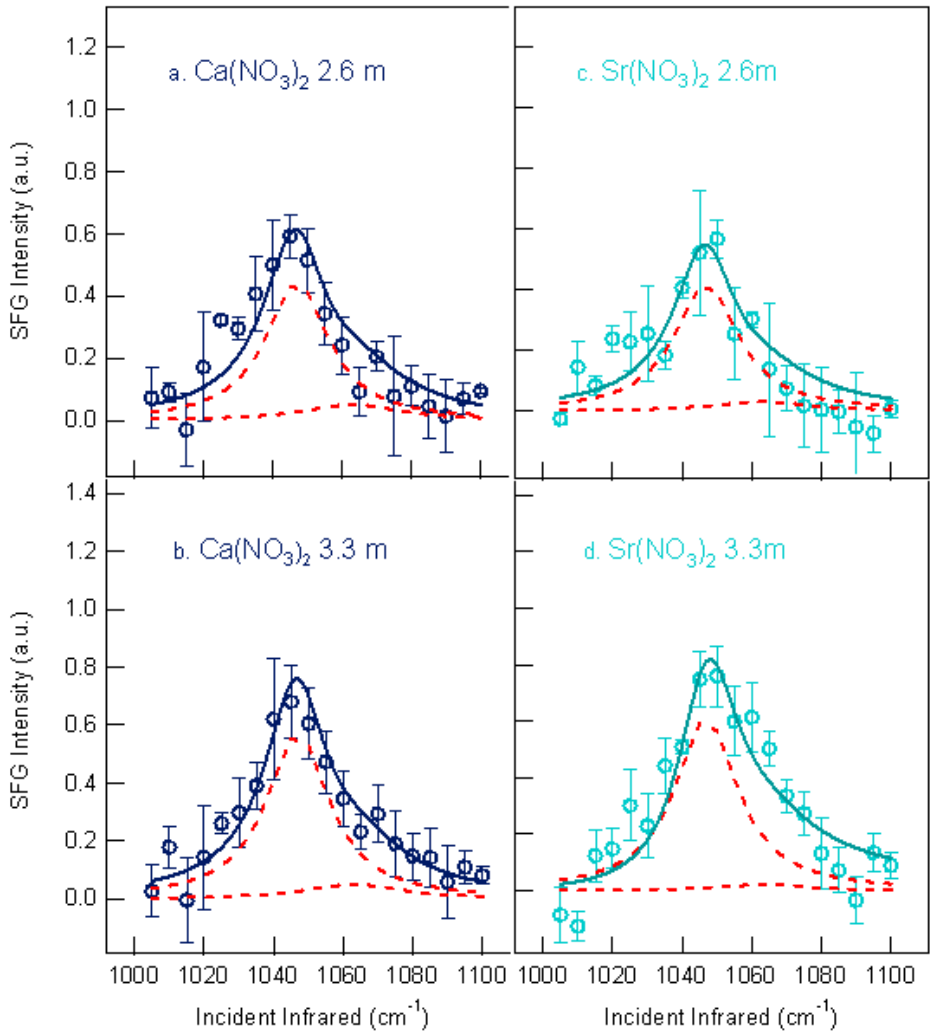

Figure 5.4 VSFG spectra of aqueous $Ca(NO_3)_2$ and $Sr(NO_3)_2$ solutions with ssp polarization: a) 2.6 m $Ca(NO_3)_2$; b) 3.3 m $Ca(NO_3)_2$; c) 2.6 m $Sr(NO_3)_2$; d) 3.3 m $Sr(NO_3)_2$. Blue circles: experimental data with error bars; solid lines: overall fits; red dashed lines: Lorentzian component peaks.

	Molality (m)	Non-resonant terms		I_{1047}	$hwhm_{1047}$	I_{1063}	$hwhm_{1063}$	I_{1047}/I_{1063}	$SDR_{IP/free}$
		Real	Imaginary						
$Mg(NO_3)_2$	2.6	0.002	0.01	2.9	10.9	25.0	16.8	0.12	0.34
	3.3	0.002	0.01	14.1	10.9	4.7	16.8	3.0	1.7
$Ca(NO_3)_2$	2.6	0.002	0.01	13.0	10.9	2.2	16.8	5.9	2.4
	3.3	0.002	0.01	16.8	10.9	2.1	16.8	8.0	2.8
$Sr(NO_3)_2$	2.6	0.002	0.01	12.5	10.9	1.3	16.8	9.6	3.1
	3.3	0.002	0.01	18.3	10.9	0.91	16.8	20	4.5

Table 5.1 Curve-fitting results of nitrate VSFG spectra. Surface number density ratio of ion-paired to relatively free nitrate ($SDR_{IP/free}$) is shown.

CHAPTER 6

WATER STRUCTURE AT THE AIR-AQUEOUS NITRATE INTERFACE

The ubiquitous nature of water in the environment and biological systems makes understanding water structure at aqueous interfaces of great interest and importance in atmospheric chemistry, aqueous geochemistry, and biology. The traditional view of the interface of inorganic salt solutions is that it is devoid of ions,[80,81] which is based primarily on macroscopic surface tension data and the Gibbs adsorption equation. However, this traditional picture has recently been challenged by theoretical[78,82-86] and experimental[38,85-89] studies. Large, polarizable ions, such as I^-, Br^-, SCN^-, and N_3^-, have been suggested to exhibit a propensity for the air-aqueous interface by molecular dynamics simulations and interface sensitive experimental observations. The inconsistency with the traditional picture originates from the fact that surface tension data provide only an integrated value of the ionic deficit over the whole interfacial region, whereas in the interfacial region the ion distribution could be nonmonotonic with ion concentrations varying with depth.

Vibrational sum frequency generation spectroscopy, an interface specific technique that provides molecular-level spectroscopic information, is among the most powerful techniques for investigating the interfacial structure of liquids and solids.[22,23,25,31,38,90,91]

The work in Chapter 5 directly probed nitrate ions and metal-nitrate ion pairing at the aqueous interface. The presence of these ions and the formation of ion pairs may have considerable effects on the hydrogen-bonded structure of water at the air-aqueous interface. Therefore, the aim of the work presented in this chapter is to elucidate the perturbation of nitrate anions, metal cations, and ion pairs on water structure at the air-aqueous interface by investigating water OH stretching modes. The sum frequency spectral changes indicate different effects of cations, Mg^{2+}, Ca^{2+}, and Sr^{2+}, on the interfacial water hydrogen-bonding network. A thickening of the air-aqueous interface with increasing cation size is proposed.

6.1 Materials

All nitrate salts were purchased from Fisher Scientific. The aqueous solutions were made using Nanopure water with resistivity 18.0-18.3 MΩ cm, and filtered, typically three to six times, using a carbon filter (Whatman Carbon-Cap 150) to remove organic impurities. VSFG spectra in the 2800 cm^{-1} to 3000 cm^{-1} region were obtained to check for organic impurities in the salt solutions. Aqueous solutions of 2.6 m and 3.3 m were studied in the present work. 2.6 m corresponds to 0.045 m.f., and 3.3 m corresponds to 0.056 m.f. for all salts (see Table 4.1).

6.2 Experimental Method

The VSFG spectra presented in this chapter were acquired using the 10 Hz scanning VSFG system. The polarizations were ssp for the sum frequency, visible and infrared light pulses, respectively. The ssp-polarized VSFG spectra presented in this chapter are the average of three replicate spectra with a 15 s exposure time for each data point, normalized to the real-time IR profile. A VSFG spectrum of neat water was obtained at the beginning and at the end of each experiment.

In addition to the VSFG study that provides information of the interfacial region, Raman and infrared experiments that provide bulk information were conducted. In the Raman instrumentation, 532 nm photons from a continuous wave laser (Spectra-Physics, Millennia II) were used for sample illumination. The power at 532 nm was ~100 mW. The grating used was 600 grooves/mm, the slit width of the monochromator entrance slit was 50 μm, and the spectral resolution was 3.2 cm^{-1}. Raman spectra presented in this chapter were collected with an exposure time of 50 s. Additional details of VSFG, Raman and IR instrumentation are in Chapter 3.

6.3 Results and Discussion

The VSFG spectrum of the air–neat water interface and the Raman and IR spectra of bulk water in the OH stretching region (3000-3800 cm^{-1}) are shown in Figure 6.1. The broad continuum spanning from ~3000 cm^{-1} to ~3600 cm^{-1} of the VSFG (Figure 6.1a),

Raman (Figure 6.1b) and IR (Figure 6.1c) spectra is assigned to the OH stretching modes of hydrogen-bonded water molecules. Though the precise assignment of the 3000-3600 cm^{-1} continuum remains controversial,[31,90-92] it is safe to say that there is a unique relationship between the frequency of the OH stretch and the length and strength of the hydrogen-bonds.[93] The lower frequencies beginning at ~3000 cm^{-1} arise from the OH stretching modes of strongly hydrogen-bonded water molecules within the hydrogen-bonding network. The observed resonances at higher frequencies arise from less strongly hydrogen-bonded water molecules. Not part of the continuum in the VSFG spectrum shown in Figure 6.1a is a narrow peak at 3700 cm^{-1}, which is assigned to the dangling OH (free OH) stretch of water molecules that straddle the air-water interface with one uncoupled OH bond directed into the gas phase and the other interacting through hydrogen-bonding with the liquid phase.

To understand the hydrogen-bonding network of the bulk water after addition of nitrate salts, a series of Raman and IR spectra were acquired for 2.6 m and 3.3 m $Mg(NO_3)_2$, $Ca(NO_3)_2$, and $Sr(NO_3)_2$ aqueous solutions. The Raman spectra of these solutions are shown in Figure 6.2a-b, and the IR spectra are shown in Figure 6.2c-d. With the addition of nitrate salts to water, the Raman spectra clearly reveal a decrease in the low frequency side (~3200 cm^{-1}) of the hydrogen-bonded continuum, and a substantial intensity increase in the high frequency side (~3400 cm^{-1}) of the continuum. The low frequency side and the high frequency side of the OH stretch in the hydrogen-bonding

network will be called the 3200 cm^{-1} band and the 3400 cm^{-1} band in this chapter for ease of comparison. The IR spectra (Figure 6.2c-d) show a decrease and narrowing of the 3200 cm^{-1} band and no enhancement of the 3400 cm^{-1} band. The changes in the Raman and IR spectra of the hydrogen-bonded OH stretch upon the addition of nitrate salts relative to that of neat water is attributed to the water hydrogen-bonding network distortion and the solvation of ions. Due to the presence of metal cations and nitrate anions in aqueous solutions, the displacement of water molecules by these ions would perturb the strong hydrogen-bonding network, resulting in an intensity loss of the 3200 cm^{-1} band in the Raman and IR spectra. Meanwhile, the water molecules that solvate the ions give rise to an intensity enhancement of the 3400 cm^{-1} band in the Raman spectra. The difference in the Raman and IR spectra is associated with different selection rules.[38]

Unlike previous studies of sodium halides and hydrogen halides where the Raman intensity enhancement of the 3400 cm^{-1} band has been found to be associated with the size and the polarizability of the anion ($Cl^- < Br^- < I^-$),[38,87] the intensity of the 3400 cm^{-1} band in the Raman spectra (Figure 6.2a-b) remains constant when the size and the polarizability of the metal cation changes in the nitrate solutions. The calculated polarizability values of cations and anions are listed in Table 6.1. Br^- has a polarizability approximately twice as high as that of Cl^-, and the Raman intensity of the 3400 cm^{-1} band of NaBr, for example, is higher than that of NaCl.[38] The difference is significant especially in more concentrated solutions (0.036 m.f., which equals 2.1 m).[38] For nitrate

salt solutions of $Mg(NO_3)_2$ and $Ca(NO_3)_2$ with similar concentrations (2.6 m and 3.3 m), however, as shown in Figure 6.2a-b, the 3400 cm^{-1} band intensity does not vary with the polarizability of the cation, though Ca^{2+} has a polarizability ten times as high as that of Mg^{2+}. The polarizability magnitude of the divalent cations is however much smaller than that of the halides as shown in Table 6.1. Additional Raman experiments of chloride solutions, $MgCl_2$ and $CaCl_2$, were conducted and results show that $MgCl_2$ and $CaCl_2$ have the same Raman intensity of the 3400 cm^{-1} band (spectra not shown here). The experiments on chlorides further reveal that Raman intensity is not sensitive to the polarizability of the cation. Therefore, it is highly likely that the anion solvation effects rather than the cation solvation effects are the dominant factor that influences the 3400 cm^{-1} band intensity, and as the size and the polarizability of the anion increases, the hydrogen-bonding network of water becomes increasingly disrupted by the solvation of anions.[38]

The VSFG spectra of aqueous $Mg(NO_3)_2$, $Ca(NO_3)_2$, and $Sr(NO_3)_2$ solutions with the same concentrations as was used in Raman and IR studies are presented in Figure 6.3. The VSFG spectrum of neat water is plotted for comparison. Upon the addition of nitrate salts, the VSFG spectra show a depletion in the 3200 cm^{-1} band, an intensity enhancement in the 3400 cm^{-1} band, and an intensity decrease in the 3700 cm^{-1} peak relative to neat water. The enhancement of the 3400 cm^{-1} band amplifies as the cation of the nitrate salt varies from Mg^{2+} to Ca^{2+} to Sr^{2+}. Additional VSFG experiments of lower

concentration (0.5 m) $Mg(NO_3)_2$ (the inset of Figure 6.3a) suggest that the spectral changes become more significant with increasing concentration.

The VSFG spectra at the air-aqueous nitrate interface provide information of the effects of nitrate salts on the hydrogen-bonding network of water at the air-aqueous interface. Recall that VSFG transition moments are related to Raman and IR transition moments;[22,23,26] therefore, it is not surprising to observe an intensity decrease of the 3200 cm^{-1} band in the VSFG spectra of the nitrate solutions relative to neat water. The intensity loss of the 3200 cm^{-1} band in the VSFG spectra is correlated with the perturbation of ions on the strong hydrogen-bonding network of interfacial water molecules. Although if we think about this with respect to a shift in population, the VSFG spectrum is sampling the solvation shell of the ions (3400 cm^{-1} band) and since there are six to seven water molecules per ion, there are few water molecules that are strongly hydrogen bonded to other water molecules.

The Shutz group proposed the presence of contact ion pairs in the surface zone of salt solutions that would neutralize the electric double layer and therefore diminish the 3200 cm^{-1} band.[74] In the case of $Ca(NO_3)_2$ and $Sr(NO_3)_2$ solutions, the formation of contact ion pairs between the metal cation and the interfacial nitrate anion is possible and may contribute to the intensity loss of the 3200 cm^{-1} band of the VSFG spectra shown in Figure 6.3b-c. In the case of $Mg(NO_3)_2$, however, as suggested by the VSFG study of the symmetric stretching modes of nitrate,[40] interfacial nitrate is relatively free from Mg^{2+}

Coulombic effects and the association between Mg^{2+} and nitrate is relatively weak. Yet, the presence of solvent-separated and solvent-shared ion pairs is possible. Therefore, the observed depletion of the 3200 cm^{-1} band of the VSFG spectra (Figure 6.3) is likely due to the displacement of interfacial water molecules by ions and relevant ion pairs.

Consistent with the Raman contribution to the VSFG spectra, the VSFG spectra of nitrate salt solutions (Figure 6.3) reveal an intensity enhancement of the 3400 cm^{-1} band relative to neat water. This intensity increase is associated with water molecules solvating the ions and ion pairs, and disrupting the hydrogen-bonding network at the air-aqueous interface. Inconsistent with the Raman spectra, however, the increase in intensity of the 3400 cm^{-1} band in the VSFG spectra amplifies with the size of the cation ($Mg^{2+} < Ca^{2+} < Sr^{2+}$). This intensity difference of the 3400 cm^{-1} band is unique at the interface.

It is likely that an increase in interfacial depth accounts for the VSFG intensity differences of the 3400 cm^{-1} band. The VSFG intensity is a function of number density and orientation of molecules at the interface. An increase in interfacial depth would increase the number of molecules probed by VSFG and thus the intensity of VSFG. In VSFG studies, the interface is defined by the concentration gradient of different species and lack of an inversion center; the bulk begins where the concentrations are homogeneously mixed and there is macroscopic inversion symmetry.[38,94] Nitrate anions in the air-aqueous interfacial region attract the metal cations toward the interface. At the same time, the cations also impose a bulk-driving force on the nitrate anions at the

interface, according to Newton's Third Law.[88] Based on a recent VSFG study of nitrate aqueous interfaces,[40] for cations with relatively large size and low surface charge density, for instance, Sr^{2+} and Ca^{2+}, the metal-nitrate ion pairing (the interaction between metal cations and interfacial nitrate anions) is enhanced relative to Mg^{2+}. Therefore, we expect that the water solvation of ions and ion pairs also varies with cation identity. The ion pairing and the water solvation account for the distribution inhomogeneity of ions in the interfacial region, and different metal cations have different effects. It is likely that for nitrate solutions with large size of divalent metal cations, the interface probed by VSFG extends deeper into the solution. In other words, the concentration gradient extends over a larger region for $Sr(NO_3)_2$ and $Ca(NO_3)_2$ solutions relative to $Mg(NO_3)_2$. This could explain the observed 3400 cm^{-1} band enhancement in the VSFG spectra, which follows the trend $Mg(NO_3)_2 < Ca(NO_3)_2 < Sr(NO_3)_2$.

The VSFG spectra of the nitrate salt solutions reveal an intensity decrease in the 3700 cm^{-1} free OH peak relative to neat water, as shown in Figure 6.3. Although clearly resolved in our spectra and shown in the VSFG nitrate studies completed by the Shultz group,[74] the intensity decrease in the 3700 cm^{-1} peak is not observed in other VSFG studies of aqueous inorganic salt solutions.[38,94,95] Such intensity decrease is observed for acid solutions however.[87] The interfacial water structure was proposed to undergo a structural reorganization upon the addition of acid, resulting in a decrease of the number of OH bonds projecting into the air.[87] According to our pH measurements, the pH of

$Ca(NO_3)_2$ and $Sr(NO_3)_2$ solutions is close to that of nanopure water, while $Mg(NO_3)_2$ solutions are slightly more acidic. Relative to previous air-aqueous acid interfacial studies,[87] the pH of nitrate salt solutions is not significantly impacting the free OH intensity.

Lower free OH population density is suggested from the observed intensity decrease for the 2.6 m and 3.3 m solutions relative to neat water. The orientation changes of the interfacial free OH could also account for an intensity decrease of the 3700 cm^{-1} peak. Additional polarization studies will be completed to rule out orientation changes. The populations of free OH for neat water, acid, base, and inorganic salt solutions were quantified by previous MD simulations.[21,86,94] Results showed that the density of free OH bonds was higher in the interfacial region than in the bulk for all systems, as one would expect. The differences between neat water and inorganic salt solutions with concentrations 1 M to 2 M (2 M to 4 M total ions) were not significant. For a more concentrated aqueous solution of 6.8 M $NaNO_3$ (13.6 M total ions), however, the density of free OH bonds was found to be less than that of neat water.[21] The concentrations used in our study were ~6 M to 9 M total ions (i.e. between 4 M and 13.6 M of the MD simulations). Thus, the lower free OH intensity at 3700 cm^{-1} for 2.6 m and 3.3 m metal-nitrate solutions (Figure 6.3a-c) compared to neat water and 0.5 m $Mg(NO_3)_2$ (Figure 6.3a inset) suggests a decrease in the free OH population upon the addition of divalent metal-nitrate salts. The population of free OH continues to decrease with increasing

nitrate concentration.

6.4 Conclusions

The air-aqueous interface of a series of divalent metal-nitrate solutions was investigated using vibrational sum frequency generation spectroscopy in the OH stretching region of liquid water. Raman and infrared spectroscopies were also employed to compare the effects of ions on water structure of the bulk solution to that of the interface. The sum frequency spectra show a depletion of the strong hydrogen-bonded water OH stretch, an intensity enhancement of the water OH stretch in the relatively weak hydrogen-bonding network, and an intensity decrease of the free OH peak upon the addition of nitrate salts to neat water. These VSFG spectral changes indicate that the interfacial water hydrogen-bonding network is disturbed by the presence of ions, formation of ion pairs, and the water solvation of ions and ion pairs. Comparison of the interfacial and the bulk vibrational structure reveals differences at the air-aqueous interface relative to the bulk. A thickening of the air-aqueous interfacial region is suggested as the size of the divalent metal cations increases.

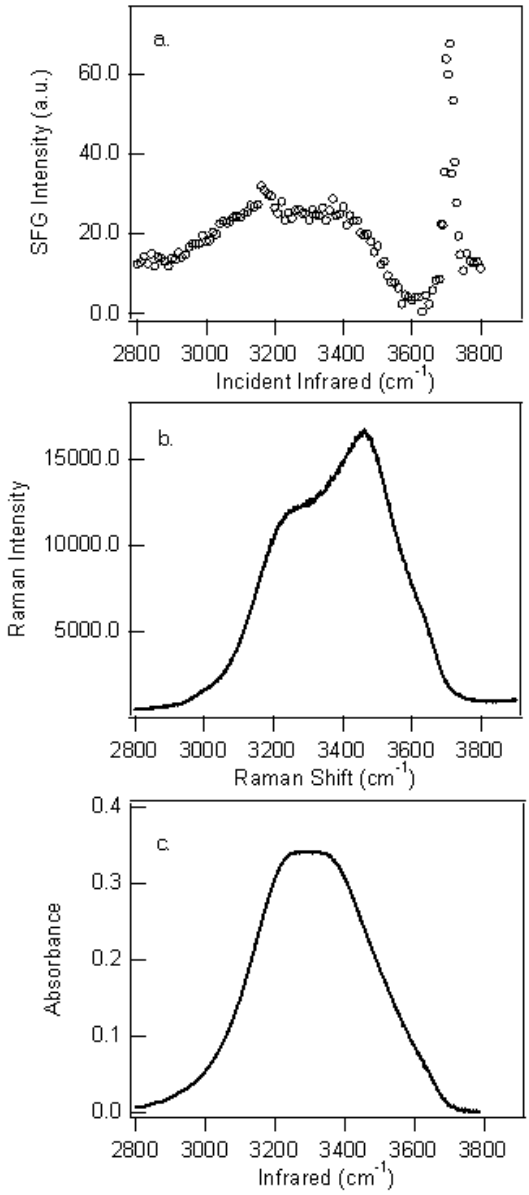

Figure 6.1 (a) ssp-polarized VSFG spectrum of the air–water interface; (b) Raman spectrum of neat water; (c) IR spectrum of neat water.

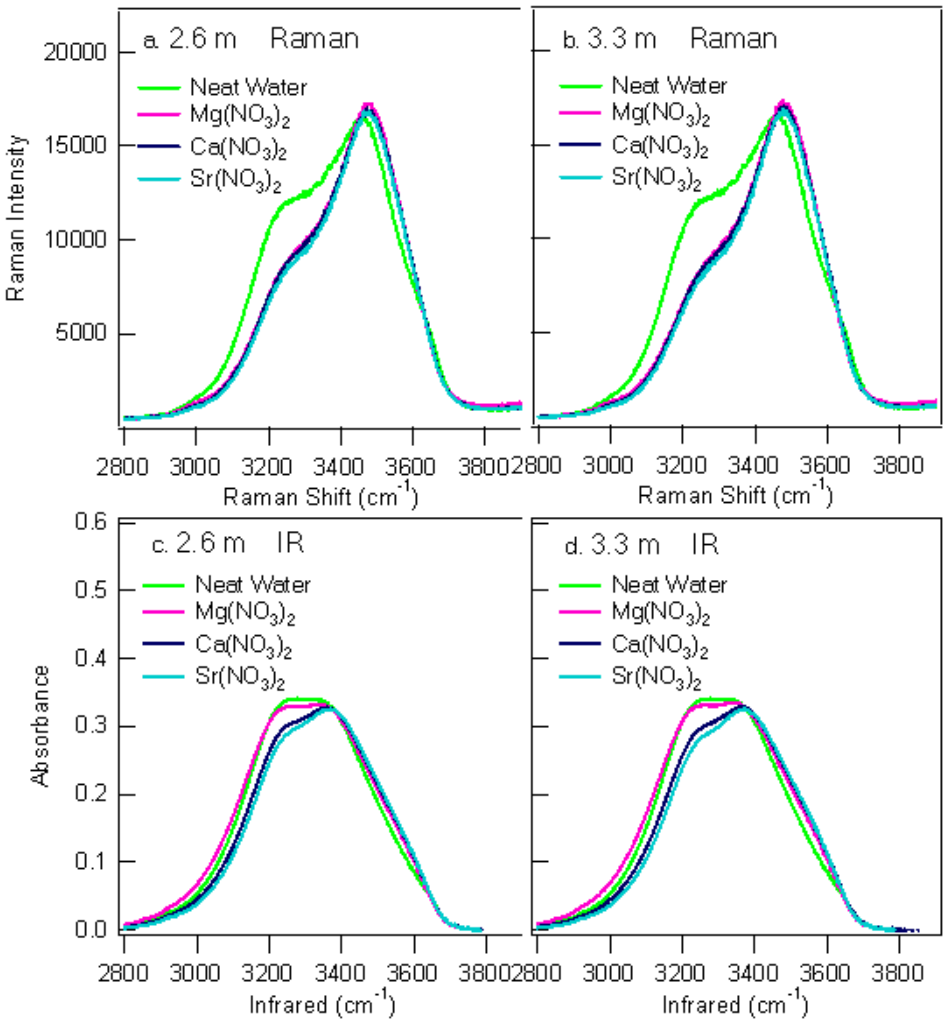

Figure 6.2 Raman and infrared spectra of aqueous nitrate solutions and neat water: a) Raman spectra of nitrate solutions with concentration 2.6 m; b) Raman spectra of nitrate solutions with concentration 3.3 m; c) IR spectra of nitrate solutions with concentration 2.6 m; d) IR spectra of nitrate solutions with concentration 3.3 m. The spectrum of neat water is plotted in each figure for comparison.

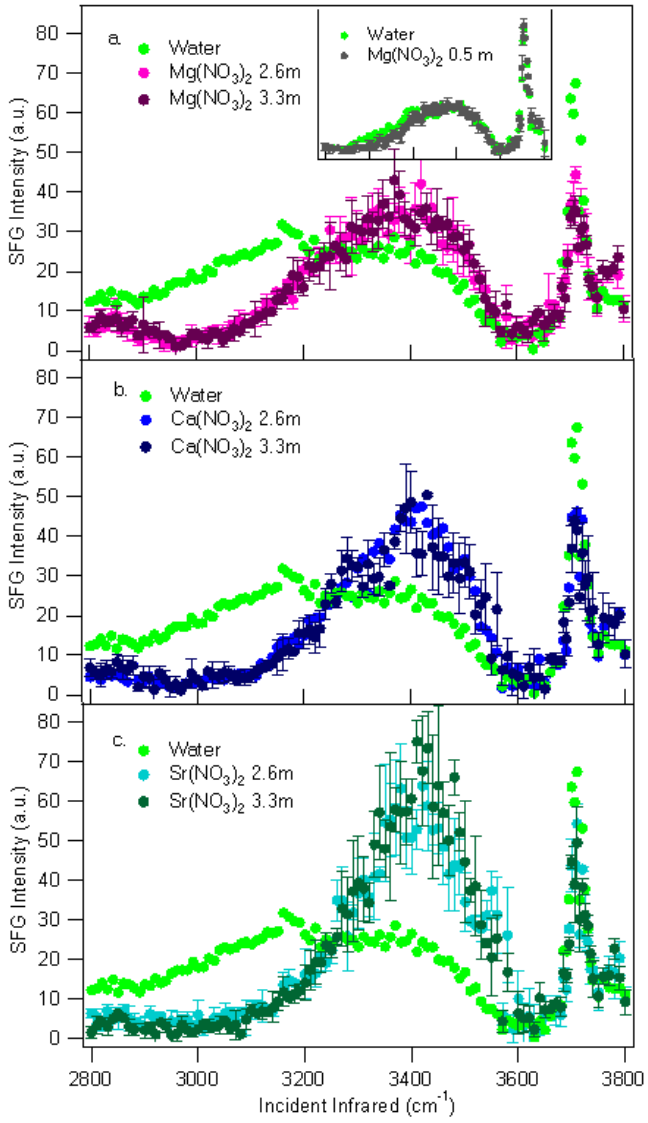

Figure 6.3 ssp-polarized VSFG spectra of (a) 2.6 m and 3.3 m $Mg(NO_3)_2$, (b) 2.6 m and 3.3 m $Ca(NO_3)_2$, (c) 2.6 m and 3.3 m $Sr(NO_3)_2$. Inset of (a) ssp-polarized spectrum of 0.5 m $Mg(NO_3)_2$. The neat water VSFG spectrum is plotted in each figure for comparison.

Polarizabilities ($bohr^3$) B3PW91/6-311++G(2df,2p)	
Be^{2+}	0.045
Mg^{2+}	0.317
Ca^{2+}	3.191
Sr^{2+}	-
F^-	5.157
Cl^-	18.783
Br^-	30.994
I^-	-
NO_3^-	27.231

Table 6.1 Polarizability values of cations and anions.[4] Sr^{2+} and I^- polarizabilities did not converge.

[4] Polarizability values are provided by Rick Spinney at The Ohio State University.

CHAPTER 7

ETHYLENEDIAMINE AT AIR-AQUEOUS AND AIR-SILICA INTERFACES

The adsorption of pollutants onto mineral oxide surfaces plays a critical role in the spatial and temporal extent of contaminant migration and transformation in the environment.[96,97] Adsorption affects the mobility and distribution of organic pollutants in the unsaturated soil zone, and in the atmospheric heterogeneous reactions with mineral aerosols. The development and refinement of effective remediation techniques requires accurate understanding of adsorption mechanisms at the mineral oxide surfaces. Therefore, the aim of the present work is to provide molecular level information of organic adsorption onto mineral oxide surfaces to elucidate adsorption mechanisms, and to determine the surface acidity of one important mineral oxide – silica.

Ethylenediamine ($H_2N(CH_2)_2NH_2$, EDA), which has the amine moieties of many widely used environmental contaminants, is employed as the representative model molecule in the present study. EDA and similar molecules 1,3-diaminopropane and 1,4-diaminobutane are industrially important and have a wide variety of applications such as chelating agents for metal ions and corrosion inhibitors in metal-liquid systems. Yet, EDA itself is of environmental interest although it has been shown not to be carcinogenic or genotoxic.[98] Among the different equilibrium conformations of EDA, the lowest

energy conformers have a gauche NCCN arrangement, stabilized by intramolecular hydrogen-bonding.[99-102]

Previous theoretical and experimental studies have been completed on the adsorption of chemical compounds with amine groups onto silica surfaces.[103-112] Infrared spectroscopy has been widely used to study the adsorption of amine compounds onto silica surfaces.[104,109-112] ^{13}C NMR spectroscopy was also used to observe the interactions between the adsorbed amines and the surface acid sites of silica based on the chemical shift differences between the free and the adsorbed molecules.[106] Adsorption kinetics of polyamidoamine dendrimers onto silica surfaces was investigated with total internal reflection fluorescence correlation spectroscopy (TIR-FCS).[108] X-ray photoelectron spectroscopy (XPS) was employed to understand the interactions between the adsorbed amine compounds and the silica surfaces as well as the amount and structure of the adsorbed amines.[104,105,107] Two possible mechanisms of amine compound adsorption onto the silica surface have been suggested by previous studies:[103,104] (1) amine groups form hydrogen-bonds with the surface silanol groups; (2) amines are chemisorbed onto the silica surface through protonation reactions.

In the study presented here, the possible adsorption mechanisms of EDA onto silica surfaces are evaluated by investigating EDA at the air-amorphous SiO_2 interface as well as EDA and its protonated products at the air-aqueous interface using vibrational sum frequency generation spectroscopy. Results show that the VSFG spectrum of EDA

adsorbed on the silica surface and that of the singly protonated EDA solution are similar in both CH and NH stretching regions. The spectral similarities indicate that EDA molecules are strongly chemisorbed to the silica surface through the protonation of one EDA amine group by surface silanol OH groups, thereby forming a $(H_2N(CH_2)_2NH_3)^+(O\text{-}Si\equiv)^-$ surface complex. The surface acidity of the silanol OH groups (pK_a (HOSi≡)) is therefore quantified to be between the two pK_a values of EDA (in the range of 7.56 to 10.71) at the air-silica interface.

7.1 Materials

The infrared-grade fused amorphous silica plates were purchased from Quartz Plus Inc. Ethylenediamine (redistilled, 99.5+%), ethylenediamine dichloride (98%), and hydrochloric acid (37.5%) were purchased from Aldrich and used as received. Solutions were prepared using Nanopure water with a resistivity of 18.0-18.3 MΩ cm. All solutions were only in contact with glass and Teflon throughout sample preparation.

7.2 Experimental Method

The infrared-grade amorphous silica plates were heated in a muffle oven at 900 ºC for more than 12 hours before experiments to remove organics from the silica surface. After the silica plates were cooled to room temperature (297±2 K), they were placed under ambient conditions for half an hour before the VSFG experiments were performed to

ensure equilibrium with water vapor in the air (relative humidity 50±3%). Relative humidity was measured by a traceable hygrometer (Fisher Scientific) with an accuracy of ±0.2%. The adsorption experiment was performed by placing the silica plate into a sealed bottle with saturated EDA vapor (vapor pressure 11.4 mmHg[113]) for 30 minutes, and was then purged with carbon free dry air (< 1ppm CO_2 and water vapor) from FTIR purge gas generator (Parker Balston, model 75-62NA) for the specified amount of time.

The 10 Hz scanning VSFG system was employed as the primary instrument for this study. The VSFG spectra were obtained before and after organic adsorption. The polarization were ssp or sps for the sum frequency, visible, and infrared light beams, respectively. Both ssp and sps spectra are shown in this dissertation, with discussion focusing on the ssp-polarized VSFG spectra. Detailed information of VSFG instrumentation can be found in section 3.1.

The surface tension values of ethylenediamine aqueous solutions were obtained by using a DeltaPi Tensiometer (Kibron Inc.). Neat water (Nanopure, with a resistivity of 18.3 MΩ cm) was used for calibration. All measurements were completed at constant temperature (297±2 K). Estimation of the surface mole fractions according to the surface tension values[114-116] is described in Appendix C.

7.3 Results and Discussion

Ethylenediamine at the air-aqueous interface. The VSFG spectra of EDA solutions at the air-aqueous interface were acquired to establish reference systems of vibrational frequencies to compare against the VSFG spectra from the air-silica interfacial adsorption studies. The ssp-polarized VSFG spectra of EDA aqueous solutions at air-aqueous interfaces are shown in Figure 7.1b-c. The spectrum of neat water is shown in Figure 7.1a for comparison. Of importance to this study are the neat water assignments of the 3700 cm^{-1} peak to the free OH of surface water, and the 3000 cm^{-1} to 3600 cm^{-1} region to the hydrogen-bonded stretching region of interfacial water. Although vibrational frequencies of infrared, Raman, and VSFG spectra do not exactly correspond with one another, these frequencies are generally within a few wavenumbers.[117-119] Thus, the peak assignments of VSFG spectra in the present study are based upon Raman and infrared spectra from the literature.[120-123] In the CH stretching region (2800-3000 cm^{-1}), the peak around 2860 cm^{-1} is assigned to the CH_2 symmetric stretching (CH_2-SS) modes, and the peak around 2920 cm^{-1} is attributed to the CH_2 asymmetric stretching (CH_2-AS) modes.[120,122] In order to obtain accurate CH peak positions, the VSFG spectra of 0.05 m.f. and 0.2 m.f. EDA aqueous solutions were fit using Lorientzian profiles in the CH stretching region. The component peaks are shown as dashed lines in Figure 7.1. The fitting results are summarized in Table 7.1.

The VSFG spectra can provide information about the orientation of surface molecules.

Based on the VSFG intensity ratios of the CH_2 symmetric and asymmetric stretching modes, the average orientation angles of methylene groups were calculated,[124-126] as listed in Table 7.1 (calculations are shown in Appendix D). According to the orientation calculations, the average tilt angle of CH_2 groups for the 0.05 m.f. EDA solution surface is 43° ± 5° from the surface normal, while this tilt angle for 0.2 m.f. EDA is 50° ± 3°. Thus, the CH_2 orientation angle of the 0.2 m.f. EDA solution surface and that of the 0.05 m.f. solution surface are similar.

The NH stretching frequencies overlap with the hydrogen-bonded OH stretching frequencies of water, as shown in Figure 7.1. According to previous assignments for infrared and Raman spectra,[120-123] there are two NH stretching peaks at ~3300 cm^{-1} and ~3360 cm^{-1} that overlap with the broad hydrogen-bonded OH stretching bands of water. The ~3300 cm^{-1} and ~3360 cm^{-1} peaks are assigned to the NH_2 symmetric stretching (NH_2-SS) and NH_2 asymmetric stretching (NH_2-AS) modes respectively. The dip observed in the VSFG spectra is due to the destructive interferences between NH_2-SS and NH_2-AS modes and/or between the NH stretching modes of EDA and the hydrogen-bonded OH stretching modes of water. Since the NH stretching and the hydrogen-bonded OH stretching modes have contributions to the intensities in the 3000-3600 cm^{-1} region and the peaks are relatively broad compared to the peaks of the CH stretch, it is difficult to deconvolute the contributions of each vibrational mode. One solution to this problem, although not within the scope of this study, could be studying the VSFG spectra of N-

deuterated EDA aqueous solutions (ND versus NH vibrations). (ND stretching peaks lie in the 2300-2550 cm^{-1} region, and these peaks are not affected by vibrational modes of water.[123])

In the VSFG spectra shown in Figure 7.1a-c, the peak at 3700 cm^{-1} is assigned to the free OH stretch of water molecules.[127-129] The VSFG intensities of the free OH peak are reduced in the 0.05 m.f. and 0.2 m.f. EDA solutions compared to neat water. Since the VSFG response is proportional to the square of the interfacial number density and is related to the orientation of surface molecules, the concentrations of EDA at the interface were estimated through surface concentration analysis based on the surface tension measurement results. The calculated surface mole fractions ($m.f._s$) are approximately 0.08 $m.f._s$ and 0.3 $m.f._s$, for 0.05 m.f. and 0.2 m.f. EDA solutions, respectively (see Appendix C for details of calculations). Therefore, the mole fraction of the surface water molecules for the 0.08 $m.f._s$ EDA and the 0.3 $m.f._s$ EDA are 0.9 $m.f._s$ H_2O and 0.7 $m.f._s$ H_2O, respectively. The square root of the VSFG intensity ratio from the free OH peak in the 0.05 m.f. EDA and 0.2 m.f. EDA spectra (Figure 7.1b-c, and c inset) is 1.3. This corresponds to the mole fraction ratio of interfacial water molecules (0.9/0.7=1.3), indicating that the orientation of the free OH does not change significantly in the interfacial region of the 0.2 m.f. EDA solution compared to that of the 0.05 m.f. solution. This is approximately consistent with the VSFG spectra with the sps polarization combination, as shown in Figure 7.2. Although the surface tension and the resulting

surface number density calculations reveal that there are less water molecules in the surface region relative to the bulk, the surface of the EDA solutions is still water-rich.

Ethylenediamine at the air-silica interface. The VSFG spectra of the amorphous silica surface before and after exposure to EDA vapor are shown in Figure 7.3. As discussed in previous work,[130,131] at ambient conditions with relative humidity (RH) at around 50%, the VSFG spectrum of silica at the air-silica interface (Figure 7.3a) shows low-intensity hydrogen-bonded OH stretch bands in the 3000-3600 cm^{-1} region but a sharp, high-intensity isolated silanol OH stretching peak at ~3750 cm^{-1}. This suggests that at 297 K and 50% RH, water molecules only cover a limited portion of the hydrated silica surface in island-like formations, and that the isolated silanol OH groups are present as the major surface species. After exposure to EDA vapor, the significant VSFG responses from the CH and NH stretching modes in Figure 7.3b and c suggest the adsorption of EDA molecules to the silica surface. The suppression of the silanol OH peak reveals that the adsorption occurs through the interaction between the surface silanol OH groups and the amine groups of the EDA molecules.

VSFG spectra of the silica surface after being exposed to EDA vapor and being purged with organic free air for 5 minutes and then for 24 hours are shown in Figure 7.3b and c, respectively. One would expect that there should be less EDA molecules on the silica surface after longer purging times, and, as a result, the VSFG response might decrease after 24 hours purging compared to 5 minutes purging. However, the peak

intensities obtained after 24 hours purging have increased by a factor of about 4 in both the CH and the NH stretching regions compared to the peaks in the spectrum obtained after 5 minutes purging.

A possible scenario to explain the differences between Figure 7.3b and c is that there is a liquidlike layer on the silica surface after the initial EDA adsorption, and this layer persists when purging for 5 minutes. The liquidlike layer may reevaporate or transform irreversibly into other states after longer purging time due to drying of the silica surface.[132] The VSFG spectra with 5-minute purging and 24-hour purging may suggest two different stages of adsorption: a physisorbed (metastable precursor) stage where the interactions are largely due to van de Waals forces, and a chemisorbed stage where the interactions between the sorbant and the sorbate are much stronger.[132] The differences of the spectral features (peak intensity, position, ratio etc.) between the short and the long purging times suggest that the liquidlike layer is removed and only strongly adsorbed EDA remains upon drying. Another possibility is that the surface EDA molecules change their coordination upon purging. However, it is beyond the scope of this work to fully elucidate the liquidlike state, as further described below.

The persistence of the EDA molecules on the silica surface after longer purging times indicates that EDA uptake by silica is at least partially irreversible. Under the purging condition with 24 hours, the adsorption-desorption process reaches equilibrium since there is no significant spectral change observed after purging for times greater than 24

hours (spectra not shown here). Consequently, the VSFG spectrum of silica exposure to EDA with the 24-hour purging time reveals the adsorption mechanism between EDA molecules and the SiO_2 surface. To elucidate the adsorption mechanism, the 24-hour purging spectrum was compared to spectroscopic signature frequencies of other carefully chosen systems.

Adsorption mechanism—hydrogen bonding versus protonation. There are four possible adsorption mechanism scenarios as shown in Figure 7.4. In scenario I, there is a liquidlike aqueous layer on the silica surface. In scenario II, the amine groups of EDA form hydrogen-bonds with the surface silanol OH groups, with the amine group acting as a proton acceptor and the silanol group being a proton donor. In scenarios III and IV, the amine groups of EDA molecules are protonated by the surface silanol OH groups and form $(H_2N(CH_2)_2NH_3)^+(O\text{-}Si\equiv)^-$ complexes through ionic bonds. In scenario III, only one of the two amine groups of the EDA molecule is protonated ($H_2N(CH_2)_2NH_3^+$), while both of the amine groups are protonated ($^+H_3N(CH_2)_2NH_3^+$) in scenario IV. In all four scenarios, water can coexist on the surface (recall ~50% RH).

EDA is a medium-strong base with $pK_{a1} = 7.56$, $pK_{a2} = 10.71$ for its conjugate acids:

$$^+H_3N(CH_2)_2NH_3^+ \rightarrow H_2N(CH_2)_2NH_3^+ + H^+ \qquad K_{a1} \qquad (7.1)$$

$$H_2N(CH_2)_2NH_3^+ \rightarrow H_2N(CH_2)_2NH_2 + H^+ \qquad K_{a2} \qquad (7.2)$$

The reported pK_a values for surface silanol OH groups are generally less than 9.0.[133-136] The interaction between the silanol functional groups on the silica surface and EDA can

be described as an acid-base reaction because the acid-base (BrØnsted) reaction can take place when the pK_a of the acid is smaller than that of the conjugate acid of the base. In other words, the adsorption mechanisms in scenarios III and IV are highly probable for EDA adsorption to the silica surface.

In this study, the VSFG spectra of aqueous EDA solutions were used to establish three reference systems: doubly protonated EDA, singly protonated EDA, and isolated EDA. The doubly protonated EDA solution was prepared using ethylenediamine dichloride ($ClH_3N(CH_2)_2NH_3Cl$, EDD) and water. The singly protonated EDA solution was prepared by controlling the pH of the EDA solution with aqueous HCl to be 9.07 (95% of EDA molecules are singly protonated EDA at this pH as determined by the acidity constants). The isolated (nonprotonated) EDA solution was prepared as a 0.05 m.f. EDA aqueous solution. Amine groups in EDA molecules are expected to be the functional groups interacting with the silica surface sites. However, the NH stretching peaks overlap with OH stretching peaks and are generally broadened due to the hydrogen-bonding with neighboring water molecules, and therefore, NH stretching peaks are not used as a spectral reference. In this study, the CH stretching peaks were used to reveal the interaction between the sorbate molecule and the sorbant surface since these peaks are well separated from other spectral features. Recall that the vibrational frequency provides information on the chemical bond and is influenced by the chemical environment.[137] Previous studies[130,137] have successfully established a spectral reference

system in the CH stretching region to study the adsorption of piperidine on silica and alumina surfaces. A similar approach was applied to elucidate the viability of the adsorption mechanisms for the present study.

Figure 7.5 shows the VSFG spectra in the CH stretching region with the overall spectral fits for reference systems and EDA adsorbed silica surfaces. The CH_2-SS peaks were chosen as the spectroscopic reference in this study since they are better separated relative to the CH_2-AS peaks from the OH and the NH stretching peaks, and therefore have minimal spectral interference. There are three significant differences observed for the CH_2-SS peaks after protonation for the reference aqueous EDA solutions. First, the CH_2-SS peak splits into two prominent peaks for both singly and doubly protonated EDA aqueous solutions. This reveals that protonation changes the distribution of the EDA conformations in the interfacial region. Second, due to the protonation, the orientation of the EDA molecules changes significantly. Assuming C_{2v} symmetry for the CH_2 groups in EDA and that the bond angle is 109.5°, orientation calculations show that the average tilt angle of the CH_2 groups in EDA molecules is 43 ± 5^o (0.05 m.f. EDA solution) and 50 ± 3^o (0.2 m.f. EDA solution), while this angle changes to 86 ± 4^o (0.07 m.f. singly protonated EDA solution) and 82 ± 2^o (0.05 m.f. doubly protonated EDA solution) after protonation, as listed in Table 7.1 (see Appendix D for details of calculations). Third, the peak position of the CH_2-SS blue shifts from ~2862 cm^{-1} for the 0.2 m.f. EDA aqueous solution to ~2872 cm^{-1} for the singly protonated EDA aqueous solution, and eventually to

~2883 cm^{-1} for the doubly protonated EDA aqueous solution (Figure 7.5, Table 7.1). This result is consistent with previous studies, which revealed that protonation causes a blue shift of the CH_2-SS peak for piperidine in aqueous solution as well as on silica and alumina surfaces.[130,137]

Compared to the reference spectra (Figure 7.5a-c), the VSFG spectrum of EDA adsorbed onto the silica surface with 5 minutes purging (Figure 7.5d) has the spectral features of several species. The peak position of the probe peak in the VSFG spectrum with 5 minutes purging (~2881 cm^{-1}) is close to that from the doubly protonated EDA solution (~2882 cm^{-1}); however, orientation results show that the surface CH_2 has a similar average orientation angle (~48°) to that of the isolated EDA solution (~43°) (see Table 7.1). One explanation is that with the 5-minute purging time, EDA molecules form a liquidlike aqueous layer on the silica surface (scenario I of Figure 7.4), and this liquidlike layer together with the underlying liquid/silica interface has contributions to the VSFG response.

After 24 hours purging for the EDA adsorbed silica surface (Figure 7.5e), the VSFG response is from the interfacial EDA-silanol complex. The VSFG spectrum of EDA adsorbed to the silica surface after 24 hours purging reveals the splitting feature of the CH_2-SS peak and a similar average CH_2 orientation angle (~81^o) compared to that of the reference systems of singly (Figure 7.5b) and doubly protonated (Figure 7.5c) EDA solutions. Both features strongly suggest that EDA molecules adsorbed on the silica

surface are protonated by the silanol groups. In addition, the probe peak position (~2872 cm^{-1}) is nearly the same as that of the singly protonated EDA aqueous solution (~2872 cm^{-1}) as shown in Figure 7.5 and Table 7.1. Therefore, the adsorption of EDA molecules onto the silica surface occurs via protonation of an amine group by a silica surface silanol site as shown in scenario III of Figure 7.4.

In this study, we have also shown that EDA is an effective surface acidity probe molecule (pK_{a1} = 7.56 and pK_{a2} = 10.71), and that VSFG spectroscopy results reveal that the surface acidity constant of silanol OH groups (pK_a (HOSi≡)) from an amorphous silica surface is in the range of 7.56 to 10.71. This is consistent with previous studies. Eisenthal et al. showed that the planar fused silica surface had a pK_a value of 4.5 for 19% of the silanols and a pK_a value of 8.5 for 81% of the silanols based on the second harmonic results.[133] By using the bond-valence methods Bickmore et al. predicted the pK_a values of the silica surface were 7.74 and 10.45.[138]

7.4 Conclusions

A mechanistic interpretation of diamine adsorption onto mineral oxide surfaces is presented in this study. The molecular-scale spectroscopic results indicate that ethylenediamine molecules are strongly chemisorbed (through ionic forces) to the silica surface through the protonation of one amine group by surface silanol OH groups, thereby forming a $(H_2N(CH_2)_2NH_3)^+(O\text{-}Si\equiv)^-$ surface complex. The surface acidity of the

amorphous silica is quantified to be in the range of the two pK_a values of the probe molecule EDA: 7.56 to 10.71. Serving as a proxy for the interactions between organic pollutants and mineral oxide surfaces, this molecular-scale study of diamine molecule adsorption onto the silica surface enables us to have a more thorough understanding of diamine pollutant fate on soil and atmospheric particles. Furthermore, detailed information of the adsorption mechanism helps to guide the development of adsorption models, the prediction of pollutant migration in the natural environment, and the design of more efficient remediation methods for pollutant-contaminated natural systems.

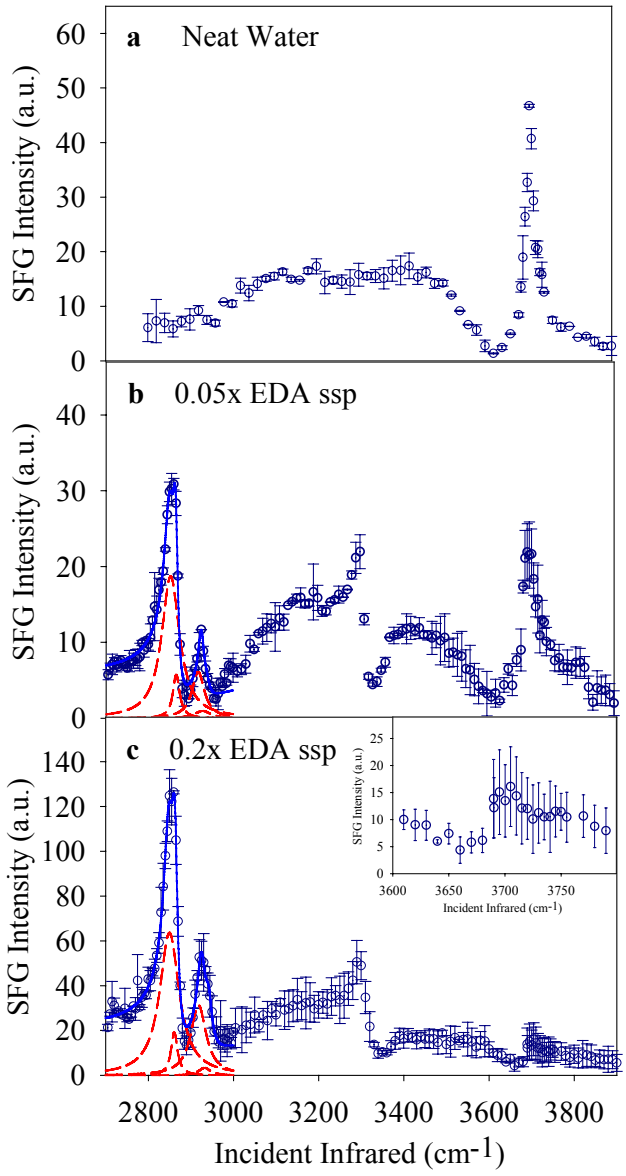

Figure 7.1 ssp-polarized VSFG spectra of a) neat water; b) 0.05 m.f. ethylenediamine at the air-aqueous interface; c) 0.2 m.f. ethylenediamine at the air-aqueous interface; inset of c) the free OH peak expanded. Dark blue circles: experimental data with error bars; blue solid lines: overall fits; red dashed lines: Lorentzian component peaks.

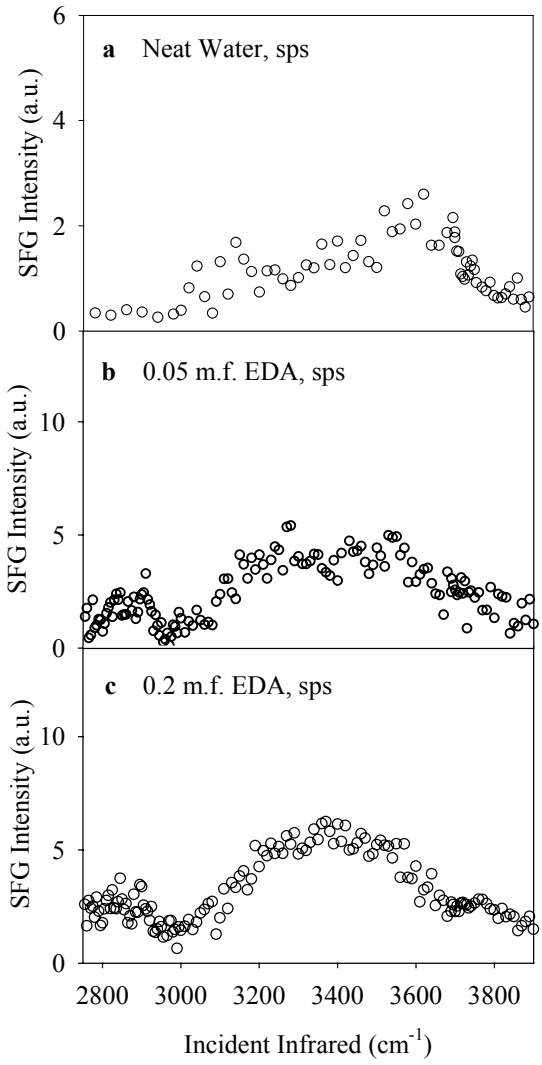

Figure 7.2 sps-polarized VSFG spectra of a) neat water (scaled to the EDA experimental conditions); b) 0.05 m.f. ethylenediamine at the air-aqueous interface; c) 0.2 m.f. ethylenediamine at the air-aqueous interface.

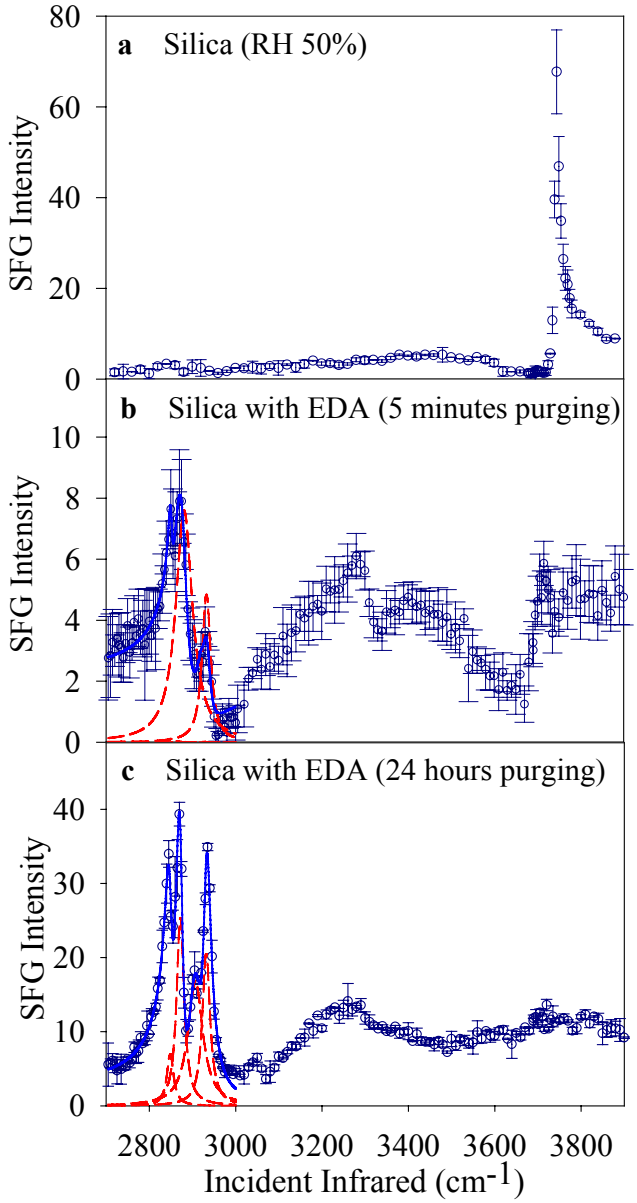

Figure 7.3 VSFG spectra of amorphous SiO_2 at the air-solid interface: a) before exposure to ethylenediamine; b) after exposure to ethylenediamine vapor and purged with organic free air for 5 minutes; c) after exposure to ethylenediamine vapor and purged for 24 hours. Dark blue circles: experimental data with error bars; blue solid lines: overall fits in the CH region; red dashed lines: Lorentzian component peaks.

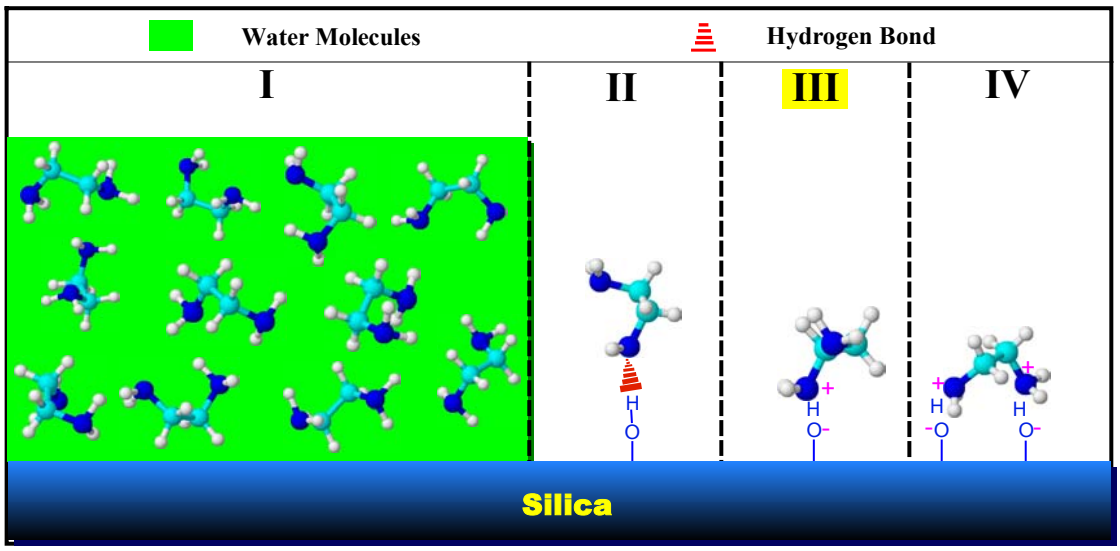

Figure 7.4 Schematic representation of adsorption scenarios: I) liquidlike aqueous layer; II) hydrogen-bonding of EDA with a surface silanol group; III) singly protonated EDA by a surface silanol group; IV) doubly protonated EDA by two surface silanol groups. In all four scenarios, water can coexist on the surface.

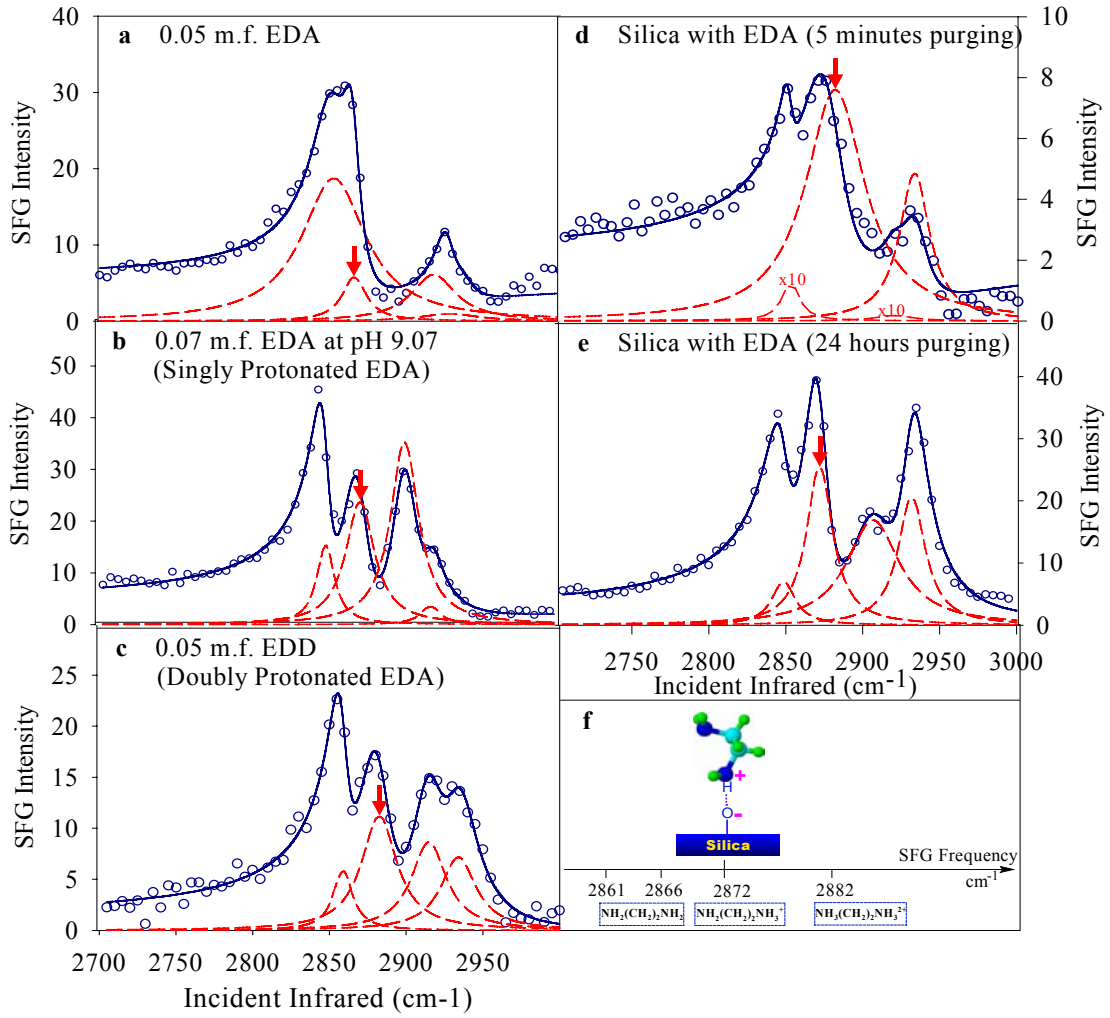

Figure 7.5 VSFG spectra in the CH stretching region of a) 0.05 m.f. ethylenediamine at the air-aqueous interface; b) 0.07 m.f. singly protonated ethylenediamine at the air-aqueous interface; c) 0.05 m.f. ethylenediamine dichloride at the air-aqueous interface; d) ethylenediamine at the air-silica interface with 5 minutes purging (component peaks at 2852.0 cm^{-1} and 2918.9 cm^{-1} have been multiplied by 10); e) ethylenediamine at the air-silica interface with 24 hours purging. Blue circles: experimental; blue solid lines: overall fits; red dashed lines: Lorentzian component peaks. f) Probe peak frequencies in the reference systems and the adsorption mechanism are shown.

	CH_2-SS (cm^{-1})		CH_2-AS (cm^{-1})		$A_{(SS)}$[5]	$A_{(AS)}$[5]	$\lvert\chi_{SS}/\chi_{AS}\rvert$	θ (degrees)
	Peak 1	Peak 2	Peak 3	Peak 4				
0.05 m.f. EDA	2852.6	2866.0	2917.7	2928.3	1501.6	368.4	2.019	43±5
0.2 m.f. EDA	2849.8	2861.2	2918.0	2932.4	5429.6	2057.3	1.625	50±3
0.07 m.f. singly protonated EDA	2849.6	2872.0	2900.9	2917.6	1134.9	1248.6	0.9534	86±4
0.05 m.f. EDD (doubly protonated EDA)	2858.8	2882.6	2914.8	2934.0	601.8	638.6	0.9708	82±2
Silica with EDA (5 min purging)	2852.0	2881.0	2918.9	2932.8	505.7	171.2	1.719	48±6
Silica with EDA (24 hr purging)	2848.7	2872.1	2906.8	2932.0	1290.0	1353.7	0.9762	81±7

Table 7.1 Curve-fitting and orientation calculation[124-126] results of VSFG spectra (see Appendix D for details of orientation calculations).

[5] $A_{(SS)}$: the area of CH_2-SS peaks; $A_{(AS)}$: the area of CH_2-AS peaks; χ_{SS}: the second order macroscopic susceptibility of CH_2-SS; χ_{AS}: the second order macroscopic susceptibility of CH_2-AS.

CHAPTER 8

ENVIRONMENTAL IMPLICATIONS AND CONCLUSIONS

The work presented in this dissertation was directed towards elucidating the interfacial ion pair formation for atmospheric aerosols and natural waters. Ion pairing at interfaces has impacts on the physical and chemical characteristics of the interface, and thus affects the migration, transformation, and fate of chemicals in the environment. Environmentally relevant interfacial systems however are usually complicated and interrelated factors coexist. Therefore, a thorough investigation of the heterogeneous chemical and physical processes that occur at such interfaces must start with careful consideration of fundamental issues. In light of this, the work presented in this dissertation focuses on a fundamental understanding of ion pairing between nitrate anions and divalent metal counterions at the air-aqueous interface.

Sum frequency, Raman, and infrared spectra reveal that the formation of ion pairs between nitrate anions and metal cations increases with increasing cation size, Mg^{2+} < Ca^{2+} < Sr^{2+}, at the interface and in the bulk. Their influences on the interfacial water structure follow the same trend, and the interfacial depth of the nitrate solution is expected to extend deeper into the bulk as the size of the cation increases. Yet, $Mg(NO_3)_2$ ion pairing properties are uniquely different at the air-aqueous interface relative to the

bulk. When the number of water molecules per ion increases by one for $Mg(NO_3)_2$ aqueous systems (3.3 m versus 2.6 m), the dominant interfacial nitrate species changes significantly, from an ion-paired nitrate to a relatively free nitrate species. Such molecular-level information of interfacial species and structure of nitrate aqueous systems provides insight into the physical and chemical processes of adsorption, desorption, and heterogeneous reactions at interfaces of nitrate aerosols and nitrate-containing aqueous systems. This information also has implications for the development and refinement of theoretical models for predicting the migration, reaction, and distribution of chemicals in the natural environment.

The surface acidity of silica was also determined in this work. The quantitative information of silica surface acidity along with the detailed understanding of ion pairing between nitrate anions and metal cations prepares us for the next step of the research, a thorough investigation of the metal-nitrate ion pair formation at silica surfaces.

APPENDIX A

VSFG SPECTRUM NORMALIZATION

The VSFG intensity is proportional to the two incident laser intensities and the square of the absolute value of the effective sum frequency susceptibility $\chi_{eff}^{(2)}$, as shown in equation 2.2. For ssp-polarized VSFG, $\chi_{eff}^{(2)}$ is associated with Fresnel factors, incident angle of IR, and χ_{yyz} by equation 2.10. Combining equation 2.2 and 2.10, we obtain that for ssp-polarized VSFG

$$I_{VSFG} = \frac{8\pi^3}{c^3 n_1(\omega_{VSFG}) n_1(\omega_{vis}) n_1(\omega_{IR})} \omega_{VSFG}{}^2 \sec^2\theta_{VSFG} \left(L_{yy}(\omega_{VSFG}) L_{yy}(\omega_{vis}) L_{zz}(\omega_{IR})\right)^2 \sin^2\theta_{IR} I(\omega_{vis}) I(\omega_{IR}) \left|\chi_{yyz}\right|^2 \tag{A.1}$$

At the air–neat water interface, medium 1 is air, and it is reasonable to assume that $n_1(\omega_{VSFG}) = n_1(\omega_{vis}) = n_1(\omega_{IR}) = 1$. $I(\omega_{vis})$ and θ_{IR} remain constant as the wavenumber changes. Therefore, I_{VSFG} is simplified,

$$I_{VSFG} = c' \omega_{VSFG}{}^2 \sec^2\theta_{VSFG} \left(L_{yy}(\omega_{VSFG}) L_{yy}(\omega_{vis}) L_{zz}(\omega_{IR})\right)^2 I(\omega_{IR}) \left|\chi_{eff}^{(2)}\right|^2 \tag{A.2}$$

c' is a constant with $c' = \frac{8\pi^3}{c^3 n_1(\omega_{VSFG}) n_1(\omega_{vis}) n_1(\omega_{IR})} \sin^2\theta_{IR} I(\omega_{vis})$.

Fresnel factors that are related to the ssp-polarized VSFG:

$$L_{yy}(\omega_{VSFG}) = \frac{2n_1(\omega_{VSFG})\cos\theta_{VSFG}}{n_1(\omega_{VSFG})\cos\theta_{VSFG} + n_2(\omega_{VSFG})\cos\gamma_{VSFG}} \tag{A.3}$$

$$L_{yy}(\omega_{vis}) = \frac{2n_1(\omega_{vis})\cos\theta_{vis}}{n_1(\omega_{vis})\cos\theta_{vis} + n_2(\omega_{vis})\cos\gamma_{vis}} \tag{A.4}$$

$$L_{zz}(\omega_{IR}) = \frac{2n_2(\omega_{IR})\cos\theta_{IR}}{n_1(\omega_{IR})\cos\gamma_{IR} + n_2(\omega_{IR})\cos\theta_{IR}}\left(\frac{n_1(\omega_{IR})}{n'(\omega_{IR})}\right)^2 \tag{A.5}$$

Refractive index of water n_2, reflection angle θ of VSFG (equation 2.1), refractive angles γ of VSFG and IR (Snell's law), and refractive index of the interface n' (equation 2.17) are all frequency dependent. Note in this section, only the real part of the complex refractive index is considered. In the VSFG system used for this study, the 10 Hz VSFG, the input visible is at 532 nm, and IR varies from 2800 cm^{-1} to 3800 cm^{-1}. The corresponding VSFG wavelength is in the range 463 nm to 442 nm, based on the fact that the frequency of VSFG is the sum of the frequencies of visible and IR beams. Refractive indices of water at different wavelengths or wavenumbers were obtained from literature[139,140] and are plotted in Figure A.1. Reflection angle θ of VSFG (equation 2.1) and refractive angles γ (Snell's law) also depend on the geometry of the VSFG system. In the system used, the incident angles of visible and IR beams were set to be 45° and 53° to the surface normal. Figure A.2 gives the calculated Fresnel factors as a function of incident infrared wavenumbers for $L_{yy}(\omega_{VSFG})$ and $L_{zz}(\omega_{IR})$. $L_{yy}(\omega_{vis})$ has a value of 0.768.

For the VSFG spectra presented in this dissertation (except in this Appendix) and

published before,[39,131] the real-time IR profile was used to normalize the VSFG spectra. Figure A.3a shows one VSFG spectrum (raw data) at the air–neat water interface obtained with the 10 Hz scanning VSFG system. Figure A.3b shows the VSFG spectrum of neat water with IR normalization. In the spectrum shown in Figure A.3c, however, $\omega_{VSFG}{}^2 \sec^2\theta_{VSFG}\left(L_{yy}(\omega_{VSFG})L_{yy}(\omega_{vis})L_{zz}(\omega_{IR})\right)^2$ as well as the IR intensities were employed for VSFG spectrum normalization. Differences in the hydrogen-bonded OH stretching region are observed when using different normalization methods, as expected.

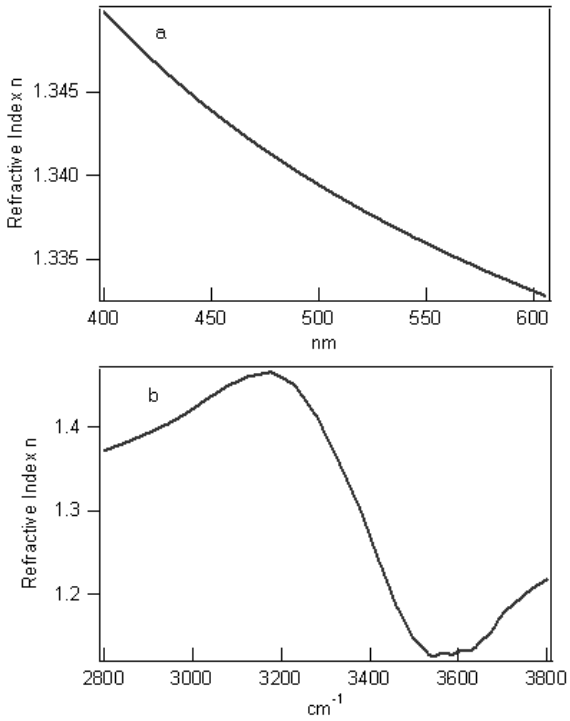

Figure A.1 (a) Refractive index of water as a function of wavelength in the visible region; (b) Refractive index of water as a function of wavenumbers of IR.[139,140]

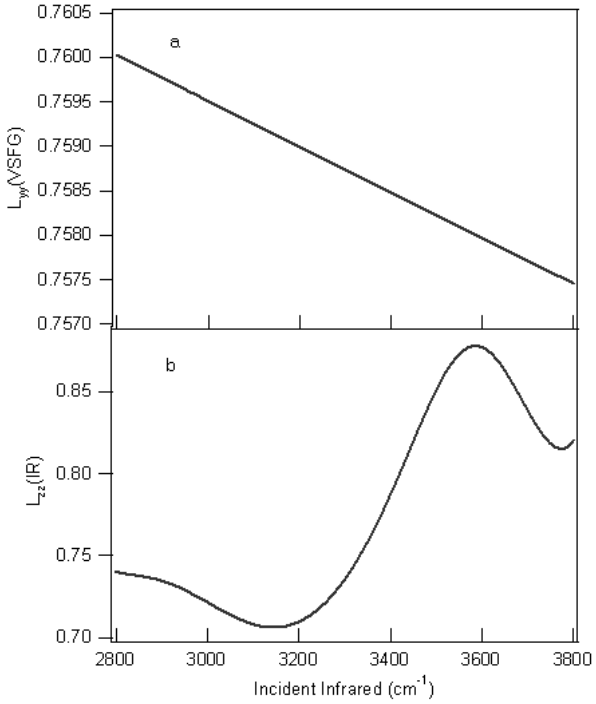

Figure A.2 Fresnel factors $L_{yy}(\omega_{VSFG})$ and $L_{zz}(\omega_{IR})$ as a function of wavenumber of incident IR.

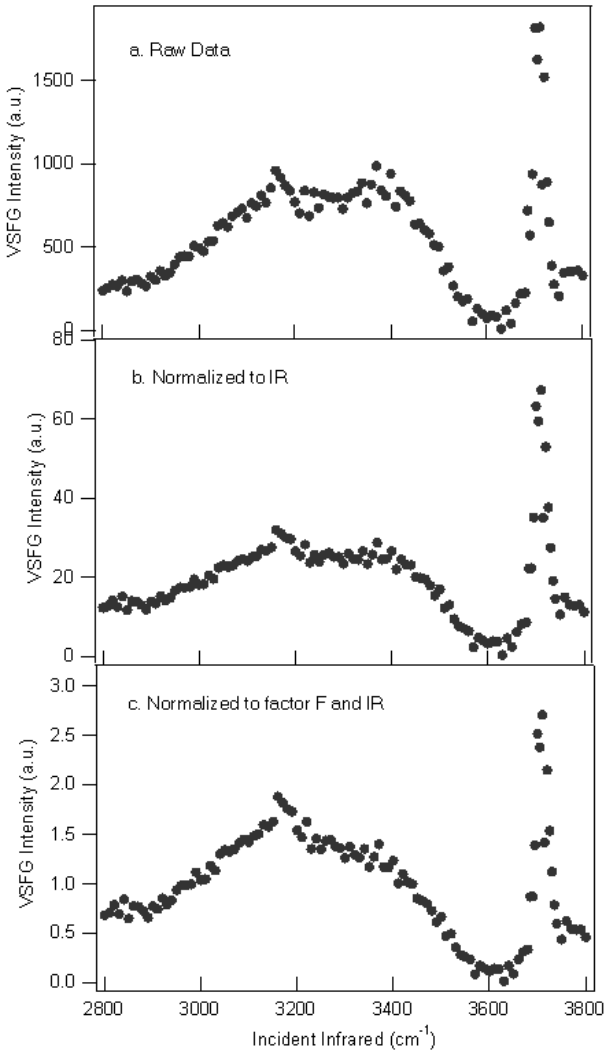

Figure A.3 ssp-polairzed VSFG spectra at the air–neat water interface: (a) VSFG spectrum before normalization; (b) VSFG spectrum normalized to real-time IR; (c) VSFG spectrum normalized to F factor (F= $\omega_{VSFG}{}^2 \sec^2\theta_{VSFG}\left(L_{yy}(\omega_{VSFG})L_{yy}(\omega_{vis})L_{zz}(\omega_{IR})\right)^2$) and real-time IR.

APPENDIX B

LOW-FREQUENCY RAMAN INSTRUMENTATION

In our Raman spectrometer, a Raman probe (Inphotonics) is employed to illuminate the sample and to filter and collect the scattered radiation. This coaxial, two-fiber probe is very convenient and efficient for Raman experiments. However, the Raman probe we used for 532 nm excitation laser has a cut-off at 250 cm^{-1}, as shown (red dashed line) in Figure B.2. In order to study the metal-nitrate interaction which has intermolecular vibrational bands at ~250 cm^{-1} or lower, a Raman setup that can detect lower frequencies was designed and utilized. As shown in Figure B.1, in this setup, a 90° configuration for the incoming laser beam and detection is used. The 532 nm light from the CW laser (Spectra-Physics, Millennia II) is focused on the sample by the fiber optic probe (Inphotonics, RPS532/12-10). The scatter is focused onto the monochromator entrance slit using a BK7 lens. A long-pass 535 nm filter (Omega Optical, Custom) is placed (slightly tilted) in the light path before the monochromator to remove the 532 nm light. (The transmission curve of the long-pass 535 nm filter is shown in Figure B.3.) Raman bands with frequencies as low as 140 cm^{-1} can be detected using this low-frequency Raman setup. Figure B.2 shows the low-frequency Raman spectra of neat water and aqueous nitrate solutions with a slit width 40 μm and an exposure time 50 s. Two peaks

at 172 cm^{-1} and 216 cm^{-1} are observed, which are assigned to the stretching modes of hydrogen bonds.

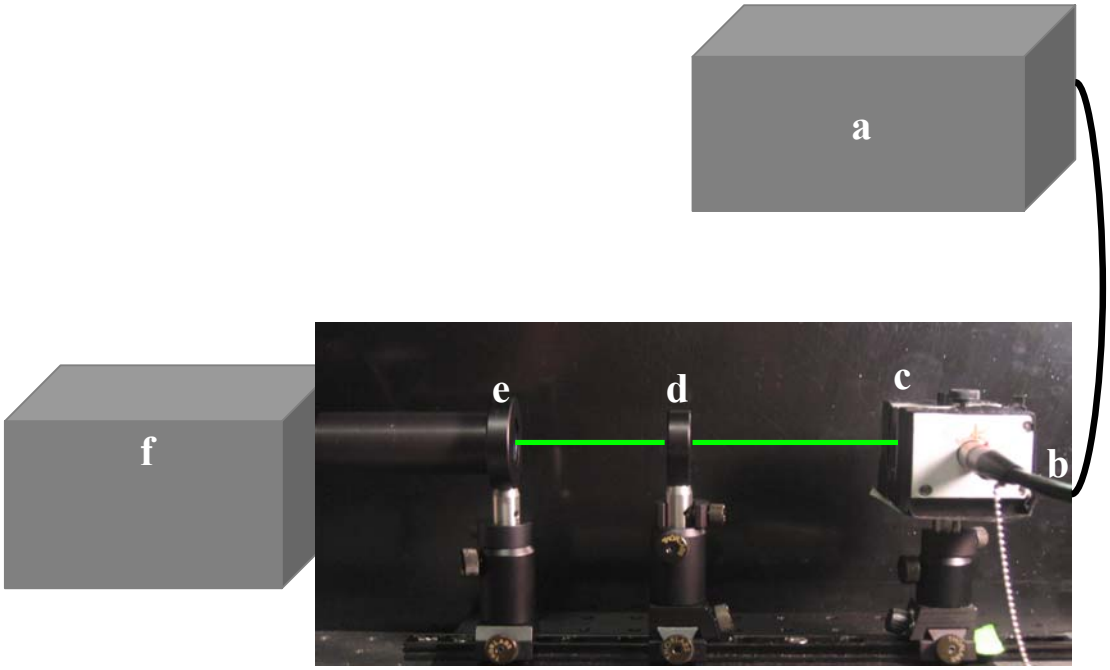

Figure B.1 Schematic layout of low-frequency Raman setup: (a) Spectra-Physics Millennia II laser; (b) fiber optic Raman probe; (c) sample holder; (d) focusing lens (FL = 75 mm); (e) 535 nm long-pass filter (Omega Optical, Custom); (f) monochromator and CCD.

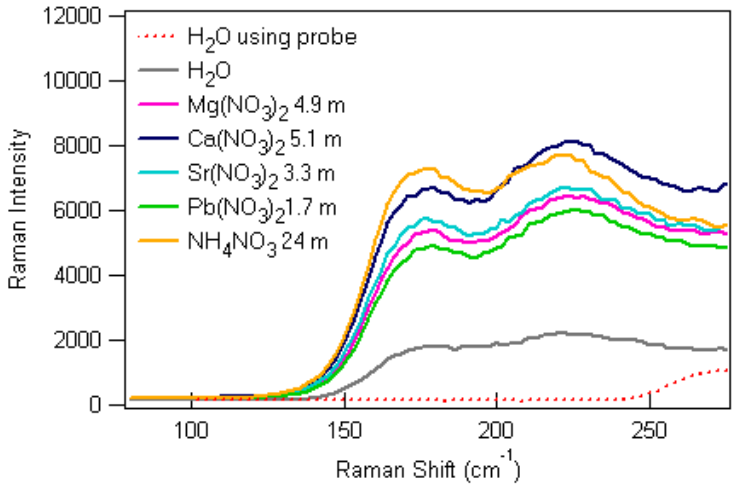

Figure B.2 Raman spectra of neat water and saturated aqueous solutions of $Mg(NO_3)_2$, $Ca(NO_3)_2$, $Sr(NO_3)_2$, $Pb(NO_3)_2$, and NH_4NO_3 obtained using the low-frequency Raman setup. The Raman spectrum of neat water measured with the Raman probe (red dashed line) is shown for comparison.

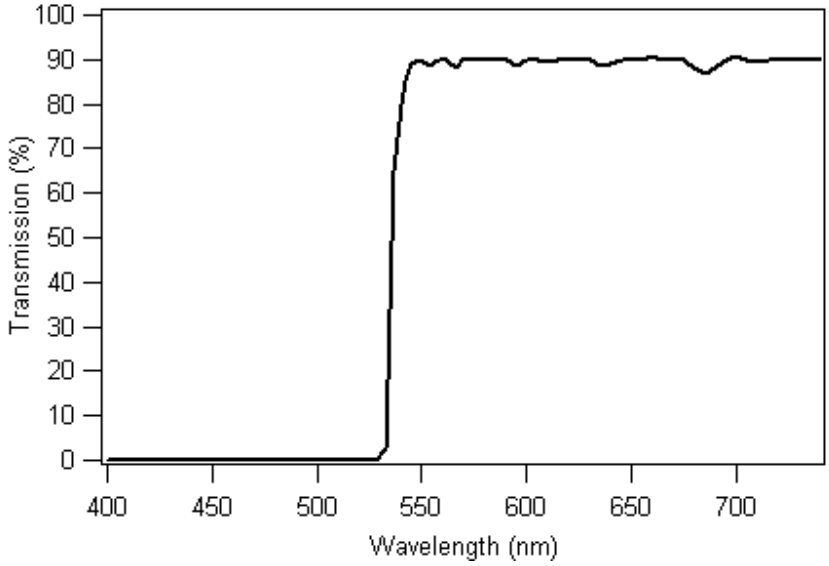

Figure B.3 Transmission curve of the 535 nm long-pass filter (Omega Optical, Custom).

APPENDIX C

ESTIMATION OF SURFACE MOLE FRACTION

The adsorption of a solute at the air-aqueous interface, hence the surface mole fraction, is characterized by the relative adsorption ($\Gamma_{2,1}$).[115,116] The relative adsorption is related to the surface tension (γ) through the Gibbs equation:[114,115,141]

$$\Gamma_{2,1} = -\frac{x(\frac{\partial \gamma}{\partial x})_{T,P}}{RT(1 + x\frac{\partial \ln f}{\partial x})} = \Gamma_2 - \Gamma_1 \frac{x}{1-x} \tag{C.1}$$

where x refers to the bulk mole fraction of the solute, EDA, f is the activity coefficient of EDA in the solution, R is the universal gas constant 8.314 J/(K·mol), T refers to the temperature, and Γ_1 and Γ_2 refer to the surface excess of water and EDA, with the unit μmol/m^2. In the present work, the surface tension values of EDA aqueous solutions were obtained by using a DeltaPi Tensiometer (Kibron Inc.) at ~297 K. According to the linear regression result of the experimental surface tension data (Figure C.1a), $(\frac{\partial \gamma}{\partial x})_{T,P}$ is constant which equals –30.0. The activity coefficient f for EDA in the binary system of EDA and water is predicted by using the UNIFAC group-contribution method,[142,143] as shown in Figure C.1b. The relative adsorption $\Gamma_{2,1}$ versus bulk mole fraction of EDA is plotted in Figure C.1c.

Assume the surface molecular areas of water (a_1) and EDA (a_2) are concentration independent, the following relationship exists based on the monolayer model.

$$N_{AV}(\Gamma_1 a_1 + \Gamma_2 a_2) = 10^{26} \tag{C.2}$$

where Γ_1 and Γ_2 are expressed in μmol/m^2, a_1 and a_2 are expressed in Å^2, and N_{AV} is Avogadro's number. a_1 is 8 Å^2 for water according to literature.[116] a_2 is estimated to be 14 Å^2 for EDA using the relative molecular surface area values provided by Gmehlling et al.,[143] which agrees with the experimental value.[144] The surface mole fraction (m.f.$_s$) can be obtained by:

$$m.f._s = \frac{\Gamma_2}{\Gamma_2 + \Gamma_1} \tag{C.3}$$

Figure C.1d shows the surface mole fraction versus the bulk mole fraction of EDA.

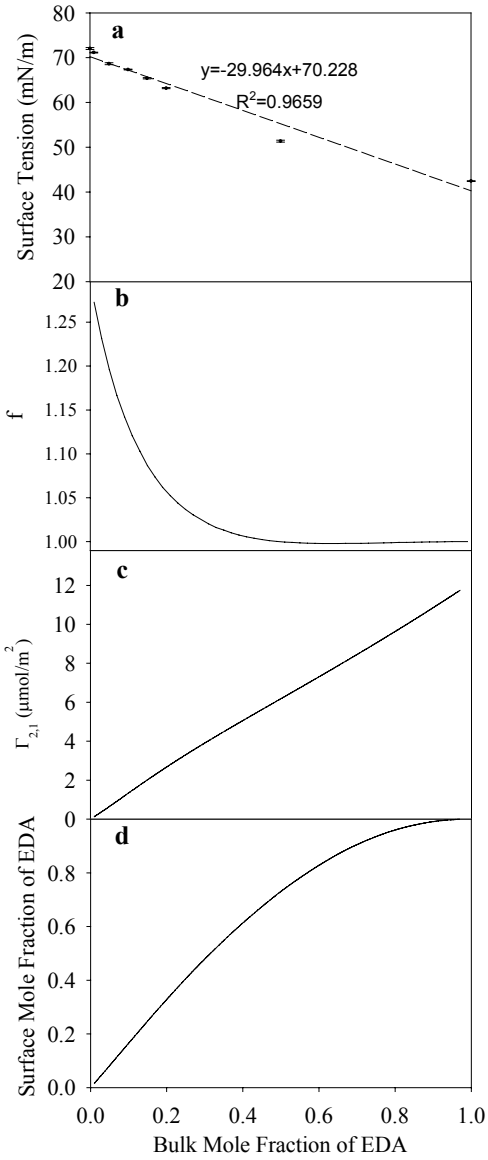

Figure C.1 (a) Surface tension values versus bulk mole fraction of ethylenediamine. Data points: experimental data with error bars; dashed line: linear regression. (b) Activity coefficient f of ethylenediamine in aqueous solutions. (c) Relative adsorption ($\Gamma_{2,1}$) of ethylenediamine in aqueous solutions. (d) Surface mole fraction of EDA versus bulk mole fraction of EDA.

APPENDIX D

ORIENTATION CALCULATIONS

The capability of determining molecular orientation is a significant advantage of VSFG studies.[145] Different components of $\chi^{(2)}$ are related to the spectroscopically active components of the molecular hyperpolarizability tensor $\beta^{(2)}$ by the average orientation angle of the functional group.[124,125,145-147] The molecular symmetry determines the nonzero elements of $\beta^{(2)}$.[125] In the present work the methylene groups of ethylenediamine are treated as having a C_{2v} symmetry. For the methylene group, the nonzero VSFG tensor elements of the symmetric stretch are β_{aac}, β_{bbc}, and β_{ccc} that are related by $\beta_{aac} + \beta_{bbc} = 2\beta_{ccc}$ for methylene at the standard bond angle 109.5°.[124-126] Though the bond angle in EDA is not exactly 109.5°, the value of $\beta_{aac} + \beta_{bbc} - 2\beta_{ccc}$ remains a small number close to zero. For the asymmetric mode, β_{aca} equals β_{caa}.[124-126] The *abc* represents the molecular coordination system.

The components of χ for the symmetric stretch (SS) are given by Lu et al.,[125] χ is described in the laboratory (xyz) coordinate system:

$$\chi_{xxz}^{SS} = \chi_{yyz}^{SS} = \frac{1}{4} N_s (\beta_{aac} + \beta_{bbc} + 2\beta_{ccc}) \langle \cos\theta \rangle + \frac{1}{4} N_s (\beta_{aac} + \beta_{bbc} - 2\beta_{ccc}) \langle \cos^3\theta \rangle \qquad \text{(D.1)}$$

$$\chi_{xzx}^{SS} = \chi_{zxx}^{SS} = \chi_{yzy}^{SS} = \chi_{zyy}^{SS} = -\frac{1}{4}N_s(\beta_{aac} + \beta_{bbc} - 2\beta_{ccc})(\langle\cos\theta\rangle - \langle\cos^3\theta\rangle) \quad \text{(D.2)}$$

$$\chi_{zzz}^{SS} = \frac{1}{2}N_s(\beta_{aac} + \beta_{bbc})\langle\cos\theta\rangle - \frac{1}{2}N_s(\beta_{aac} + \beta_{bbc} - 2\beta_{ccc})\langle\cos^3\theta\rangle \quad \text{(D.3)}$$

For the asymmetric stretch (AS), the components of χ are:[146]

$$\chi_{xxz}^{AS} = \chi_{yyz}^{AS} = -\frac{1}{2}N_s\beta_{aca}(\langle\cos\theta\rangle - \langle\cos^3\theta\rangle) \quad \text{(D.4)}$$

$$\chi_{xzx}^{AS} = \chi_{zxx}^{AS} = \chi_{yzy}^{AS} = \chi_{zyy}^{AS} = \frac{1}{2}N_s\beta_{aca}\langle\cos^3\theta\rangle \quad \text{(D.5)}$$

$$\chi_{zzz}^{AS} = N_s\beta_{aca}(\langle\cos\theta\rangle - \langle\cos^3\theta\rangle) \quad \text{(D.6)}$$

where θ is the tilt angle from the surface normal.

χ_{xxz}^{SS} and χ_{xxz}^{AS} are related to the VSFG spectra using the ssp polarization combination. According to previous work,[124] the relationships between $\beta_{ccc,}$ $\beta_{aac,}$ and β_{caa} are $\beta_{aac} = 2\cdot\beta_{ccc}$ and $\beta_{caa} = 1.053\cdot\beta_{aac}$ for CH_2 with C_{2v} symmetry. Combined with the relationships $\beta_{aac} + \beta_{bbc} = 2\beta_{ccc}$ and $\beta_{aca} = \beta_{caa}$ shown above, and assuming that $\frac{1}{2}N_s\beta_{ccc} = 1.00$ arbitrary unite (a.u.), equation D.1 and D.4 can be greatly simplified:

$$\chi_{xxz}^{SS} = 2\langle\cos\theta\rangle \quad \text{(D.7)}$$

$$\chi_{xxz}^{AS} = -2.106(\langle\cos\theta\rangle - \langle\cos^3\theta\rangle) \quad \text{(D.8)}$$

Here, absolute values of χ are used for the asymmetric stretch.

$$\chi_{xxz}^{AS} = \left| -2.106(\langle \cos\theta \rangle - \langle \cos^3\theta \rangle) \right| \quad \text{(D.9)}$$

Figure D.1 shows the dependence of second order susceptibilities on the tilt angle. The calculated tilt angle θ from the VSFG intensity ratio of the symmetric and asymmetric stretch are listed in Table D.1.

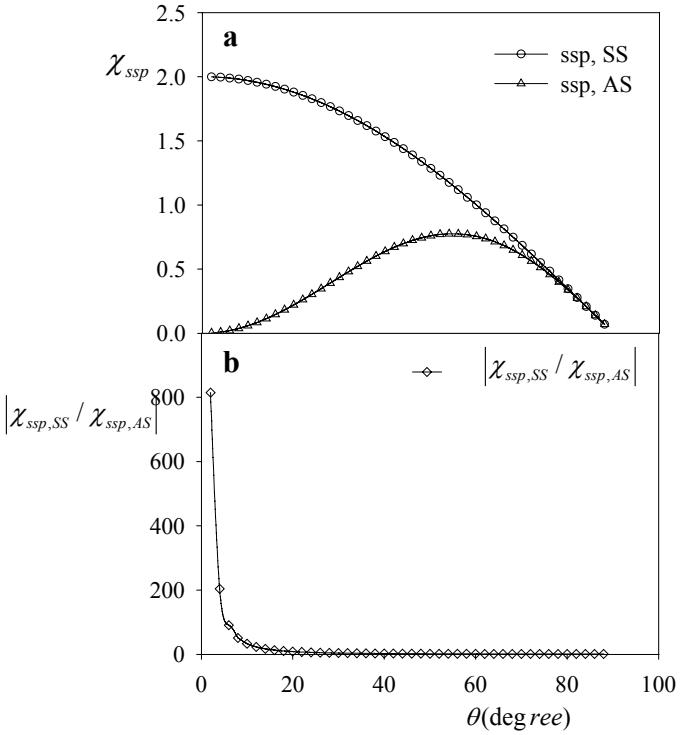

Figure D.1 (a) Second order susceptibilities for the symmetric (SS) and asymmetric (AS) stretch of methylene as a function of tilt angle. (b) The ratio between them as a function of tilt angle.

	$A_{(SS)}$[6]	$A_{(AS)}$[6]	$A_{(SS)}/A_{(AS)}$	χ_{SS}/χ_{AS}[6]	cos (θ)	θ (degree)
0.05 m.f. EDA	1502	368	4.08	2.02	0.7278	43±5
0.2 m.f. EDA	5430	2057	2.64	1.62	0.6445	50±3
Silica with EDA (5min)	506	171	2.96	1.72	0.6689	48±6
Singly protonated EDA	1135	1249	0.909	0.953	0.06211	86±4
EDD (doubly protonated EDA)	602	639	0.942	0.971	0.1473	82±2
Silica with EDA (24hr)	1290	1354	0.953	0.976	0.1647	81±7

Table D.1 Orientation calculation results of VSFG spectra (error in θ was determined by the error in the reproducible fits).

[6] A(SS): the area of CH_2-SS peaks; A(AS): the area of CH_2-AS peaks; χSS: the second order macroscopic nonlinear susceptibility of CH_2-SS; χAS: the second order macroscopic nonlinear susceptibility of CH_2-AS.

LIST OF REFERENCES

(1) Finlayson-Pitts, B. J.; Pitts Jr., J. N. Tropospheric air pollution: Ozone, airborne toxics, polycyclic aromatic hydrocarbons, and particles. *Science* **1997**, *276*, 1045-1052.

(2) Finlayson-Pitts, B. J.; Pitts Jr., J. N. *Chemistry of the Upper and Lower Atmosphere: Theory, Experiments and Applications*. Academic Press: San Diego, CA, 2000.

(3) Bauer, S. E.; Koch, D.; Unger, N.; Metzger, S. M.; Shindell, D. T.; Streets, D. G. Nitrate aerosols today and in 2030: a global simulation including aerosols and traposphere ozone. *Atmos. Chem. Phys.* **2007**, *7*, 5043-5059.

(4) Finlayson-Pitts, B. J.; Hemminger, J. C. Phyical chemistry of airborne sea salt particles and their components. *J. Phys. Chem. A* **2000**, *104*, 11463-11477.

(5) Finlayson-Pitts, B. J. The tropospheric chemistry of sea salt: A molecular-level view of the chemistry of NaCl and NaBr. *Chem. Rev.* **2003**, *103*, 4801-4822.

(6) Hoffmann, M. R.; Laskin, A.; Finlayson-Pitts, B. J. Sodium nitrate particles: physical and chemical properties during hydration and dehydration, and implications for aged sea salt aerosols. *Aerosol Sci.* **2004**, *35*, 869-887.

(7) Wolff, E. W.; Jones, A. E.; Martin, T. J.; Grenfell, T. C. Modelling photochemical NO_x production and nitrate loss in the upper snowpack of Antarctica. *Geophys. Res. Lett.* **2002**, *29*, 5.

(8) Blunier, T.; Floch, G. L.; Jacobi, H.-W.; Quansah, E. Isotopic view on nitrate loss in Antarctic surface snow. *Geophys. Res. Lett.* **2005**, *32*, L13501.

(9) Domine, F.; Shepson, P. B. Air-snow interactions and atmospheric chemistry. *Science* **2002**, *297*, 1506-1510.

(10) Boxe, C. S.; Colussi, A. J.; Hoffmann, M. R.; Perez, I. M.; Murphy, J. G.; Cohen, R. C. Kinerics of NO and NO2 evolution from illuminated frozen nitrate solutions. *J. Phys. Chem. A* **2006**, *110*, 3578-3583.

(11) Davis, D.; Nowak, J. B.; Chen, G.; Buhr, M.; Arimoto, R.; Hogan, A.; Eisele, F.; Mauldin, L.; Tanner, D.; Shetter, R.; Lefer, B.; McMurry, P. Unexpected high levels of NO oberved at South Pole. *Geophys. Res. Lett.* **2001**, *28*, 3625-3628.

(12) Manahan, S. E. *Fundamentals of Environmental Chemistry*. Lewis Publishers: Boca Raton, Fla., 2001.

(13) Weiner, E. R. *Applications of Environmental Chemistry: A Practical Guide for Environmental Professionals*. Lewis Publishers: Boca Raton, 2000.

(14) VanLoon, G. W.; Duffy, S. J. *Environmental Chemistry: A Global Perspective*. Oxford University Press: Oxford ; New York, 2000.

(15) Jones, J. B.; Holmes, R. M. Surface-subsurface interactions in stream ecosystems. *Trends in Ecology & Evolution* **1996**, *11*, 239-242.

(16) Wu, L.; Green, R.; Yates, M. V.; Pacheco, P.; Klein, G. Nitrate leaching in overseeded bermudagrass fairways. *Crop Science* **2007**, *47*, 2521-2528.

(17) Spiro, T. G.; Stigliani, W. M. *Chemistry of the Envionment*. Prentice Hall: Upper Saddle River, New Jersey, 2003.

(18) Salvador, P.; Curtis, J. E.; tobias, D. J.; Jungwirth, P. Polarizability of the nitrate anion and its solvation at the air/water interface. *Phys. Chem. Chem. Phys.* **2003**, *5*, 3752-3757.

(19) Dang, L. X.; Chang, T.-M.; Roeselova, M.; Garrett, B. C.; Tobias, D. J. On NO_3–H_2O interactions in aqueous solutions and at interfaces. *J. Chem. Phys.* **2006**, *124*, 066101.

(20) Minofar, B.; Vacha, R.; Wahab, A.; Mahiuddin, S.; Kunz, W.; Jungwirth, P. Prepensity for the air/water interface and ion pairing in magnesium acetate vs magnisium nitrate solutions: molecular dynamics simulations and surface tension measurements. *J. Phys. Chem. B* **2006**, 15939-15944.

(21) Thomas, J. L.; Roeselova, M.; Dang, L. X.; Tobias, D. J. Molecular dynamics simulations of the solution-air interface of aqueous nitrate. *J. Phys. Chem. A* **2007**, *111*, 3091-3098.

(22) Zhuang, X.; Miranda, P. B.; Kim, D.; Shen, Y. R. Mapping molecular orientation and conformation at interfaces by surface nonlinear optics. *Phys. Rev. B* **1999**, *59*, 12632-12640.

(23) Lambert, A. G.; Davies, P. B. Implementing the theory of sum frequency generation vibrational spectroscopy: A tutorial review. *Appl. Spectrosc. Rev.* **2005**, *40*, 103-145.

(24) Moad, A. J.; Simpson, G. J. A Unified Treatment of Selection Rules and Symmetry Relations for Sum-Frequency and Second Harmonic Spectroscopies. *J. Phys. Chem. B* **2004**, *108*, 3548.

(25) Gopalakrishnan, S.; Liu, D.; Allen, H. C.; Kuo, M.; Shultz, M. J. Vibrational spectroscopic studies of aqueous interfaces: Salts, acids, and nanodrops. *Chem. Rev.* **2006**, *106*, 1155-1175.

(26) Wang, H.-F.; Gan, W.; Lu, R.; Rao, Y.; Wu, B.-H. Quantitative spectral and orientational analysis in surface sum frequency generation vibrational spectroscopy (SFG-VS). *Int. Rev. Phys. Chem.* **2005**, *24*, 191-256.

(27) Long, D. A. *The Raman Effect: A Unified Treatment of the Theory of Raman Scattering by Molecules*. John Wiley & Sons: Chichester, England, 2001.

(28) Harris, D. C.; Bertolucci, M. D. *Symmetry and Spectroscopy: An Introduction to Vibrational and Electronic Spectroscopy*. Dover Publications: New York, 1989.

(29) Zhang, D.; Gutow, J.; Eisenthal, K. B. Vibrational spectra, orientations, and phase transitions in long-chain amphiphiles at the air/water interface: Probing the head and tail groups by sum frequency generation. *J. Phys. Chem.* **1994**, *98*, 13729-13734.

(30) Superfine, R.; Huang, J. Y.; Shen, Y. R. Experimental determinantion of the sign of molecular dipole moment derivatives: An infrared-visible sum frequency generation absolute phase measurement study. *Chem. Phys. Lett.* **1990**, *172*, 303-306.

(31) Shen, Y. R.; Ostroverkhov, V. Sum-frequency vibrational spectroscopy on water interfaces: Polar orientation of water molecules at interfaces. *Chem. Rev.* **2006**, *106*, 1140-1154.

(32) Lucarini, V.; Saarinen, J. J.; Peiponen, K.-E.; Vartiainen, E. M. *Kramers-Kronig Relations in Optical Materials Research*. Springer: Berlin ; New York, 2005.

(33) Zelsmann, H. R. Temperature dependence of the optical constants for liquid H2O and D2O in the far IR region. *J. Mol. Struct.* **1995**, *350*, 95-114.

(34) Bertie, J. E.; Eysel, H. H. Infrared intensities of liquids I: Determination of infrared optical and dielectric constants by FT-IR using the CIRCLE ATR Cell. *Appl. Spectrosc.* **1985**, *39*, 392-401.

(35) Bertie, J. E.; Lan, Z. Infrared intensities of liquids XX: The intensity of the OH stretching band of liquid water revisitedm and the best current values of the optical constants of H_2O(l) at 25°C between 15,000 and 1 cm^{-1}. *Appl. Spectrosc.* **1996**, *50*, 1047-1057.

(36) Kocak, A.; Berets, S. L.; Milosevic, V.; Milosevic, M. Using the Kramers-Kronig method to determine optical constants and evaluating its suitability as a linear transform for near-normal front-surface reflectance spectra. *Appl. Spectrosc.* **2006**, *60*, 1004-1007.

(37) Iizuka, K. *Elements of Photonics*. Wiley-Interscience: New York, N. Y., 2002.

(38) Liu, D.; Ma, G.; Levering, L. M.; Allen, H. C. Vibrational spectroscopy of aqueous sodium halide solutions and air-liquid interfaces: Observation of increased interfacial depth. *J. Phys. Chem. B* **2004**, *108, 2252-2260.*

(39) Xu, M.; Liu, D.; Allen, H. C. Ethylenediamine at air/liquid and air/silica interfaces: Protonation versus hydrogen bonding investigated by sum frequency generation spectroscopy. *Environ. Sci. Technol.* **2006**, *40*, 1566 -1572.

(40) Xu, M.; Callahan, K. M.; Tang, C. Y.; Tobias, D. J.; Allen, H. C. Nitrate ions and ion pairing at the air-aqueous interface. *In preparation.* **2008**.

(41) Hommel, E. L. A broad bandwidth sum frequency generation spectroscopic investigation of organic liquid surfaces. The Ohio State University, 2003.

(42) Marcus, Y.; Hefter, G. Ion pairing. *Chem. Rev.* **2006**, *106*, 4585-4621.

(43) Buchner, R.; Chen, T.; Hefter, G. Complexity in "simple" electrolyte solutions: Ion pairing in $MgSO_4$(aq). *J. Phys. Chem. B* **2004**, *108*, 2365-2375.

(44) Collins, K. D. Charge density-dependent strength of hydration and biological structure. *Biophys. J.* **1997**, *72*, 65-76.

(45) Fleissner, G.; Hallbrucker, A.; Mayer, E. Increasing contact ion pairing in the supercooled and glassy states of "dilute" aqueous magnesium, calcium, and strontium nitrate solution. Implications for biomolecules. *J. Phys. Chem.* **1993**, *97*, 4806-4814.

(46) Marcus, Y. *Ion solvation*. Wiley: Chichester, U. K., 1985.

(47) Irish, D. E.; Davis, A. R.; Plane, R. A. Types of interaction in some aqueous metal nitrate systems. *J. Chem. Phys.* **1969**, *50*, 2262-2263.

(48) Fleissner, G.; Hallbrucker, A.; Mayer, E. Raman spectroscopic evidence for increasing contact-ion pairing in the glassy states of "dilute" aqueous calcium nitrate solutions. *Chem. Phys. Lett.* **1994**, *218*, 93-99.

(49) Waterland, M. R.; Stockwell, D.; Kelley, A. M. Symmetry breaking effects in NO3-: Raman spectra of nitrate salts and ab initio resonance Raman spectra of nitrate-water complexes. *J. Chem. Phys.* **2001**, *114*, 6249-6258.

(50) Frost, R. L.; James, D. W. Ion-ion-solvent interactions in solution part 4. Raman spectra of aqueous solutions of some nitrates with monovalent cations. *J. Chem. Soc., Faraday Trans.* **1982**, *78*, 3235-3247.

(51) Irish, D. E.; Walrafen, G. E. Raman and infrared spectral studies of aqueous calcium nitrate solutions. *J. Chem. Phys.* **1967**, *46*, 378-384.

(52) Hester, R. E.; Plane, R. A. Raman spectrophotometric study of complex formation in aquesous solutions of calcium nitrate. *J. Chem. Phys.* **1964**, *40*, 411-414.

(53) Peleg, M. A Raman spectroscopic investigation of megnesium nitrate-water system. *J. Phys. Chem.* **1972**, *76*, 1019-1025.

(54) Smirnov, P.; Yamagami, M.; Wakita, H.; Yamaguchi, T. An X-ray diffraction study on concentrated aqueous calcium nitrate solutions at subzero

temperatures. *J. Mol. Liq.* **1997**, *73/74*, 305-316.

(55) Rohman, N.; Wahab, A.; Mahiuddin, S. Isentropic compressibility, shear relaxation time, and Raman spectra of aqueous calcium nitrate and cadmium nitrate solutions. *J. Solution Chem.* **2005**, *34*, 77-94.

(56) Spohn, P. D.; Brill, T. B. Raman spectroscopy of the species in concentrated aqueous solutions of $Zn(NO_3)_2$, $Ca(NO_3)_2$, $Cd(NO_3)_2$, $LiNO_3$, and $NaNO_3$ up to 450°C and 30 MPa. *J. Phys. Chem.* **1989**, *93*, 6224-6231.

(57) Chang, T. G.; Irish, D. E. Raman and infrared spectral study of magnesium nitrate-water systems. *J. Phys. Chem.* **1973**, *77*, 52-57.

(58) Hester, R. E.; Plane, R. A. Vibrational spectroscopies study of contact ion pairing between Zn^{++} and NO_3^- in water. *J. Chem. Phys.* **1966**, *45*, 4588-4593.

(59) Wahab, A.; Mahiuddin, S.; Hefter, G.; Kunz, W.; Minofar, B.; Jungwirth, P. Ultrasonic velocities, densities, viscosities, electrical conductivites, Raman spectra, and molecular dynamics simulations of aqueous solutions of $Mg(OAc)_2$ and $Mg(NO_3)_2$: Hofmeister effects and ion pair formation. *J. Phys. Chem. B* **2005**, *109*, 24108-24120.

(60) Irish, D. E.; Davis, A. R. Interactions in aqueous alkali metal nitrate solutions. *Can. J. Chem.* **1968**, *46*, 943-951.

(61) Irish, D. E.; Chang, G.; Nelson, D. L. Concerning cation-nitrate ion contact in aquesous solutions. *Inorg. Chem.* **1970**, *9*, 425-426.

(62) Kiriukhin, M. Y.; Collins, K. D. Dynamic hydration numbers for biologically important ions. *Biophys. Chem.* **2002**, *99*, 155-168.

(63) Watanabe, D.; Hamaguchi, H. Ion association dynamics in aqueous solutions of sulfate salts as studied by Raman band shape analysis. *J. Chem. Phys.* **2005**, *123*, 034508.

(64) Rudolph, W. W.; Irmer, G.; Hefter, G. T. Raman spectroscopic investigation of speciation in $MgSO_4$ (aq). *Phys. Chem. Chem. Phys.* **2003**, *5*, 5253-5261.

(65) Vollmar, P. M. Ionic interactions in aquesous solution: a Raman spectral study. *J. Chem. Phys.* **1963**, *39*, 2236-2248.

(66) Ikushima, Y.; Saito, N.; Arai, M. Raman spectal stdies of aqueous zinc nitrate solution at high temperatures and at a high pressure of 30 MPa. *J. Phys. Chem. B* **1998**, *102*, 3029-3035.

(67) Zhang, Y.-H.; Choi, M. Y.; Chan, C. K. Relating hygroscopic properties of magnesium nitrate to the formation of contact ion pairs. *J. Phys. Chem. A* **2004**, *108*, 1712-1718.

(68) Frank, H. S.; Wen, W.-Y. Structural aspects of ion-solvent interaction in

aqueous solutions: A suggested picture of water structure. *Discuss. Faraday Soc.* **1957**, *24*, 133.

(69) Irish, D. E.; Chang, T. G.; Tang, S.-Y. Raman and ultrasonic relaxation studies of some nitrate salts in N-methylacetamide. *J. Phys. Chem.* **1981**, *85*, 1686-1692.

(70) Shen, M.; Xie, Y.; Schaefer, H. F. Hydrogen bonding between the nitrate anion (conventional and peroxy forms) and water molecule. *J. Chem. Phys.* **1990**, *93*, 3379-3388.

(71) Waterland, M. R.; Kelley, A. M. Far-ultraviolet resonance Raman spectroscopy of nitrate ion in solution. *J. Chem. Phys.* **2000**, *113*, 6760-6773.

(72) Xu, M.; Larentzos, J.; Roshdy, M.; Spinney, R.; Criscenti, L. J.; Allen, H. C. Raman studies of aqueous metal-nitrate solutions: Hydration versus ion pairing. *In preparation.* **2008**.

(73) Kido Soule, M. C.; Blower, P. G.; Richmond, G. L. Nonliear vibrational spectroscopic studies of the adsorption and speciation of nitric acid at the vapor/acid solution interface. *J. Phys. Chem. A* **2007**, *111*, 3349-3357.

(74) Schnitzer, C. S.; Baldelli, S.; Shultz, M. J. Sum frequency generation of water on NaCl, $NaNO_3$, $KHSO_4$, HCl, HNO_3, and H_2SO_4 aqueous solutions. *J. Phys. Chem. B* **2000**, *104*, 585-590.

(75) Lilley, T. H. Thermodynamic introduction to solute-solute and solute-solvent interactions in biological fluids. In *Handbook of Metal-Ligand Interactions in Biological Fluids. Bioinorganic Chemistry*. Berthon, G., Ed.; Marcel Dekker, Inc.: New York, 1995; Vol. 1.

(76) Bertie, J. E.; Michaelian, K. H. Comparison of infrared and Raman wave numbers of neat molecular liquids: Which is the correct infrared wave number to use? *J. Chem. Phys.* **1998**, *109*, 6764-6771.

(77) Torii, H. Time-domain calculations of the polarized Raman spectra, the transient infrared absorption anisotropy, and the extent of delocalization of the OH stretching mode of liquid water. *J. Phys. Chem. A* **2006**, *110*, 9469-9477.

(78) Jungwirth, P.; Tobias, D. J. Specific ion effects at the air/water interface. *Chem. Rev.* **2006**, *106*, 1259-1281.

(79) Petersen, P. B.; Saykally, R. J. On the nature of ions at the liquid water surface. *Annu. Rev. Phys. Chem.* **2006**, *57*, 333-364.

(80) Durand-Vidal, S.; Simonin, J. P.; Turq, P. *Electrolytes at interfaces*. Kluwer Academic: Dordrecht ; Boston, 2000.

(81) Adamson, A. W.; Gast, A. P. *Physical chemistry of surfaces*. Wiley: New

York, 1997.

(82) Jungwirth, P. T., Douglas J. Molecular structure of salt solutions: A new view of the interface with implications for heterogeneous atmospheric chemistry. *J. Phy. Chem. B* **2001**, *105*, 10468-10472.

(83) Jungwirth, P.; Tobias, D. J. Ions at the air/water interface. *J. Phys. Chem. B* **2002**, *106*, 6361-6373.

(84) Dang, L. X.; Chang, T. M. Molecular mechanism of ion binding to the liquid/vapor interface of water. *J. Phy. Chem. B* **2002**, *106*, 235-238.

(85) Petersen, P. B.; Saykally, R. J.; Mucha, M.; Jungwirth, P. Enhanced concentration of polarizable anions at the liquid water surface: SHG spectroscopy and MD simulations of sodium thiocyanide. *J. Phy. Chem. B* **2005**, *109*, 10915-10921.

(86) Mucha, M.; Frigato, T.; Levering, L. M.; Allen, H. C.; Tobias, D. J.; Dang, L. X.; Jungwirth, P. Unified molecular picture of the surfaces of aqueous acid, base, and salt solutions. *J. Phys. Chem. B* **2005**, *109*, 7617-7623.

(87) Levering, L. M.; Sierra-Hernandez, M. R.; Allen, H. C. Observation of hydronium ions at the air-aqueous acid interface: Vibrational spectroscopic studies of aqueous HCl, HBr, and HI. *J. Phys. Chem. C* **2007**, *111*, 8814-8826.

(88) Petersen, P. B.; Saykally, R. J. Evidence of an enhanced hydronium concentration at the liquid water surface. *J. Phys. Chem. B* **2005**, *109*, 7976-7980.

(89) Yang, X.; Kiran, B.; Wang, X. B.; Wang, L. S.; Mucha, M.; Jungwirth, P. Solvation of the azide anion (N_3^-) in water clusters and aqueous interface: A combined investigation by photoelectron spectroscopy, density functional calculations, and molecular dynamics simulations. *J. Phy. Chem. A* **2004**, *108*, 7820-7826.

(90) Shultz, M. J.; Baldelli, S.; Schnitzer, C.; Simonelli, D. Aqueous solutions/air interfaces probed with sum frequency generation spectroscopy. *J. Phys. Chem. B* **2002**, *106*, 5313-5324.

(91) Richmond, G. L. Molecular Bonding and Interactions at Aqueous Surfaces as Probed by Vibrational Sum frequency Spectroscopy. *Chem. Rev.* **2002**, *102*, 2693-2724.

(92) Smith, J. D.; Cappa, C. D.; Wilson, K. R.; Cohen, R. C.; Geissler, P. L.; Saykally, R. J. Unified description of temperature-dependent hydrogen-bond rearrangement in liquid water. *Proc. Natl. Acad. Sci.* **2005**, *102*, 14171-14174.

(93) Wang, Z.; Pang, Y.; Dlott, D. D. Hydrogen-bond disruption by vibrational excitations in water. *J. Phys. Chem. A* **2007**, *111*, 3196-3208.

(94) Gopalakrishnan, S.; Jungwirth, P.; Tobias, D. J.; Allen, H. C. Air-liquid

interfaces of aqueous solution containing ammonum and sulfate: Spectroscopic and molecular dynamics studies. *J. Phys. Chem. B* **2005**, *109*, 8861-8872.

(95) Raymond, E. A.; Richmond, G. L. Probing the molecular structure and bonding of the surface of aqueous salt solutions. *J. Phys. Chem. B* **2004**, *108*, 5051-5059.

(96) Al-Abadleh, H. A.; Grassian, V. H. Oxide surfaces as environmental interfaces. *Surf. Sci. Rep.* **2003**, *52*, 63.

(97) Usher, C. R.; Michel, A. E.; Grassian, V. H. Reactions on mineral dust. *Chem. Rev.* **2003**, *103*, 4883.

(98) Leung, H.-W. Evaluation of the genotoxic potential of alkyleneamines. *Mutat. Res.* **1994**, *320*, 31-43.

(99) Bultinck, P.; Goeminne, A.; Van de Vondel, D. Ab initio conformational analysis of the chelating bidentate ligands ethylenediamine and 1,3-propanediamine. *J. Mol. Struct. (Theochem)* **1995**, *339*, 1-14.

(100) Rasmussen, K.; Tosi, C. Conformational analysis of 1,2-ethanediamine and 1,3-propanediamine by CFF, PCILO and ab initio methods. *Acta Chemica Scandinavica A* **1983**, *37*, 79-91.

(101) Kazerouni, M. R.; Hedberg, L.; Hedberg, K. Conformational analysis. 16. ethylenediamine. an electron-diffraction and ab initio investigation of molecular strcture, conformational composition, anti-gauche energy and entropy differences, and implications for internal hydrogen bonding. *J. Am. Chem. Soc.* **1994**, *116*, 5279-5284.

(102) Van Alsenoy, C.; Siam, K.; Ewbank, J. D.; Schafer, L. Ab initio studies of structural features not easily amenable to experiment. *J. Mol. Struct. (Theochem)* **1986**, *136*, 77-91.

(103) *Adsorption on Silica Surface*. Papirer, E., Ed.; Marcel Dekker, Inc.: New York, 2000; Vol. 90.

(104) Vidyadhar, A.; Rao, K. H.; Chernyshova, I. V. Mechanisms of amine-quartz interaction in the absence and presence of alcohols studied by spectroscopic methods. *J. Colloid Interface Sci.* **2002**, *256*, 59-72.

(105) Hirva, P.; Pakkanen, T. A. Modeling the interaction of amine bases on isolated and geminal hydroxyl groups on silica. *Surface Science* **1992**, *271*, 530-538.

(106) Gay, I. D.; Liang, S. Investigation of surface acidity by 13C NMR: adsorption of amines on silica, alumina, and mixed silica-alumina. *J. Catal.* **1976**, *44*, 306-313.

(107) Bucatariu, F.; Simon, F.; Spange, S.; Schwarz, S.; Dragan, S. Adsorption of poly(vinyl formamide-co-vinyl amine) onto silica particle surfaces and stability of the

formaed hybrid materials. *Macromol. Symp.* **2004**, *210*, 219-228.

(108) McCain, K. S.; Schluesche, P.; Harris, J. M. Modifying the adsorption behavior of polyamidoamine dendrimers at silica surfaces investigated by total internal reflection fluorescence correlation spectroscopy. *Anal. Chem.* **2004**, *76*, 930-938.

(109) Sokoll, R.; Hobert, H. Thermal desorption and infrared studies of amine adsorbed on SiO_2, Al_2O_3, Fe_2O_3, MgO and CaO: III. aniline and t-butylamine. *J. Catal.* **1990**, *125*, 285-291.

(110) Sokoll, R.; Hobert, H.; Schmuck, I. Thermal desorption and infrared studies of amine adsorbed on SiO_2, Al_2O_3, Fe_2O_3, MgO and CaO: I. diethylamine and triethylamine. *J. Catal.* **1990**, *121*, 153-164.

(111) Sokoll, R.; Hobert, H.; Schmuck, I. Thermal desorption and infrared studies of amine adsorbed on SiO_2, Al_2O_3, Fe_2O_3, MgO and CaO: II. isopropylamine and cyclohexylamine. *J. Catal.* **1990**, *125*, 276-284.

(112) Chabal, Y. J.; Hines, M. A.; Feijoo, D. Characterization of silicon surfaces and interfaces by optical vibrational spectroscopy. *J. Vac. Sci. Technol. A* **1995**, *13*, 1719-1727.

(113) Yaws, C. L.; Yang, H.-C. Henry's law constant for compound in water. In *Thermodynamic and Physical Property Data*; Yaws, C. L., Ed.; Gulf Publishing Company: Houston, TX, 1992; Vol.; pp 181-206.

(114) Defay, R.; Prigogine, I.; Bellemans, A. *Surface Tension and Adsorption*. John Wiley and Sons, Inc.: New York, NY, 1966.

(115) Jonsson, B.; B., L.; Holmberg, K.; Kronberg, B. *Surfactants and Polymers in Aqueous Solution*. John Wiley & Sons Ltd:, 1998.

(116) Tyrode, E.; Johnson, C. M.; Baldelli, S.; Leygraf, C.; Rutland, M. W. A vibrational sum frequency spectroscopy study of the liquid-gas interface of acetic acid-water mixtures: 2. orientation analysis. *J. Phy. Chem. B* **2005**, *109*, 329.

(117) Miranda, P. B.; Shen, Y. R. Liquid Interfaces: A Study by Sum-Frequency Vibrational Spectroscopy. *J. Phys. Chem. B* **1999**, *103*, 3292-3307.

(118) Buck, M.; Himmelhaus, M. Vibrational spectroscopy of interfaces by infrared-visible sum frequency generation. *J. Vac. Sci. Technol. A* **2001**, *19*, 2717-2736.

(119) Allen, H. C.; Raymond, E., A.; Richmond, G. L. Nonlinear vibrational sum frequency generation spectroscopy of atmospherically relevant molecules at aqueous solution surfaces. *Curr. Opin. Colloid Interface Sci.* **2000**, *5*, 74-80.

(120) Righini, R.; Calfano, S. The vibrational optical spectrum of ethylenediamine crystal: calculation of the one-phonon spectrum of the high-temperature

crystal form. *Chemical Physics* **1976**, *17*, 45-57.

(121) Kudoh, S.; TAkayanagi, M.; Nakata, M.; Ishibashi, T.; M., T. Infrared-induced rotational isomerization of 1,2-ethanediamine in argon matrices and conformational analysis by DFT calculation. *J. Mol. Struct.* **1999**, *479*, 41-52.

(122) Giorgini, M. G.; Pelletti, M. R.; Paliani, G.; Cataliotti, R. S. Vibrational Spectra and Assignments of Ethylene-Diamine and its Deuterated Derivatives. *J. Raman Spectrosc.* **1983**, *14*, 16-21.

(123) Batista de Carvalho, L. A. E.; Lourenco, L. E.; Margues, M. P. M. Confirmational study of 1,2-diaminoethane by combined ab initio MO calculations and Raman spectroscopy. *J. Mol. Struct.* **1999**, *482-483*, 639-646.

(124) Hirose, C.; Akamatsu, N.; Domen, K. Formulas for the analysis of surface sum-frequency generation spectrum by CH stretching modes of methyl and methylene groups. *J. Chem. Phys.* **1992**, *96*, 997-1004.

(125) Lu, R.; Gan, W.; Wu, B.-H.; Chen, H.; Wang, H.-f. Vibrational polarization spectroscopy of CH stretching modes of the methylene group at the vapor/liquid interfaces with sum frequency generation. *J. Phy. Chem. B* **2004**, *1008*.

(126) Wei, X.; Hong, S.; Zhuang, X.; Goto, T.; Shen, Y. R. Nonlinear optical studies of liquid crystal alignment on a rubbed polyvinyl alcohol surface. *Phys. Rev. E: Statistical Physics, Plasmas, Fluids, and Related Interdisciplinary Topics* **2000**, *62*, 5160-5172.

(127) Scherer, J. R. The Vibrational Spectroscopy of Water. In *Advances in Infrared and Raman Spectroscopy*; Clark, R. J. H., Hester, R. E., Ed.; Heyden: Philadelphia, 1978; Vol. 5; pp 149-216.

(128) Allen, H. C.; Raymond, E. A.; Richmond, G. L. Surface structural studies of methanesulfonic acid at air/aqueous solution interfaces using vibrational sum frequency spectroscopy. *J. Phys. Chem. A* **2001**, *105*, 1649-1655.

(129) Buch, V.; Devlin, J. P. A New Interpretation of the OH-Stretch Spectrum of Ice. *J. Chem. Phys.* **1999**, *110*, 3437-3443.

(130) Liu, D.; Ma, G.; Allen, H. C. Adsorption of 4-picoline and piperidine onto hydrated SiO_2 surface: Probing the surface acidity with vibrational sum frequency generation spectroscopy. *Environ. Sci. Technol.* **2005**, *39*, 2025-2032.

(131) Liu, D.; Ma, G.; Xu, M.; Allen, H. C. Adsorption of ethylene glycol vapor on a-Al_2O_3 (0001) and amorphous SiO_2 surfaces: observation of molecular orientation and surface hydroxyl groups as sorption sites. *Environ. Sci. Technol.* **2005**, *39*, 206-212.

(132) Venables, J. A. *Introduction to Surface and Thin Film Process*. Cambridge University Press: Cambridge, UK, 2000.

(133) Ong, S.; Zhao, X.; Eisenthal, K. B. Polarization of water molecules at a chaged interface: Second harmonic studies of the silica/water interface. *Chem. Phys. Lett.* **1992**, *191*, 327.

(134) Sahai, N. Is Silica Really an Anomalous Oxide? Surface Acidity and Aqueous Hydrolysis Revisited. *Environ. Sci. Technol.* **2002**, *36*, 445.

(135) Dines, T. J.; MacGregor, L. D.; Rochester, C. H. The surface acidity of oxides probed by IR spectroscopy of adsorbed diazines. *Phys. Chem. Chem. Phys.* **2001**, *3*, 2676.

(136) Hiemstra, T.; Venema, P.; Van Riemsdijk, W. H. Intrinsic proton affinity of reactive surface groups of metal hydroxides: the bond valence principle. *J. Colloid Interface Sci.* **1996**, *184*, 680-692.

(137) Ma, G.; Liu, D.; Allen, H. C. Piperidine adsorption on hydrated a-alumina (0001) surface studied by vibrational sum frequency generation spectroscopy. *Langmuir* **2004**.

(138) Bickmore, B. R.; Tadanier, C. J.; Rosso, K. M.; Monn, W. D.; Eggett, D. L. Bond-valence methods for pKa prediction: critical reanalysis and a new approach. *Geochim. Cosmochim. Acta* **2004**, *68*, 2025-2042.

(139) Querry, M. R.; Wieliczka, D. M.; Segelstein, D. J. Water (H_2O). In *Handbook of Optical Constants of Solids II*. Palik, E. D., Ed.; Academic: Boston, 1991; pp 1059-1077.

(140) Segelstein, D. J. The Complex Refractive Index of Water. University of Missouri, Kansas City, 1981.

(141) Alberty, R. A. On the derivation of the Gibbs adsorption equation. *Langmuir* **1995**, *11*, 3598-3600.

(142) Smith, J. M.; Van Ness, H. C. *Introduction to Chemical Engineering*, 4th ed.; McGraw-Hill: New York, NY, 1987.

(143) Gmehlling, J.; Rasmussen, P.; Fredenslund, A. Vapor-liquid equlibria by UNIFAC group contribution. Revision and extension. 2. *Ind. Eng. Chem. Process Des. Dev.* **1982**, *21*, 118-127.

(144) Gaines, J., G. L. Langmuir-blodgett films of long-chain amines. *Nature* **1982**, *298*, 544-545.

(145) Wang, C.; Groenzin, H.; Shultz, M. J. Surface characterization of nanoscale TiO_2 film by sum frequency generation using methanol as a molecular probe. *J. Phys. Chem. B* **2004**, *108*, 265-272.

(146) Brown, M. G.; Raymond, E. A.; Allen, H. C.; Scatena, L. F.; Richmond, G.

L. The Analysis of Interference Effects in the Sum Frequency Spectra of Water Interfaces. *J. Phys. Chem. A* **2000**, *104*, 10220-10226.

(147) Wang, J.; Chen, C.; Buck, S. M.; Chen, Z. Molecular chemical structure on poly(methyl methacrylate) (PMMA) surface studies by sum frequency generation (SFG) vibrational spectroscopy. *J. Phys. Chem. B* **2001**, *105*, 12118-12125.